DEPLOYABLE VERTICALLY ORIENTED SOLAR COLLECTORS UTILIZING ALL-INFLATED POLYMER CONSTRUCTION

MATTEO DAMIANO TIMPANO

A THESIS SUBMITTED TO
THE FACULTY OF GRADUATE STUDIES
IN PARTIAL FULFILLMENT OF THE REQUIREMENTS
FOR THE DEGREE OF
MASTER OF APPLIED SCIENCE

GRADUATE PROGRAM IN MECHANICAL ENGINEERING
YORK UNIVERSITY
TORONTO, ONTARIO

July 2022

Abstract

We realize the first all-inflated and vertically oriented solar trough concentrator that targets a low-concentration, low-cost regime. First, we derive the maximum concentration for a circular mirror coupled to a circular receiver based on the full collection condition. We then develop the structural framework for mechanically permissible vertical collectors using Euler-Bernoulli beam theory and present a novel Monte Carlo ray tracing algorithm that applies to mirrors that deflect due to wind-loading. The coupled structural and optical study, along with experimental flux mapping and a new methodology involving lasers, informed the development of a final prototype measuring 12" in diameter and 9 ft tall that achieves a flux concentration of 2.13. The final on-sun experiment resulted in an outlet temperature of 40°C and an outlet power of approximately 10 W at an efficiency of 2 - 4%. Experimental results were then verified using a thermal simulation using Simulink.

Extended abstract

Technologies that aim to harvest sunlight are severely limited by the dilute nature of solar radiation reaching the Earth's surface. At any given time, the maximum power generated by these technologies is approximately 1 kW/m^2, requiring large areas to be spanned in order to generate a significant power output. Even so, these technologies can only be realized if they can be made to achieve economies of scale with respect to existing power generation methods. To that end, concentrated solar power technologies (CSP) aim to minimize the cost of collecting aperture by intercepting solar radiation over large areas and delivering it to a smaller focal region. Perhaps the most mature CSP is the parabolic trough concentrator (PTC) which is a line-symmetric device with a thermodynamic concentration limit of 215×. Yet despite numerous design improvements, PTCs face three inherent challenges: (1) the associated construction cost is still too expensive resulting in an undesirable levelized cost of energy (LCOE), (2) the horizontal configuration underperforms in northern latitudes in the winter months, and (3) the achievable concentration cannot compare to that of solar power towers (SPTs). It is for these reasons that this work aims to completely redesign the solar trough concentrator such that it can be better placed within the overall picture of CSP technology.

Recognizing that solar trough concentrators will never be able to achieve the same operating temperatures and cycle efficiencies as the solar power tower, we shift our focus to low-concentration, low-cost designs useful on a much smaller scale. To satisfy these requirements, we shift to a pneumatic design utilizing a mirror with a circular arc cross-section. The benefit of doing so is that the mirror will automatically assume its required shape upon inflation, thus ridding the need for complex systems that approximate the parabola. More importantly, a significant portion of the overall construction cost of existing PTCs is attributed to the metal or concrete structural support members. Significant cost-savings are realized by switching to a concentrator that is erected vertically, relying on inflation pressure for structural support. Simultaneously, the vertical configuration results in better operating efficiencies in northern latitudes during the winter months when the sun is lower in the sky.

In this work, we first start by deriving the concentration ratio formula for a solar collector comprising a circular arc mirror coupled to a tubular absorber. Interestingly, the formula for concentration is separated into three regimes. We then study several exemplary designs from an optical and thermal perspective with the use of transmission angle curves and flux distributions to aid in the development of an solar concentrator optimized in terms of concentration.

We then provide the framework for structural stability in the vertical configuration. Utilizing Euler-Bernoulli beam theory, we recognize a range of acceptable aspect ratios, $5 \leq AR \leq 10$, that minimizes the effects of wind-loading from a structural and optical perspective. We also provide the construction procedure for key sub-assemblies such as the outer envelope (bag) and the inflation, thermal, and tracking sub-assemblies. Two methods of stowing the collector using tape springs and winches were also briefly explored. Construction was concluded by the development of a novel concentric receiver tube made of butyl rubber with solar selectivity equal to 1.05. The final values for geometric and flux concentration were 2.73 and 2.13, respectively.

We also present a novel Monte Carlo ray tracing algorithm for determining the intercept factor as the collector deflects due to wind-loading. The simulation is run for six cases. First the receiver is assumed to remain perfectly vertical, while the outer envelope is subject to a headwind, crosswind, and obliquewind respectively. In the latter half, the receiver is assumed to deflect the same amount as the outer envelope. Prescribing the operating conditions in this way provide a conservative and liberal estimate of the optical performance, respectively. At 4 m/s wind speeds, the intercept factor reduces to approximately 0.65 from 0.78 in the case of a stationary receiver and reduces negligibly in the case of a receiver that follows the deflection of the outer-envelope.

An in-depth thermal simulation using Simulink was then conducted. The simulation is set-up such that the receiver tube is segmented into finite sections to study the evolution of the temperature of the wall and of the heat transfer fluid. The flow rate which produces the maximum temperature was determined to be approximately 1 scfm producing an outlet temperature equal to 42°C. However, the temperature at the outlet is severely limited by the convective and radiative losses which amount to a thermal efficiency of 7%. Furthermore, it is shown that mitigating the thermal losses increases efficiency to approximately 25% and the outlet temperature to 110°C.

Experiments were then performed on the physical system to determine its optical and thermal performance. First, the surface of a Lambertian target was mapped using a laser to determine the physical effect of inflation pressure and wrinkling. It was determined that the effects of wrinkling are minimized for operating pressures equal to or greater than 1 psi. We then performed on-sun experiments to determine the flux distribution across the Lambertian target. The final flux map shows that the peak flux concentration ratio is equal to 2.33.

In the final experiment, the all-inflated vertical collector was deployed on the roof of the Bergeron Centre for Engineering Excellence to conduct on-sun tests in an effort to determine thermal performance. The average inlet and outlet temperature were determined to be approximately equal to 19.6°C and 40.0°C, respectively. The average power output and efficiency was determined to be in the range of 9.4 - 12.6 W and 2.6 - 4.2%, respectively. Finally, suggestions for improving thermal performance are provided.

Funding acknowledgements

I acknowledge the funding support of the Natural Sciences and Engineering Research Council of Canada (NSERC), which made this research possible.

Acknowledgements

I would like to start by thanking Dr. Cooper for providing me with the opportunity to conduct my studies under his supervision. It is not very often that you meet someone with such dedication and knowledge to their field of study that shows itself not only through their work, but the work of their students. I could not have accomplished what I have without his infinite guidance and support throughout my studies.

A special thanks goes out to all my lab mates Taz, Ana, Ikbal, Perry, Mubariz, and Gianpaolo. Their continued input allowed me to reach goals I never would have thought possible. You all made this such a memorable experience.

I would also like to extend my appreciation to my closest friends Jenna, John, Nicola, and Eliano. They have continually supported me when things got tough, provided a break when I needed it, and of course, celebrated my successes and achievements. I could not have done it without all of you.

Finally, I cannot express how thankful I am to have a family that supported me throughout all of it. To my brother Chris who paved the way for me, to my mom Caterina who pushed me to give it my all, to my dad Daniele who inspired me to become an engineer in the first place, to my grandfather Damiano who raised me, and to my grandmother Raffaella who I know is watching over me – thank you.

Table of Contents

List of figures

List of tables

Nomenclature

Greek Characters

α	Total hemispherical absorptance	-
α	Absorptance of the receiver	-
α_λ	Spectral hemispherical absorptance	-
α_{exp}	Experimentally calculated absorptance	-
β	Slope of a beam according to Euler-Bernoulli beam theory	° (rad)
β	Coefficient of volume expansion	1/K
γ	Intercept factor	-
δ	Deflection of the vertical collector	m
$\delta(\mathrm{z})$	Displacement function of the mirror undergoing wind-loading	m
δ_H	Deflection of the horizontal collector	m
δ_V	Deflection of the vertical collector	m
$\delta_{H,\mathrm{max}}/\delta_{\mathrm{max}}$	Maximum deflection of the horizontal collector	m
$\delta_{V,\mathrm{max}}$	Maximum deflection of the vertical collector	m
ε	Total hemispherical emittance	-
$\varepsilon_1/\varepsilon_2$	Principal strains in the fabric of an inflated collector	-
ε_λ	Spectral hemispherical emittance	-
$\varepsilon_{\mathrm{exp}}$	Experimentally calculated emittance	-
η	Optical efficiency	-
η_{opt}	Thermal efficiency	-

ϑ	Skew angle	°
θ	Polar angle characterizing the mirror in Qa-MCRT	°
θ	Solar elevation angle in the thermal simulation	°
θ_i	Acceptance angle	°
$\theta_{\max}$	Maximum polar angle of the mirror in Qa-MCRT	°
$\theta_{\min}$	Minimum polar angle of the mirror in Qa-MCRT	°
θ_V	Slope of the horizontal collector undergoing deflection	° (rad)
θ_V	Slope of the vertical collector undergoing deflection	° (rad)
θ_W	Wind direction in Qa-MCRT	°
λ	Wavelength	μm (nm)
ν	Kinematic viscosity	m^2/s
$\nu_{\theta x}$	Poisson ratio	-
ρ	Density of the air (wind) incident on the surface of the inflated collector	kg/m^3
ρ	Reflectance of the mirror	-
ρ_λ	Spectral hemispherical reflectance	-
σ	Stefan-Boltzmann constant	$W/m^2\ K^4$
σ	Slope/surface error of the mirror	° (rad)
$\sigma_{11}/\sigma_{22}/\sigma_{33}$	Principal stresses in the fabric of an inflated collector	N/m^2
σ_θ	Hoop stress in the fabric of an inflated collector	N/m^2
σ_L	Longitudinal stress in the fabric of an inflated collector due to inflation pressure	N/m^2
σ_A	Bending stress in the fabric of an inflated collector due to an applied load	N/m^2
τ	Transmittance of the top-sheet	-

τ_λ	Spectral hemispherical transmittance	-
φ	Polar angle used for characterizing the mirror of a generic collector	°
φ_{crit}	Critical angle which indicates the beginning of the two-reflection regime	°
$\varphi_{max,2\text{-}ref}$	Maximum rim angle of a circular mirror beyond which full collection is no longer observed	°
φ_{rim}	Rim angle for a generic mirror	°
ψ	Polar angle used to characterize the point on a circular receiver	°
ψ_1	Polar angle fulfilling condition 1 in the derivation for maximum geometric concentration of a circular mirror coupled to a circular absorber	°
ψ_2	Polar angle fulfilling condition 2 in the derivation for maximum geometric concentration of a circular mirror coupled to a circular absorber	°
ω	Distributed load of the surface of the inflated collector	N/m
ω	Polar angle used to characterize a circular mirror	°
ω^*	Intermediate angle where the reflected ray is tangent to the caustic produced by a circular mirror	°
ω_{crit}	Critical angle which indicates the beginning of the two-reflection regime	°
$\omega_{max,2\text{-}ref}$	Maximum rim angle of a circular mirror beyond which full collection is no longer observed	°
ω_{rim}	Rim angle for a circular mirror	°

Latin characters

A	Cross-sectional area of the inflated collector	m^2
A_i	Inlet aperture area	m^2
A_o	Outlet aperture area	m^2
AR	Aspect ratio	-
$\mathbf{c}$	Equation of the caustic produced by a circular mirror	-
C	Circumference of the receiver	m
$\mathbf{C}$	Parameterization of the infinitesimal cross-section for the mirror/receiver in Qa-MCRT	-
C_D	Drag coefficient of the inflated collector	-
C_{flux}	Flux concentration ratio	×
C_g	Geometric concentration ratio	×
$C_{g,\text{2-ref regime}}$	Geometric concentration within the two-reflection regime of a circular mirror	×
$C_{g,2D,\max}$	Maximum geometric concentration for 2D concentrators	×
$C_{g,\text{caustic regime}}$	Geometric concentration within the caustic regime of a circular mirror	×
$C_{g,\text{rim ray regime}}$	Geometric concentration within the rim ray regime of a circular mirror	×
c_p	Specific heat capacity	J/kgK
$C_{\mathrm{receiver,z}}$	z-component of the position of the receiver w.r.t. the origin	m (in.)
D	Diameter of the collector	m
D	Ray travel parameter in Qa-MCRT	-
$D_{\min}$	Minimum ray travel parameter in Qa-MCRT that produces an intersection	-

E	Elastic modulus	N/m^2
E_b	Blackbody emissive power	W/m^2
$E_{b\lambda}$	Blackbody spectral emissive power	W/m^2 μm
E_i	Irradiance at the inlet aperture	W/m^2
E_o	Irradiance at the outlet aperture	W/m^2
f	Receiver displacement factor	-
f	Fractional function	-
F	Applied load on the surface of the inflated collector	N
F_D	Drag force	N
F_R	Resultant force on the lowest extreme fibres of the inflated collector	N
g	Constant for gravitational acceleration	m/s^2
Gr_L	Grashof number	-
h	Convective heat transfer coefficient	W/m^{2}K
H	Height of the inflated collector/receiver	m
h_1	Local heat transfer gain using the temperature difference at the inlet	W/m^{2}K
h_a	Local heat transfer gain using the arithmetic mean of the terminal temperature differences	W/m^{2}K
h_ln	Local heat transfer gain using the logarithmic mean of the terminal temperature differences	W/m^{2}K
I	Area moment of inertia	m^4
k	z-component of the position of the receiver w.r.t. the origin	-
k	Thermal conductivity	W/mK
L/l	Length of the inflated collector	m

L_{AP}	Length of the inlet aperture in the thermal simulation	m
M	Main method	-
$\dot{m}$	Mass flow rate	kg/s
m^*	Non-dimensionalized moment	-
M_A	Applied moment on the surface of the inflated collector	Nm
M_C	Collapse moment of the inflated collector	Nm
$M_{C,\text{M}}$	Collapse moment according to the Main method	Nm
$M_{C,\text{STN}}$	Collapse moment according to the Stein method	Nm
m_{caustic}	Slope of the caustic produced by a circular mirror	-
$M_{W,\text{M}}$	Wrinkle moment according to the Main method	Nm
$m_{W,M}^*$	Non-dimensionalized moment according to the Main method	-
$m_{W,S}^*$	Non-dimensionalized moment according to the Stein method	-
$M_{W,\text{STN}}$	Wrinkle moment according to the Stein method	Nm
$\text{Nu}_{\text{combined}}$	Nusselt number for combined free and forced convection	-
$\text{Nu}_{L,\text{forced}}$	Nusselt number for forced convection at the top of the receiver	-
Nu_{free}	Nusselt number for free convection	-
$\hat{\text{n}}$	Inlet aperture normal	-
$\hat{\mathbf{n}}$	Normal vector of the mirror at the point of intersection in Qa-MCRT	-
$\mathbf{O}$	Coordinate origin	-
p	Internal pressure of the inflated collector	psi (N/m^2)
$\mathbf{P}$	Point on the circular mirror	-
P_{wind}	Pressure of the air (wind) incident on the surface of the inflated collector	N/m^2

Pr	Prandtl number	-
Q	Local heat gain at any point along the receiver in the thermal simulation	W
$\mathbf{Q}$	Parameterization of the circular receiver	-
Q_{gain}	Heat incident on the receiver that contributes to heating the heat transfer fluid	W
$Q_{\mathrm{gain,\ local}}$	Local heat gain between the wall of the receiver and the bulk fluid in thermal contact with it	W
Q_i	Heat incident on the inlet aperture	W
Q_{in}	Heat incident on the receiver	W
$Q_{\mathrm{in,1\text{-}seg}}$	Heat incident on a segment of the receiver in the thermal simulation	W
q_{local}	Local heat flux	W/m^2
Q_{loss}	Heat incident on the receiver that is lost due to convection or radiation	W
Q_o	Heat incident on the outlet aperture	W
Q_{out}	Useful heat carried by the heat transfer fluid extracted from the outlet of the receiver	W
q_{pyr}	Irradiance reading from the pyrheliometer	W/m^2
Q_{receiver}	Heat incident on the receiver	W
q_{source}	Heat from the source (sun)	W/m^2
Q_{targ}	Total heat over the surface of the Lambertian target	W
r	Radius of the receiver	m
$\mathbf{r}$	Parameterization of a reflected ray	-
$\vec{\mathbf{r}}$	Parameterization of a ray in Qa-MCRT	-
R	Radius of the mirror/collector	m

$R_{\text{cond., d. wall}}$	Thermal resistance corresponding to the conduction through the wall of the dummy tube	K/W
$R_{\text{cond., r. wall}}$	Thermal resistance corresponding to the conduction through the wall of the receiver	K/W
$R_{\text{conv., loss}}$	Thermal resistance corresponding to the convective losses off the receiver	K/W
$R_{\text{conv., air-to-d. wall}}$	Thermal resistance corresponding to the convection from the fluid in the annulus to the outer wall of the dummy tube	K/W
$R_{\text{conv., d. wall-to-air}}$	Thermal resistance corresponding to the convection from the inner wall of the dummy tube to the fluid on the inside of the dummy tube	K/W
$R_{\text{conv., r. wall-to-air}}$	Thermal resistance corresponding to the convection from the inner wall of the receiver to the fluid in the annulus	K/W
r_{crit}	Radius of the mirror in the two-reflection regime	m
$R_{\text{rad., loss}}$	Thermal resistance corresponding to the radiative losses off the receiver	K/W
Re_L	Reynolds number for external axial flow over the top of the receiver	-
$\vec{\mathbf{r}}_{\mathbf{spec}}$	Direction vector of the specularly reflected ray in Qa-MCRT	-
$\hat{\text{s}}$	Sun vector	-
$\hat{\mathbf{s}}$	Unit direction vector of an incident ray in Qa-MCRT	-
$\vec{\text{s}}$	Parameterization of the mirror undergoing wind-loading in Qa-MCRT	-
$s_{\text{loc},x}$	*x*-component of the direction vector of a ray in the LCS in Qa-MCRT	-
$s_{\text{loc},y}$	*y*-component of the direction vector of a ray in the LCS in Qa-MCRT	-
$s_{\text{loc},z}$	*z*-component of the direction vector of a ray in the LCS in Qa-MCRT	-

s_x	x-component of the direction vector of a ray in the GCS in Qa-MCRT	-
s_y	y-component of the direction vector of a ray in the GCS in Qa-MCRT	-
s_z	z-component of the direction vector of a ray in the GCS in Qa-MCRT	-
t	Parametric pathlength travelled by a ray	-
t	Thickness of the fabric of the inflated collector	m
t^*	Parametric pathlength travelled by a ray at the intermediate angle where the reflected ray is tangent to the caustic produced by a circular mirror	-
T_{01}	Temperature of the receiver wall at the inlet	°C (K)
T_{02}	Temperature of the receiver wall at the outlet	°C (K)
T_∞	Temperature of the surroundings	°C (K)
$T_{\mathrm{air,\ annulus}}$	Temperature of the heat transfer fluid (air) in the annulus	°C (K)
$T_{\mathrm{air,\ inner}}$	Temperature of the heat transfer fluid (air) in the dummy tube	°C (K)
T_{b1}	Temperature of the bulk fluid at the inlet	°C (K)
T_{b2}	Temperature of the bulk fluid at the outlet	°C (K)
$T_{\mathrm{d.\ wall\ inner}}$	Inner wall temperature of the dummy tube	°C (K)
$T_{\mathrm{d.\ wall\ outer}}$	Outer wall temperature of the dummy tube	°C (K)
T_{in}	Temperature at the inlet of the receiver	°C (K)
T_{o}	Operating temperature of the receiver	°C (K)
T_{out}	Temperature at the outlet of the receiver	°C (K)
$T_{\mathrm{r.\ wall\ inner}}$	Inner wall temperature of the receiver	°C (K)
$T_{\mathrm{r.\ wall\ outer}}$	Outer wall temperature of the receiver	°C (K)

T_s	Average surface temperature of the outer wall of the receiver	°C (K)
T_{sun}	Surface temperature of the sun	K
uint-8	8 bit unsigned integer	-
$\mathbf{v}$	Direction vector of a reflected ray	-
V	Velocity of the air (wind) incident on the surface of the inflated collector	m/s
V	Velocity of the air over the surface of the receiver	m/s
W_{AP}	Width of the inlet aperture in the thermal simulation	m
$W_{\text{proj.}}$	Projected width of the inflated collector	m
x_e	Starting x-coordinate of a ray in Qa-MCRT	-
x_{int}	x-coordinate of the intersection point in Qa-MCRT	-
$x_{n,\text{2D}}$	x-component of the normal vector in the two-dimensional analogue in Qa-MCRT	-
x_{surf}	x-coordinate of the mirror	-
y_e	Starting y-coordinate of a ray in Qa-MCRT	-
y_{int}	y-coordinate of the intersection point in Qa-MCRT	-
$y_{n,\text{2D}}$	y-component of the normal vector in the two-dimensional analogue in Qa-MCRT	-
y_{surf}	y-coordinate of the mirror	-
z_e	Starting z-coordinate of a ray in Qa-MCRT	-
$z_{n,\text{2D}}$	x-component of the normal vector in the two-dimensional analogue in Qa-MCRT	-

Abbreviations

BoPET	Biaxially-oriented polyethylene terephthalate	-
CSP	Concentrated solar power	-
CSR	Circumsolar ratio	-
DNI	Direct normal irradiance	W/m^2
EDPM	Ethylene propylene diene monomer rubber	-
ETFE	Poly(ethylene tetrafluoroethylene)	-
FEP	Fluorinated ethylene propylene	-
GCS	Global coordinate system	-
HCPV	High concentration photo voltaic	-
HTF	Heat transfer fluid	-
LCOE	Levelized cost of energy	USD/kWh
LCS	Local coordinate system	-
LFR	Linear Fresnel reflector	-
MCRT	Monte Carlo ray tracing	-
NIR	Near infrared (wavelength)	-
NREL	National Research Energy Laboratory	-
PTC	Parabolic trough concentrator	-
Qa-MCRT	Quasi-analytical Monte Carlo ray tracing	-
SAM	System Advisor Model	-
SPT	Solar power tower	-
STN	Stein method	-

Chapter 1

Introduction

In 2020, the global energy demand was approximately 557.1×10^{18} J or 13.2 billion tonnes of oil equivalent [1]. Despite the growth rate being -4.5% from the previous year due to the pandemic, the global energy demand has been growing at an alarming rate of 1.9% per annum since 2009 [1], and is set to rebound 4.6% in 2021 alone, returning to pre-pandemic levels [2]. This steady increase in global energy demand invariably results in an increase of CO_2 emissions, reaching a total of 31.5 Gt and resulting in an unprecedented atmospheric concentration of 412.5 parts per million in 2020 [2], [3]. For many, renewable energy remains the solution to combatting the global energy crisis, however, a fundamental lack of understanding of the existing resources prevents them from being utilized to their fullest extent. Consider the solar resource which emits thermal radiation that enters the Earth's outer atmosphere at an irradiance of 1367 W/m^2 [4]. The average irradiance striking the Earth's surface is approximately 54% of the value at the atmosphere [4]. This leaves 738 W/m^2 that contributes almost exclusively to heating the surface of the Earth. Multiplying by the Earth's surface area gives a total of 9.4×10^{16} W of essentially untapped energy. Further, multiplying by the number of seconds in a year results in approximately 3.0×10^{24} J, or more than 5300 times the global energy demand. Placing the solar resource in this perspective realizes a form of renewable energy that can power the needs of humankind almost indefinitely.

Despite the vast and untapped nature of the solar reserve, technical barriers exist that prevent solar technology from being a major contributor to global energy production. Solar energy is dilute, meaning that solar power is spread out rather evenly over the surface of the Earth. Harnessing this power requires spanning large areas of land to produce a significant output. This is exacerbated by the cost per m^2 of collector area of conventional solar power technologies, making these methods economically unattractive. Therefore, in order to fully realize solar power technologies as a real solution to an ever-growing problem, the dilute nature of sunlight must be dealt with on a large scale.

1.1. Motivation

Concentrated solar power technologies (CSP) have been evolving over the past few decades to combat the issues previously stated. CSP refers to a category of technologies which utilize a configuration of mirrors to focus sunlight onto a receiver positioned at their focal plane. The benefit of doing so is that the dilute irradiance from the sun can be intercepted over large areas and delivered to a singular focus, thus generating a significant thermal or electrical output. Economies of scale can only be achieved, however, if the cost per m^2 of collecting aperture is sufficiently minimized to achieve cost competitiveness with existing technology. According to a review article by Tagle-Salazar et al. the levelized cost of energy (LCOE) for fossil fuels in 2019 was 0.066 USD/kWh [5]. Although fossil fuels generally provide a low LCOE, this value provides a figure-of-merit to achieve cost competitiveness.

CSP can be subdivided into line and point focus systems. The latter consists of those designs fabricated from 3D extruded geometries such as the solar dish or solar tower. These solar energy technologies require 3D-axis tracking where both the mirror and the receiver track the sun throughout the day. 3D axis trackers have a much greater theoretical concentration ratio of 46000×, however their complicated geometries and tracking scheme render them very expensive [4]. Line focus systems are developed based on 2D extruded geometries and include technologies such as the linear Fresnel collector (LFC) or the parabolic trough concentrator (PTC). While these technologies can achieve a theoretical concentration ratio of only 215×, they are one-axis trackers and are therefore much simpler to develop [4]. The parabolic trough concentrator specifically has seen many improvements over the years making them more economically viable to produce.

A parabolic trough concentrator consists of three main components: a mirror, receiver, and a supporting structure. A conceptual design of a parabolic trough concentrator is shown in **Figure 1.1**. The first generation of parabolic trough concentrators, as the name suggests, utilized silvered glass mirrors or rigid aluminized reflectors shaped into parabolas [5], [6]. The receiver is fixed to the focus of the mirror, and internally carries a heat transfer fluid (HTF) such as water or thermal oil that raises in temperature as it is exposed to concentrated sunlight. The hot HTF is sometimes converted into electrical energy with an efficiency of 9-20% [6]. Alternatively, the receiver may be directly replaced with photovoltaics to convert from thermal to electrical energy directly. In doing so, the overall cell area is reduced due to concentration. In their review paper, Tagle-Salazar et. al stated that the average cost of the reflector surface is approximately \$20-30 per m^2 for silvered glass mirrors or less than \$20 per m^2 for aluminized reflectors [5]. While these values seem attractive at first, one third of the investment costs result from the steel and aluminum girders used as structural support [7]. In 2019 the LCOE of concentrating solar power based on PTCs utilizing a metal frame was approximately 0.259 USD/kWh [5].

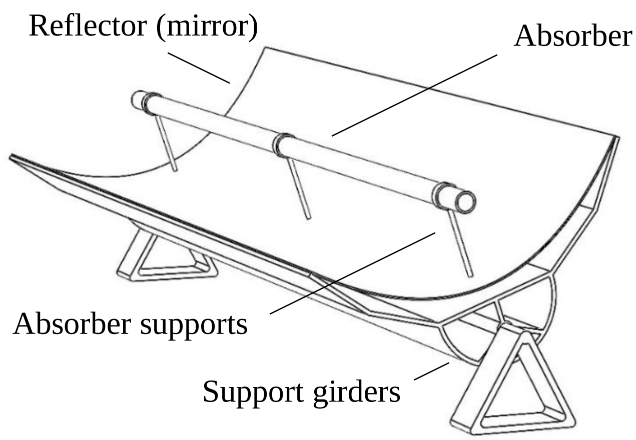

Figure 1.1. Conceptual design of a parabolic trough concentrator.

It is for these reasons that the PTC was redesigned to realize a more economically favoured design. First, it was proposed that a significant reduction in cost can be made by replacing the rigid mirror with thin film reflective polymers. The mirror is fastened at the edges to a transparent top-sheet and a modest millibar overpressure is applied to produce an inflated chamber where the receiver is housed. The mirror membrane is formed into a parabola using various techniques that will be discussed in the next section. Aside from resulting in a cheaper overall design, the transparent top-sheet also protects the mirror from external factors. The second innovation results from fabricating the support structure out of pre-cast concrete frames. A study performed by Pitz-Paal et al. has approximated a reduction in LCOE of 18-28% for these innovations [8]. The exact LCOE has yet to be determined. Nonetheless, however, even with a maximum reduction in LCOE, PTCs are still not cost competitive with traditional methods of energy production.

Despite their cost, PTCs are a mature technology and have been commercially proven over the years. Both the north-south and east-west tracking schemes have been thoroughly analyzed and their performance metrics are almost guaranteed in the geographical regions they have been tested. However, deployment location has been largely absent from the discussion of PTCs over their development. It is known that PTCs operate best when the sun is high in the sky due to a reduction in losses associated with angular elevation. In the winter months in northern latitudes, however, the sun appears lower in the sky, and therefore horizontally oriented PTCs will suffer a significant reduction in performance.

Finally, even as PTCs are further developed, they simply cannot compare with the fluxes and temperatures achieved by third generation solar power towers (SPTs) which operate at >700°C with a cycle efficiency of >50% [6]. However, while SPTs target large scale power generation, this leaves a technological gap for extremely low-cost, low-concentration technologies useful on a smaller scale.

The overwhelming cost, imposed losses in northern latitudes, and insufficient concentration compared to SPTs motivates a complete design overhaul of traditional PTCs. This thesis aims to realize a new configuration of economically viable solar collectors that target a low-concentration regime and can operate in northern latitudes without significant performance loss.

1.2. Literature review

This section will focus on discussing the recent advancements made with respect to CSP technology. The design, construction, and theoretical and experimental results will be detailed at length for comparison and for justification of the objectives of the current work. Specific emphasis is placed on the first and second generation solar collectors utilizing pneumatic polymer mirrors, as low-cost construction motivates the design space for PTCs [6].

The Solar Technology Laboratory at ETH Zurich was one of the first groups to realize PTCs based on inflated thin film membranes and supported on pre-cast concrete structures. In the paper provided by Bader et al., the advantages of this generation of solar collector were five folded: (1) the concrete structure is more rigid than its metal counterpart, (2) vibrations due to wind are largely eliminated, (3) the alignment of the mirror can be controlled by applying a differential pressure, (4) the transparent top-sheet used to enclose the pressurized chamber is self-cleaning, and (5) the mirror is protected by external forces [7]. In practice, however, the mirror membrane assumed a cylindrical shape upon inflation. To correct for the spherical aberration, two tailor-made secondary reflectors were included past the focus to redirect spilled radiation back towards the receiver. The prototype developed measured 49.4 m in length and 7.9 m in width. A comprehensive Monte Carlo ray tracing (MCRT) technique was applied to understand the maximum theoretical concentration ratio with and without surface errors within the mirror membrane. The concentration ratios were given as a distribution over the target plane, with $x = 0$ m indicating the centre of the target. In the ideal case where the mirror is without error, the maximum concentration ratio achievable occurs directly at the centre of the target and was given as 151 suns [7], however this value drops to approximately 21 suns with a surface error of 10 mrad. The corresponding optical efficiency was found to decrease approximately linearly with increasing surface error. The same MCRT technique was applied after inducing surface errors within the secondary mirror. At a surface error of 0 and 10 mrad, the concentration ratios were given as 151 and 73 suns, respectively [7]. As the surface error increases, the optical efficiency of the secondary mirrors decreases significantly less than the primary mirror. It was noted that the system is much more insensitive to changes in the secondary mirror, due to the reduced optical path to the target [7]. While the concrete frame was designed to give stability to the system, it was also found that the collector deforms under its own weight as it tracks the sun, significantly affecting the radius of the mirror. The system was simulated with a maximum deformation of 3 mm [7]. A strong variation of the concentration ratio is observed along the length of the collector with the peak concentration reducing from 151 to 51 suns [7]. The solar collector was then experimentally validated to analyze the compounding effects. The measured peak solar concentration ratio was found to be approximately 55 suns. Deviations from the maximum theoretical solar concentration ratio were due to: (1) a flat instead of ideally curved secondary mirror, (2) mirror reflectance equal to approximately 92%, (3) attenuation of irradiance through the transparent top-sheet equal to approximately 9-19%, varying according to different skew angles, and (4) performance reduction due to dust on the top-sheet [7].

The same research group then attempted to correct for the errors induced by a circular mirror by approximating a parabola using a method called the arc-spline [9]. In this configuration, secondary mirrors would not be necessary as the spilled radiation would be reduced by the better focusing capabilities of the parabola. In this method, the mirror is formed from four separate tangentially adjacent circular arcs. Each arc has an inner clamping point located near the centreline of the concentrator such that the volume in between each segment can be individually pressurized [9]. By applying a modest millibar vacuum under each membrane, each arc assumes a circular shape that approximates a parabola as a whole [9]. In theory, the maximum and root mean square difference between the position and slope of the arc-spline and the parabola were given as Δz_{max} = 0.33 mm, Δz_{rms} = 0.18 mm, $\Delta\alpha_{max}$ = 1.98 mrad, and $\Delta\alpha_{rms}$ = 0.8 mrad, respectively [9]. Due to the complex nature of the arcspline, a parameter study was then performed whereby parameters were individually deviated (in theory) to view their effects on concentration. The first parameter to be studied was the number of arcs that constitute the arcspline. It was found that four arcs suffice in approximating the parabola – any subsequent arcs provide a marginal benefit. With four arcs and a skew angle of 0°, the peak and average solar concentration ratio on a 0.1 m wide target was given as 208.1 and 87.6 suns, respectively [9]. Since four arcs proved ideal, all further parameter changes were made with respect to an arc-spline consisting of four segments subject to a skew angle of 30° such that the theoretical peak and average concentration equaled 160.9 and 74.8 suns, respectively [9]. Then, each of the following parameters were varied to study their effects on concentration: increasing the pressure of each individually controlled pressure chambers forming the arcspline by 1 Pa, decreasing the width of each section forming the arcspline by 1 mm, increasing the width of each section forming the arcspline by 2 mm, and subjecting the mid-point of the supporting girder to a 3 mm displacement due to self-weight. The parameter study revealed that these effects decrease the peak concentration by 3.7 – 17.3% and the average concentration by 2.1 – 11.2% [9]. It is noted by Bader et al. that it is possible to adjust the internal pressure of each membrane to compensate for a variation in mirror width, however, if the width deviates by more than 1.63 mm, the optimum geometry cannot be restored [9]. It is also noted that the maximum displacement of each girder varies on the girder under consideration (upper, lower, or central), however the magnitude is on the order of millimetres [9]. The arc-spline was then experimentally validated by performing an on-sun experiment. In this experiment, the skew angle equaled 60° and the maximum peak solar concentration ratio equaled 18.9 suns, or 39% of the maximum value [9]. The research group then summarized by providing the allowable deviations from each parameter for practical use which are: ±1 Pa difference in internal pressure, ±1 mm in membrane width without pressure correction, and less than 1 mm girder deflection.

To culminate the research on the arc-spline concentrator, an on-sun experiment was performed using an array of helically coiled absorber tubes [10]. Since the optical experiments, additional pneumatic sleeves were incorporated at the clamping junction, thus enabling the path length of each arc to be controlled using individual pressure control [10]. Air was used as the heat transfer fluid in the 212 m long prototype for several reasons: (1) air has no temperature limit, (2) it does not degrade and is non-toxic, and (3) is freely available in the atmosphere [10]. It is noted, however, that air has a lower thermal conductivity and volumetric heat capacity relative to typical heat transfer fluids which warranted receivers with larger heat transfer areas. In addition, truncated trumpet secondaries were used to increase the overall concentration. The theoretical geometric concentration ratios of the primary and secondary reflectors were given as 62.8 and 1.473, respectively, resulting in a maximum geometric concentration ratio of 92.5 [10]. Good et al. provide great detail regarding the receiver design, modelling of flow regimes, and characterization of theoretical thermal losses. This, however, will be foregone to discuss the experimental results. The surface of the arc-spline underwent shape scans to determine the angular deviation from the theoretical shape. In the off-sun experiment, the intercept factor that results from the shape scan was given as 0.94 [10]. In the on-sun experiment, however, the intercept factor was significantly reduced to 0.54, owing to elongation of mirror films due to thermal expansion and deflection of the concrete beams and receiver due to self weight [10]. Optical and thermal losses were also quantified in great detail, which prompted discussion of technical improvements for future iterations. Nonetheless, for a yearly direct normal irradiance (DNI) of 2400 kWh/m^2, their model predicts an annual thermal output of 500°C with a root mean square deviation of 6% for experimental results [10]. For comparison, the pumping power consumed varied from 0.17 kW at a mass flow rate of 0.51 kg/s to 5.9 kW at a mass flow rate of 2.0 kg/s. This accounted for 0.5-7.8% of the total thermal output power of the system multiplied by 0.35 for thermal to electric conversion.

Tabor and Zeimer emphasized the importance of developing an inexpensive solar concentrator by not only using a non-tracking primary, but also showed that a circular profile with triangular receiver outperforms the parabola for large enough acceptance angles [11]. Furthermore, Tabor and Zeimer showed that the triangular receiver outperforms a circular receiver as it captures the same radiation but minimizes the surface area [11]. Much of the paper provided by Tabor and Zeimer involved the derivation of the triangular receiver, but this will be foregone in favour of the experimental results. It was shown that for a triangular receiver with an acceptance angle of 15 to 20°, a circular reflector outperforms the parabola as the parabola loses symmetry as the ray tilts away from the optical axis [11]. The same phenomenon was observed with a circular receiver at lower acceptance angles. The circular trough concentrator was then constructed with a length of

12 m and a diameter of 1.5 m [11]. The receiver was fabricated such that it took the form of an isosceles triangle with a side length of about 13 cm and was coated with copper oxide to achieve an emittance of 0.15 and an absorptance of 0.9 [11]. Tabor and Zeimer achieved a concentration ratio of approximately 3 and an operation of 150°C [11]. The design cost of the solar collector was approximately \$20 per m^2 [11].

Most recently, De Los Santos-Garcia et al. attempted to develop a lightweight solar concentrator at a fraction of the cost of existing systems [12]. Inflation was achieved by using Mylar as the reflective surface formed into a cylinder, and sealing the enclosure with a polycarbonate film on top with transmittance of 88%. De Los Santos-Garcia et al. also utilized a unique receiver design based on a finned heat pipe mounted within an evacuated tube [12]. The outer tube was coated with an AlN coating to achieve solar selectivity and was thermally connected to the finned heat pipe carrying acetone [12]. Once significant operating temperatures were achieved, the acetone would boil and evaporate into a bulb inserted into a manifold, where the heat is extracted by flowing water [12]. The receiver was slightly tilted such that the acetone would flow back into the heat pipe after condensing [12]. Utilizing a heat pipe also provided the additional benefit of minimizing warm-up and cooldown losses as their heat capacities are lower than traditional liquid filled pipes [12]. The dimensions of the system measured 1.6 m in length and 1.2 m in width, limited by commercial off the shelf components [12]. Interestingly, the design proposed by De Los Santos-Garcia et al. had the receiver placed outside the pneumatic chamber. Nonetheless, the geometric concentration ratio was stated as 13.54 [12]. Tracking was achieved by using two light-dependent resistors (LDRs) attached to the concentrator separated by some distance [12]. The tracking motor would activate until the difference in resistance between the diodes were within an acceptable value, indicating that the concentrator was focused [12]. In practice, the optical efficiency with losses was approximately 0.57 while the thermal efficiency was between 0.25 and 0.32 [12]. The maximum temperature achieved in this experiment was 80°C limited by the fluid circulation system [12]. Nonetheless, De Los Santos-Garcia exemplified a low-cost alternative of solar concentrator costing \$58.50 per m^2 [12].

In addition to the literature detailed thus far, significant strides have been made to push the limits of the PTC in terms of concentration ratio. In the paper by Cooper et al. it is shown that it is possible to surpass the maximum theoretical concentration ratio of 215× by incorporating tracking secondaries [13]. The motivation behind their research was to replace the expensive cell area of photovoltaics with the less expensive concentrator area [13]. In this way, CSP technology can be used to leverage cheap reflector materials to focus sunlight onto smaller, and cheaper, photovoltaics. The so-called high concentration photovoltaic (HCPV) collector was based on the arc-spline collector previously developed at ETH Zurich. In this design, the primary mirror consists of two wings each assuming the shape of an off-axis parabola [13]. Each wing measured 5 m in width resulting in an overall collecting aperture of 10 m [13]. The secondary concentrating stage placed at the focal plane of each wing had a width of 0.07 m, resulting in a primary concentration ratio of 71× [13]. The secondary concentrators which assume the shape of an asymmetrically truncated transformer crossed with a truncated hyperbolic (trumpet) can individually track on an axis perpendicular to the primary [13]. The geometric concentration ratio for the secondary equaled 8.5× [13]. The total concentration of the system then equaled approximately 605× [13]. The system was simulated using VeGaS as the MCRT software and predicted an optical efficiency of 78% for the collector [13]. A solar-to-electrical efficiency of 25% is predicted year-round [13]. Cooper et al. later showed in a separate paper that it is also possible to achieve the same concentration ratios of parabolic reflectors using non-parabolic profiles [14].

1.3. The concept of the vertical collector

As was stated in the motivation there exists an untapped area in the trade-off between cost and performance, particularly for lower temperature applications. As a result, the concept of an all-inflated vertically oriented solar trough concentrator (shown schematically in **Figure 1.2**) is proposed to make the switch between high-cost long-lifetime systems to low-cost short-payback systems. **Figure 1.2 a)** shows the basic construction of a vertically oriented solar concentrator which features a transparent top-sheet and mirror bound together to form an outer-envelope. An internal pressure erects the outer-envelope and causes the cross-section to assume a circular shape. Solar radiation enters through the transparent top-sheet where it reflects off the mirror and heads towards the receiver as shown in **Figure 1.2 b)**. The solar radiation is then absorbed by the receiver and convects thermal energy to the heat transfer fluid flowing through it. Finally, the heat transfer fluid then flows towards the exit of the receiver where it is processed as useful heat.

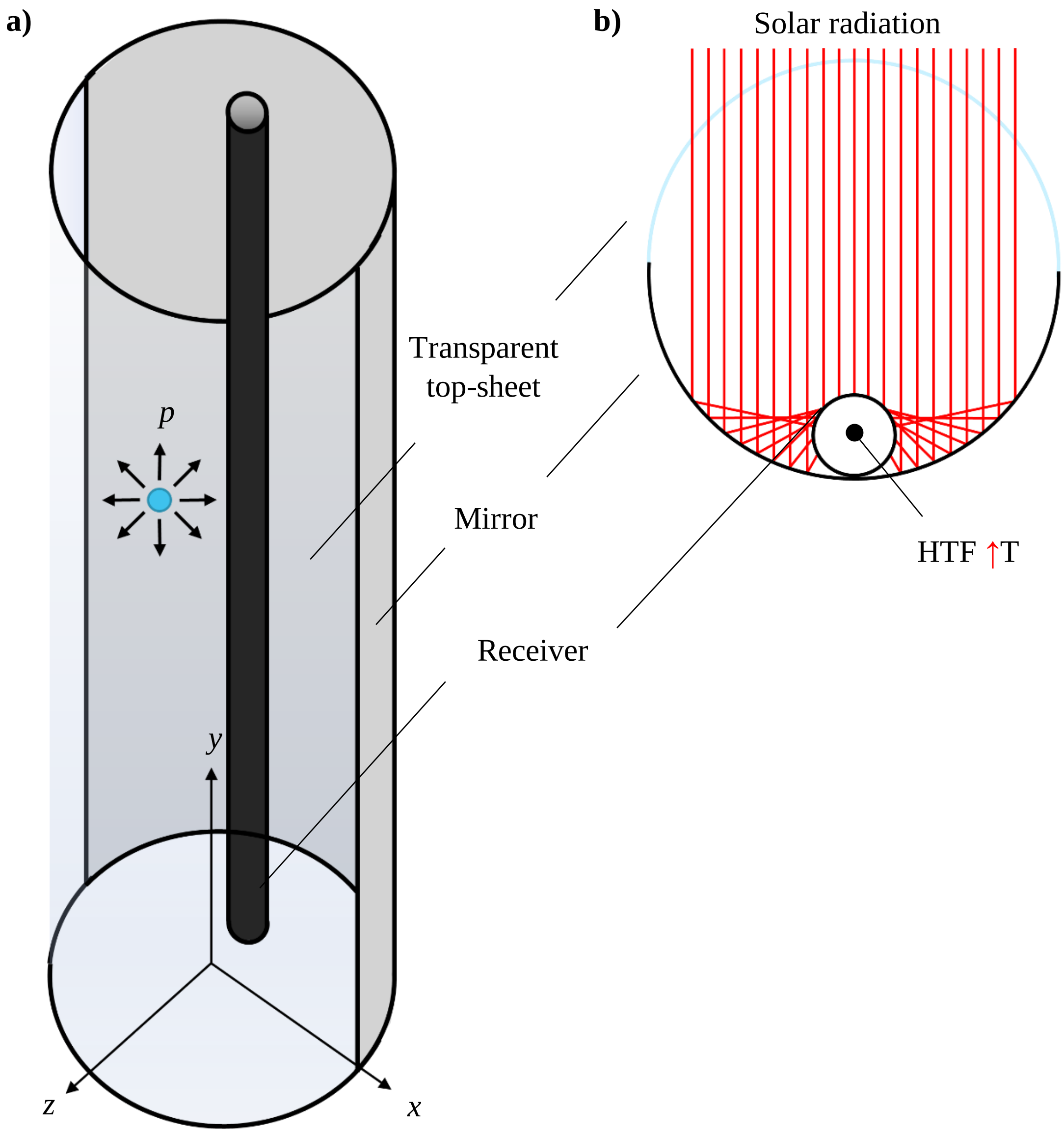

Figure 1.2. a) The main construction and conceptual design of an inflated vertically oriented solar concentrator; and **b)** the fundamental operating principal of the solar concentrator showing incident radiation reflecting off the mirror and being intercepted by the receiver where it transfers heat to the internal HTF.

1.4. Overarching goals

This next generation of solar collectors will be realized upon the investigation of several key innovations. First, the solar collector must be all-inflated. While the idea of pneumatic membranes is not particularly novel by itself, no solar concentrator has been constructed without framing spanning its length. The design, however, must rely on inflation pressure alone for structural integrity. This innovation then leads into the need for vertical orientation. Since the design will rely on inflation for structural support, it is more convenient to orient the collector vertically to minimize the effects of deflection due to self weight. Additionally, the target location for the design is northern latitudes, where the vertical orientation outperforms the horizontal orientation in the winter months. An additional layer of novelty is introduced as the design must utilize an inflated receiver tube as well. To date, all solar collectors utilize a rigid receiver tube coated with a solar selective material. The design, however, will see an immense decrease in cost by utilizing a fully inflated receiver tube made from flexible membranes. Since the collector area is now all-inflated and fully flexible, robotic deployment will be explored to autonomously stow and deploy the design as needed. Also resulting from inflation, the design must be lightweight. Most existing PTCs must be constructed on site due to their immense weight and size, specifically those with concrete frames which are cast directly at the location of deployment [7], [9], [10]. Others are made with size consideration in mind to allow for them to be transported using road vehicles [11]. The design, however, is to be fabricated such that it can be compacted and transported to the area of deployment cleanly and easily. Much like existing PTCs, the design must be capable of achieving simple tracking to leverage small acceptance angles with large concentration ratios. Finally, the design must be developed such that it is resistant to wind. If all these innovations are explored and leveraged together, this collector will see a drastic decrease in cost per m^2 of collecting aperture while enabling rapid deployment.

1.5. Project objectives

The overarching goals can be further elaborated to provide several objectives that determine the success of the project. The project objectives are succinctly described in the list below.

(1) Develop conceptual designs for a thermal prototype
(2) Develop a coupled structural-optical-thermal model for determining the performance of the design
(3) Construct a lab-scale prototype to demonstrate the structural and optical integrity of the design

(4) Select, measure, and optimize polymeric materials for use in the design

(5) Construct an outdoor “on-sun” prototype and measure the achieved efficiency

(6) Validate models vis-à-vis the experimental results, and use the validated model to optimize the design

1.6. Cost consideration

Since the cost per m^2 of collecting aperture is a primary driver of CSP technology, it is useful to establish a baseline for cost comparison of the collector to be developed in this work. In October 2021, the National Research Energy Laboratory (NREL) updated the baseline cost for parabolic trough concentrators using two state-of-the-art designs, namely the Ultimate Trough and the Sunbeam-MT [15]. The final cost estimate is exhaustive and is given as the installed cost in $\$/m^2$ and includes not only the material costs, but also the equipment needed for installation on-site and transportation costs [15]. Furthermore, NREL provides potential deviations in the installed cost by way of material production volume [15]. Nevertheless, it was found that the installed cost for the Ultimate Trough and the Sunbeam-MT were $\$152/m^2$ and $120/m^2$, respectively [15]. It was also found that the supporting structure comprised a significant portion of the installed cost in both cases amounting to $\$32.4/m^2$ (for the cantilever beams) in the Ultimate Trough and $\$30.2/m^2$ (space frame and support arms inclusive) in the Sunbeam-MT [15].

In February of 2022, NREL used their System Advisor Model (SAM) to update the cost estimate for heliostat designs, thus providing the most recent baseline for all CSP technology [16]. Their work compares a commercial design, the Stellio developed primarily by Schlaich Bergermann und Partner (sbp), and an advanced/developing design, the SunRing developed by Solar Dynamics of the United States [16]. Once again, the cost estimate for both designs included the material, manufacturing, assembly, and transportation costs [16]. The total installed cost for the Stellio and the SunRing were given as $\$127/m^2$ and $\$96/m^2$, respectively [16]. Therefore, in order for the current work to be successful, the total cost must less than $\$100/m^2$, preferably by an order of magnitude.

1.7. Thesis outline

The project defined by the overarching goals and objectives primarily deals with modelling, simulation, and design. As a result, this thesis will go through the design process of an all-inflated vertically oriented solar collector beginning from theory and culminating in the thermal results. As this design is the first of its kind, many of the procedures and results presenting here can be easily extended to other applications.

Chapter 2 discusses the background and theory necessary to understand the work that follows. Several fundamental terms are described that will be used throughout the text, followed by the derivation for maximum concentration for a trough concentrator comprising a circular mirror coupled to a circular absorber.

Chapter 3 is devoted to the structural design and material science behind the vertically oriented solar trough concentrator. The chapter begins by discussing the adaptation of Euler-Bernoulli beam theory to thin film inflated beams and how this may be extended to the application of solar concentrators subject to wind-loading. Then, a detailed process of the construction of several key components is provided including the outer envelope (bag), sealing methods, framing, and the inflation sub-assembly. The material of choice for the receiver is then discussed followed by a discussion of its construction. Finally, a discussion on furling and tracking is provided.

Chapter 4 discusses the optical modelling of the system. While Monte Carlo ray tracing methods are ubiquitously used in the design of CSP systems, analytical results are limited to geometries readily defined by closed form equations. The vertical trough concentrator, however, is subject to wind-loading and will deflect accordingly. This chapter discusses a quasi-analytical method of applying Monte Carlo ray tracing techniques to a vertical collector experiencing deflection due to wind-loading, followed by the results of the simulation applied to the prototype developed in the CooperLab.

Chapter 5 aims to develop a thermal model of the proposed collector in operation. An equivalent thermal circuit is provided to elucidate the thermal resistances and heat flows of the system, followed by a comprehensive thermal simulation developed in Simulink. The Simulink model provides a set of results corresponding to outlet temperature, thermal efficiency, convection coefficients, evolution of the temperature profile throughout the receiver, wall temperature along the receiver, and the losses that occur within the system.

Chapter 6 provides the experimental results that culminate the project. Chapter 6 is divided into two sections – optical and thermal. In the optical section, a combination of on- and off-sun methods are used to quantify the optical performance of the prototype equipped with a Lambertian target. First, the surface of the reflector is exposed to a laser in several locations and imaged. The images are then superimposed to provide details as to the effect of wrinkling on optical performance and to determine the correct operating pressure that minimizes these effects for on-sun experiments. The results of an on-sun experiment are then provided in the form of a flux map, which shows the distribution of concentration ratio across the target. In the thermal section, the collector is equipped with a thermal receiver and thermocouples for measuring temperature. The results of the culminating on-sun experiment are given over a 5-hour period.

Chapter 7 provides recommendations for future improvements. We return to the thermal simulation to elucidate the effects of mitigating thermal losses. Additionally, pathways to reducing leakage within the system and improvements to furling are discussed.

Chapter 2

Theory and background[1]

In this chapter, the background and theory for understanding this work is presented. First, we develop a simple analytical formula for the achievable geometric concentration ratio as a function of the rim angle and acceptance angle of the concentrator. Further, we probe the optical and thermal performance of several exemplary designs to understand all facets of operation. In doing so we develop a baseline for designing optimal concentrators that will be used in later Chapters.

2.1. Fundamentals of nonimaging optics

Nonimaging optics is a branch of optics that considers the thermodynamic transformation of electromagnetic radiation between a source and a target. Solar concentrators are optical devices that utilize this phenomenon by intercepting radiation over large areas and subsequently delivering it to a receiver smaller in size to maximize output temperature. The fundamental process of concentration is governed by two quantities, the geometric concentration ratio and the flux concentration ratio[2]. The geometric concentration ratio is defined as the ratio of the area at the inlet to the area at the outlet

$$C_g = A_i / A_o \tag{2.1}$$

The flux concentration ratio is defined as the ratio of the irradiance at the inlet aperture to that at the outlet

$$C_{\text{flux}} = E_i / E_o \tag{2.2}$$

The geometric concentration ratio and the flux concentration ratio are related by [17]

---

[1] Material in this section has been submitted for review in Solar Energy Engineering under Timpano and Cooper "Nonimaging behavior of circular trough concentrators with tubular receivers"
[2] Often the word ratio is omitted for brevity

$$C_{\text{flux}} = \frac{E_o}{E_i} = \frac{Q_o / A_o}{Q_i / A_i} = \frac{Q_o}{Q_i} C_g = \eta_{\text{opt}} C_g \tag{2.3}$$

where η_{opt} is the optical efficiency defined as the ratio of outlet power to inlet power. According to Eq. (2.1), the geometric concentration ratio can be made arbitrarily large by either increasing the area of the inlet aperture or decreasing the area of the outlet aperture. The flux concentration, however, is bound by thermodynamic laws. That is, increasing C_g past a certain limiting value will cause a corresponding decrease in the value of the optical efficiency in Eq. (2.3). Typically, solar concentrators are designed such that the optical efficiency is equal to exactly 1. This condition has been referred to as "full collection".

2.2. Concentration limits

Historically, two limits of concentration are provided for CSP technologies. The first limit is referred to as the thermodynamic limit and is derived based on the conservation of étendue. The exact derivation of the thermodynamic limit will be foregone, however, as it can be found in prior works [4]. Nevertheless, for a 2D trough geometry subject to a source that produces a cone of rays subtending a half angle of θ_i, the thermodynamic limit is

$$C_{g,2D,\max} = \frac{1}{\sin\theta_i} \tag{2.4}$$

Eq. (2.4) gives no consideration to the physical geometry of the system and therefore provides the absolute upper limit of concentration. If the source is the sun which produces a cone of rays subtending a half angle of 0.266°, the thermodynamic limit is equal to approximately 215×. While the thermodynamic limit allows us to better understand the fundamentals of concentration, the more important quantities are the specific limits. The specific limits reference the exact geometry of the system and provides the value of concentration that can be achieved in practice. The specific limits have been derived for several existing geometries such as the parabola with both a flat and tubular absorber and will be provided in a later section. However, there exists a major gap in literature as the formula for maximum concentration for a circular mirror coupled to a tubular receiver has not yet been derived. The next section aims to fill this gap by deriving the maximum concentration for this case.

2.3. Derivation of the maximum achievable concentration ratio[3]

2.3.1. Geometry and definitions

Consider a translationally-symmetric line-symmetric (trough) concentrator comprising a mirror with a circular arc cross-section coupled to a tubular absorber with a circular cross-section as shown in **Figure 2.1**. For a given width of the mirror, the receiver is to be sized for "full collection" meaning that all rays striking the mirror within an acceptance cone of $\pm\theta_i$ are reflected towards and intercepted by the receiver. In order to maximize the concentration ratio, we seek the smallest possible receiver which satisfies full collection for a given acceptance angle. The resulting concentration ratio represents the full collection concentration limit [14] for the particular case of a circular trough mirror with tubular receiver.

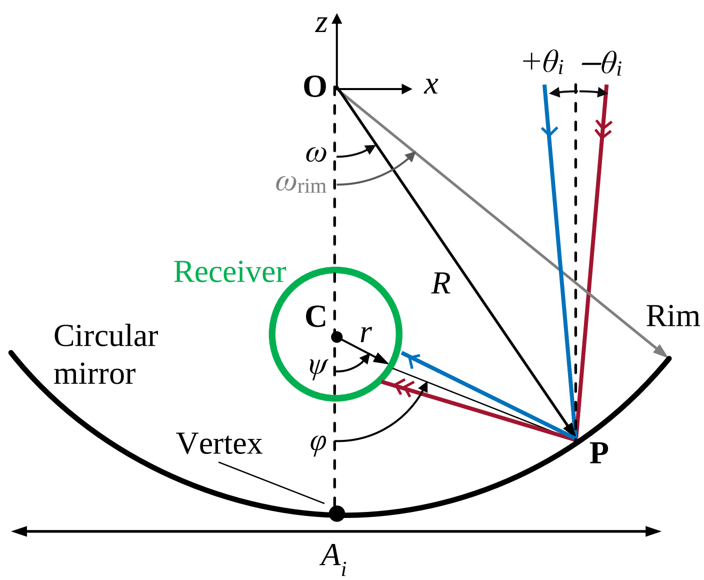

Figure 2.1. Cross-section of a solar trough concentrator with a circular mirror coupled to a circular receiver showing the main geometrical parameters.

The circular arc mirror with centre **O** at (0, 0) can be parameterized by

[3] Sections 2.3-2.5 (inclusive) correspond to material submitted for review in Solar Energy Engineering under Timpano and Cooper "Nonimaging behavior of circular trough concentrators with tubular receivers"

$$\mathbf{P} = \begin{bmatrix} P_x \\ P_z \end{bmatrix} = \begin{bmatrix} R\sin\omega \\ -R\sin\omega \end{bmatrix} \tag{2.5}$$

where ω is the parametric angle measured positive counterclockwise from $-z$ and spanning from $-\omega_{\text{rim}}$ to ω_{rim}. An on-axis ray parallel to z and incident on any point **P** on the mirror will be reflected such that it makes an angle of $\varphi = 2\omega$ with the optical axis as it approaches the receiver. The “rim angle” $\varphi_{\text{rim}} = 2\omega_{\text{rim}}$ represents the maximum angle that a reflected on-axis ray makes with respect to the optical axis, and is useful for comparison with other focusing concentrator types. The concentration ratio C_{g} is then defined as

$$C_g = \frac{A_i}{A_o} = \frac{2R\sin\omega_{\text{rim}}}{2\pi r} = \frac{R\sin\left(\frac{1}{2}\varphi_{\text{rim}}\right)}{\pi r} \tag{2.6}$$

where A_i is the inlet aperture area (projected width), A_o is the receiver aperture area (circumference), R is the radius of the mirror, and r is the radius of the receiver. In general, rays will be incident from within an acceptance cone of $\pm\theta_i$. The “edge rays” are defined as the set of rays incident at an angle $\theta = \pm\theta_i$, with those from $+\theta_i$ referred to as the left edge rays, and those from $-\theta_i$ as the right edge rays. Therefore, a generic ray incident on the mirror at any angle θ measured counterclockwise from the optical axis produces a reflected ray with direction vector **v** defined as

$$\mathbf{v} = \begin{bmatrix} v_x \\ v_z \end{bmatrix} = \begin{bmatrix} -\sin(\varphi-\theta) \\ \cos(\varphi-\theta) \end{bmatrix} = \begin{bmatrix} -\sin(2\omega-\theta) \\ -\cos(2\omega-\theta) \end{bmatrix} \tag{2.7}$$

A generic reflected ray may then be parameterized as

$$\mathbf{r} = \begin{bmatrix} r_x \\ r_z \end{bmatrix} = \mathbf{P} + t\mathbf{v} = \begin{bmatrix} R\sin\omega - t\sin(2\omega-\theta) \\ -R\cos\omega + t\cos(2\omega-\theta) \end{bmatrix} \tag{2.8}$$

where t is the parametric pathlength traveled by the ray after reflection. The caustic formed by the rays incident at a given angle θ is the solution to the following equation [18]

$$\frac{\partial r_x}{\partial t}\frac{\partial r_z}{\partial \omega} - \frac{\partial r_x}{\partial \omega}\frac{\partial r_z}{\partial t} = 0 \tag{2.9}$$

Inputting Eq. (2.8) into Eq. (2.9) and solving for t yields

$$t = \tfrac{1}{2} R\cos\left(\omega - \theta\right) \tag{2.10}$$

Substituting Eq. (2.10) into Eq. (2.8) gives the equation of the caustics as

$$\mathbf{c} = \begin{bmatrix} \tfrac{1}{4} R\left(3\sin\omega - \sin\left(3\omega - 2\theta\right)\right) \\ \tfrac{1}{4} R\left(-3\cos\omega + \cos\left(3\omega - 2\theta\right)\right) \end{bmatrix} \tag{2.11}$$

Now consider a circular absorber centred at some point along the optical axis and parameterized by

$$\mathbf{Q} = \begin{bmatrix} r\sin\psi \\ C_{\text{receiver},z} - r\cos\psi \end{bmatrix} \tag{2.12}$$

To size the receiver for maximum concentration, we need to determine the value of r and $C_{\text{receiver},z}$ that produces the smallest possible receiver that captures all reflected radiation from within $\pm\theta_i$ for a given ω_{rim}. Interestingly, as observed for the case of the circular mirror with flat receiver [19], depending on the choice of rim and acceptance angle, there exists multiple regimes with different conditions for constraining the minimum receiver size. The three different C_g regimes are shown schematically in **Figure 2.2**. In the first regime, which we denote the rim ray regime, the receiver may be sized using the edge rays reflected from the rim alone. In the second regime, which we denote the caustic regime, the receiver is sized based on the right edge ray reflected from the right rim and the left edge ray caustic. In the third regime, we allow for two reflections from the mirror, which enables an increase in aperture width while keeping the receiver size fixed. The achievable concentration ratio within these three regimes is detailed in the following sections.

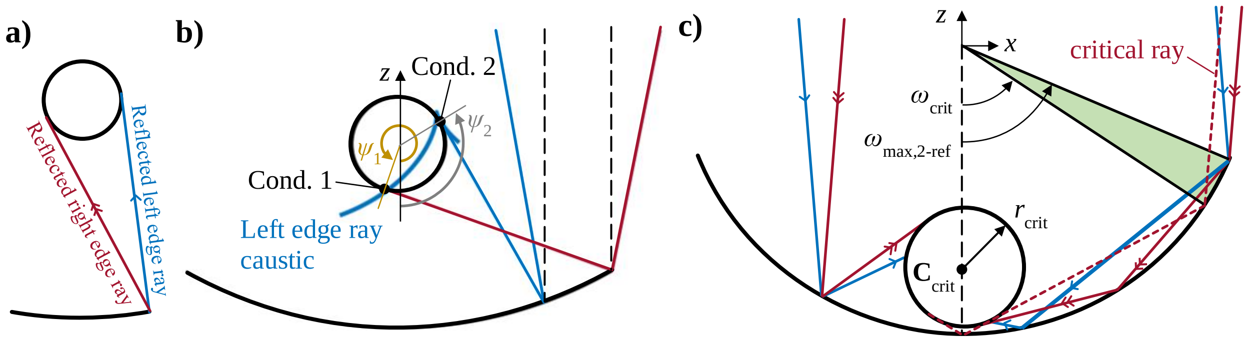

Figure 2.2. Three regimes producing different conditions for determining the minimum receiver size: **a)** rim ray regime where the receiver is sized based on the edge rays reflected from the rim alone; **b)** caustic regime where the receiver is sized based on the left edge ray caustic and the right edge ray from the rim; and **c)** two-reflection regime.

2.3.2. Rim ray regime

As seen in **Figure 2.2 a)**, for very small rim angles, the receiver may simply be sized based on a condition of tangency to the left and right edge rays reflected from the rim. Any rays reflected at an interior point $|\omega| < \omega_{\text{rim}}$ will be intercepted by a receiver thusly sized. Interestingly, for a parabolic trough with circular receiver, the receiver is sized using exactly the same rim ray condition [14]. Therefore, the concentration in this regime is identical to that achieved by a parabolic trough with circular receiver [14]

$$C_{g,\text{rim ray regime}} = \frac{\sin(2\omega_{\text{rim}})}{\pi \sin\theta_i} \tag{2.13}$$

However, for the circular trough, this rim ray regime persists only for extremely small rim angles, specifically for $\omega_{\text{rim}} < \theta_i$. The resulting designs therefore only make sense for very large θ_i and are even still too incompact and achieve too low C_g to be of practical use. Nevertheless, we include this regime within our formulation for completeness, and to highlight that, like the case of the flat receiver [19], a circular trough can match the C_g of the parabolic trough under very specific conditions.

2.3.3. Caustic regime

As the rim angle is increased, the condition of tangency to the edge rays from the rim no longer guarantees full collection, as rays reflected at interior points on the mirror begin to miss a receiver thusly sized. This defines a new, far more important regime where rays reflected from interior points on the mirror must be considered when sizing the receiver. To account for all interior points when sizing the receiver, it is logical to make use of the caustic of the edge rays, since this represents the envelope of rays reflected anywhere from the concentrator [18], [19]. As shown in **Figure 2.2 b)**, within this caustic regime, the minimum receiver size is specified by two conditions: 1) tangency of the receiver to the right edge ray coming from ω_{rim} and 2) tangency of the receiver to the left edge ray caustic. These two conditions may then be used to determine the value of $C_{\text{receiver},z}$ and r, after which C_g may be determined from Eq. (2.6).

Condition 1

Referring to **Figure 2.2 b)**, Condition 1 may be written mathematically as

$$\psi_1 = 270° + \left(2\omega_{\text{rim}} + \theta_i\right) \tag{2.14}$$

Inputting this value of ψ_1 into Eq. (2.12) yields the corresponding point on the receiver

$$\mathbf{Q} = \begin{bmatrix} -r\cos\left(2\omega_{\text{rim}} + \theta_i\right) \\ C_{\text{receiver},z} - r\sin\left(2\omega_{\text{rim}} + \theta_i\right) \end{bmatrix} \tag{2.15}$$

Now consider the equation of the right edge ray that reflects off ω_{rim}

$$\mathbf{r} = \begin{bmatrix} R\sin\omega_{\text{rim}} - t\sin\left(2\omega_{\text{rim}} + \theta_i\right) \\ -R\cos\omega_{\text{rim}} + t\cos\left(2\omega_{\text{rim}} + \theta_i\right) \end{bmatrix} \tag{2.16}$$

To fulfill tangency to the receiver, the intersection point of this ray with the receiver must occur at the value of ψ provided in Eq. (2.14). Intersecting Eq. (2.16) with Eq. (2.15) yields

$$x: \quad t = \frac{R\sin\omega_{\text{rim}} + r\cos\left(2\omega_{\text{rim}} + \theta_i\right)}{\sin\left(2\omega_{\text{rim}} + \theta_i\right)} \tag{2.17}$$

$$z: \quad t = \frac{C_{\text{receiver},z} - r\sin\left(2\omega_{\text{rim}} + \theta_i\right) + R\cos\omega_{\text{rim}}}{\cos\left(2\omega_{\text{rim}} + \theta_i\right)} \tag{2.18}$$

Equating Eq. (2.17) and Eq. (2.18) to eliminate t yields the following equation for $C_{\text{receiver},z}$

$$C_{\text{receiver},z} = \left(R\sin\omega_{\text{rim}} + r\cos\left(2\omega_{\text{rim}} + \theta_i\right)\right)\cot\left(2\omega_{\text{rim}} + \theta_i\right) + r\sin\left(2\omega_{\text{rim}} + \theta_i\right) - R\cos\omega_{\text{rim}} \tag{2.19}$$

Condition 2

Now consider Condition 2, which requires that the slope of the caustic be equal to the slope of the receiver at their point of intersection. The slope of the caustic is found from

$$m_{\text{caustic}} = \frac{\partial c_z / \partial\omega}{\partial c_x / \partial\omega} = -\cot\left(2\omega - \theta_i\right) = \tan\left(2\omega - \theta_i + 90°\right) \tag{2.20}$$

and the slope of the receiver is found from

$$m_{\text{receiver}} = \frac{dz}{dx} = \frac{dz / d\psi}{dz / d\psi} = \frac{\dfrac{d}{d\psi}\left(C_{\text{receiver},z} - r\cos\psi\right)}{\dfrac{d}{d\psi}\left(r\sin\psi\right)} = \tan\psi \tag{2.21}$$

Equating Eq. (2.20) and Eq. (2.21) yields the angle ψ_2 at the point of tangency

$$\begin{aligned} &\tan\left(2\omega^* - \theta_i + 90°\right) = \tan\psi_2 \\ &\psi_2 = 90° + \left(2\omega^* - \theta_i\right) \end{aligned} \tag{2.22}$$

In Eq. (2.22), ω has been replaced with ω^* to indicate the specific value of the parameter ω that fulfills the tangency condition. The coordinates of the receiver at this point are

$$\mathbf{Q} = \begin{bmatrix} r\sin\left(90° + \left(2\omega^* - \theta_i\right)\right) \\ C_{\text{receiver},z} - r\cos\left(90° + \left(2\omega^* + \theta_i\right)\right) \end{bmatrix} = \begin{bmatrix} r\cos\left(2\omega^* - \theta_i\right) \\ C_{\text{receiver},z} + r\sin\left(2\omega^* - \theta_i\right) \end{bmatrix} \tag{2.23}$$

We can now intersect Eq. (2.23) with the equation of the caustic, Eq. (2.11), to give the following two equations

$$r\cos\left(2\omega^* - \theta_i\right) = \tfrac{1}{4}R\left[3\sin\omega^* - \sin\left(3\omega^* - 2\theta_i\right)\right] \tag{2.24}$$

$$C_{\text{absorber},z} + r\sin\left(2\omega^* - \theta_i\right) = \tfrac{1}{4}R\left[-3\cos\omega^* + \cos\left(3\omega^* - 2\theta_i\right)\right] \tag{2.25}$$

Eqs. (2.19), (2.24), and (2.25) form a set of three equations with three unknowns r, ω^*, and $C_{\text{receiver},z}$, which can be solved to specify the receiver geometry which fulfills the full collection condition.

A simplified formulation of Condition 2

Solving Eqs. (2.19), (2.24), and (2.25) analytically, while possible, is tedious and yields an expression which is too long to be of practical use. Therefore, we seek an alternate way of expressing Condition 2 that will produce a set of simple, closed form equations identical in result to that of the caustic method. Since the caustic defines the curve to which each ray is tangent, if we knew the angle ω^* at which the caustic intersected and was tangent to the receiver, we could forego the caustic equation, and directly use the simpler ray equation (Eq. (2.16)) to fulfill Condition 2. Condition 2 is then rewritten as tangency to some ray at an intermediate angle ω^*

$$\mathbf{r} = \begin{bmatrix} R\sin\omega^* - t^*\sin\left(2\omega^* - \theta_i\right) \\ -R\cos\omega^* + t^*\cos\left(2\omega^* - \theta_i\right) \end{bmatrix} \tag{2.26}$$

Intersecting Eq. (2.26) with Eq. (2.23) yields

$$r\cos\left(2\omega^* - \theta_i\right) = R\sin\omega^* - t^*\sin\left(2\omega^* - \theta_i\right) \tag{2.27}$$

$$C_{\text{receiver},z} + r\sin\left(2\omega^* - \theta_i\right) = -R\cos\omega^* + t^*\cos\left(2\omega^* - \theta_i\right) \tag{2.28}$$

Equating Eqs. (2.27) and (2.28) to eliminate t^* yields the following equation for r

$$r = -C_{\text{receiver},z}\sin\left(2\omega^* - \theta_i\right) - R\sin\left(\omega^* - \theta_i\right) \tag{2.29}$$

Finally, we can eliminate $C_{\text{receiver},z}$ by substituting Eq. (2.19) into Eq. (2.29) to get

$$r = R\frac{\sin\left(2\omega^* - \theta_i\right)\sin\left(\omega_{\text{rim}} + \theta_i\right)\csc\left(2\omega_{\text{rim}} + \theta_i\right) - \sin\left(\omega^* - \theta_i\right)}{\sin\left(2\omega^* - \theta_i\right)\csc\left(2\omega_{\text{rim}} + \theta_i\right) + 1} \tag{2.30}$$

For any value of ω^*, Eq. (2.30) yields the receiver size that is just large enough to intercept all radiation for a mirror segment spanning from ω^* to the rim. However, we want the smallest possible receiver size that just satisfies full collection over the entire mirror. To find the size of the receiver that satisfies this condition, we scan over all angles from 0 to ω_{rim} to find the value of ω^* that produces the largest r. A receiver with this r will therefore collect all radiation within the acceptance cone reflected anywhere on the mirror. While the ω^* producing this maximum r could be determined by setting $d/d\omega^*$ of Eq. (2.30) equal to zero and solving, the resulting expression is too long to be of practical use. Fortunately, a simple approximate solution exists.

Figure 2.3 shows the resulting value of ω^* as a function of ω_{rim} for an acceptance angle of 1°. It is observed that the exact value of ω^* varies approximately linearly with ω_{rim}. This implies that there may be an approximate solution for ω^* that does not require solving for the maximum. Superimposed on **Figure 2.3** is a straight line of the form $\omega^* = ½\omega_{\text{rim}}$ which shows good agreement with the exact solution.

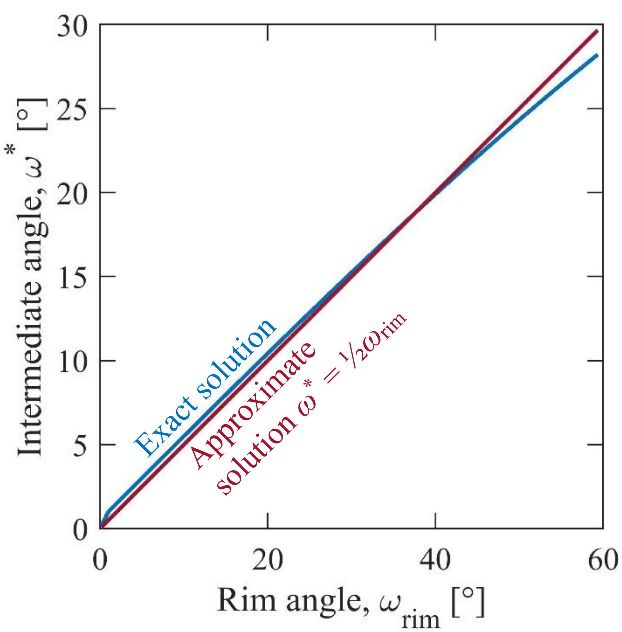

Figure 2.3. Comparison of the exact and approximate solution for ω^* for an acceptance angle $\theta = 1°$.

Using this convenient approximation, we may now replace ω^* with $\frac{1}{2}\omega_{\text{rim}}$ in Eq. (2.30) to yield the final equation for the receiver radius in the caustic regime

$$r = R\frac{\sin(\omega_{\text{rim}}-\theta_i)\sin(\omega_{\text{rim}}+\theta_i)\csc(2\omega_{\text{rim}}+\theta_i)-\sin\left(\frac{1}{2}\omega_{\text{rim}}-\theta_i\right)}{\sin(\omega_{\text{rim}}-\theta_i)\csc(2\omega_{\text{rim}}+\theta_i)+1} \tag{2.31}$$

With r now known, the concentration ratio may be readily determined using Eq. (2.6)

$$C_{g,\text{caustic regime}} = \frac{1}{\pi}\frac{\sin\omega_{\text{rim}}\left(\sin(\omega_{\text{rim}}-\theta_i)+\sin(2\omega_{\text{rim}}+\theta_i)\right)}{\sin(\omega_{\text{rim}}-\theta_i)\sin(\omega_{\text{rim}}+\theta_i)-\sin\left(\frac{1}{2}\omega_{\text{rim}}-\theta_i\right)\sin(2\omega_{\text{rim}}+\theta_i)} \tag{2.32}$$

2.3.4. Two-reflection regime

From **Figure 2.2**, it is observed that as ω_{rim} increases from **a)** to **c)**, the receiver simultaneously increases in size and shifts further down towards the vertex of the mirror to satisfy full collection. Further increasing ω_{rim} would cause the receiver to collide with the vertex of the mirror[4], at which point Eq. (2.31) would no longer produce a meaningful result. Fortunately, *before* this collision occurs, a fortuitous two-reflection condition occurs which removes the requirement of further increasing and downshifting the receiver.

Figure 2.2 c) shows the critical angle ω_{crit} at which the two-reflection condition begins. The dashed line shows a ray striking the mirror at an angle ω_{crit} which then reflects off the mirror and heads toward the receiver to fulfill Condition 2. Keeping the receiver placement and sized fixed, a ray striking the mirror at a slightly larger angle $\omega_{\text{crit}}+\Delta\omega$, would miss the receiver, and would continue towards the vertex of the mirror. However, this ray would then reflect off the mirror a second time, at the vertex, and would continue toward the left side receiver where it would be absorbed. Therefore, for angles somewhat larger than ω_{crit}, the receiver position and size can be fixed at that corresponding to ω_{crit}, with the rays being absorbed after two reflections. This two-reflection condition prevails up until $\omega_{\text{max,2-ref}}$, beyond which the twice-reflected right edge ray would leak through the gap between the receiver and the mirror. The shaded area corresponds to the geometry that produces the second concentration regime. Beyond $\omega_{\text{max,2-ref}}$, either the condition

[4] This collision occurs at a rim angle of $\omega_{\text{rim}} = 60.4°$ for an acceptance angle of $\theta_i = 1°$.

of full collection will be violated by the leaked rays, or the receiver size would need to be increased until eventually the receiver reached the vertex of the mirror. We return to this point in *Section 2.5*.

Geometrically, the critical angle is defined as the point on the rim where the right edge ray, after reflecting once off the mirror, would intercept the back vertex of the mirror $(0, -R)$. Mathematically, ω_{rim} may be determined by intersecting the reflected ray equation, Eq. (2.16), with the vertex $(0, -R)$, which, after some lengthy manipulation, yields the surprisingly simple result

$$\omega_{\text{crit}} = \tfrac{1}{3}\pi - \tfrac{2}{3}\theta_i \tag{2.33}$$

which allows ω_{crit} to be determined for any θ_i. **Figure 2.4** shows a plot of ω_{crit}, determined from Eq. (2.33), and $\omega_{\text{max,2-ref}}$, determined numerically, as a function of θ_i. This plot may be utilized to establish the limits of each concentration regime.

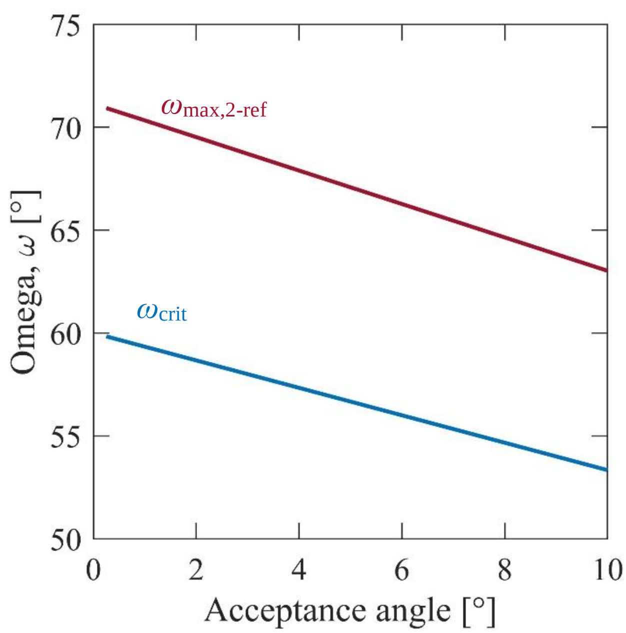

Figure 2.4. Critical and maximum ω as a function of the acceptance angle θ_i.

With ω_{crit} now determined from Eq. (2.33), it may be subbed in place of ω_{rim} in Eq. (2.31) to find r_{crit}

$$r_{\text{crit}} = R\frac{\sin\left(\frac{1}{3}\pi-\frac{5}{3}\theta_i\right)\sin\left(\frac{1}{3}\pi+\frac{1}{3}\theta_i\right)\csc\left(\frac{2}{3}\pi-\frac{1}{3}\theta_i\right)-\sin\left(\frac{1}{6}\pi-\frac{4}{3}\theta_i\right)}{\sin\left(\frac{1}{3}\pi-\frac{5}{3}\theta_i\right)\csc\left(\frac{2}{3}\pi-\frac{1}{3}\theta_i\right)+1} \tag{2.34}$$

For $\omega_{\text{crit}} < \omega < \omega_{\text{max,2-ref}}$, the receiver size (and position) may be fixed according to Eq. (2.34), with the assurance that rays are intercepted by the receiver after exactly two reflections off the mirror. Plugging Eq. (2.34) and into Eq. (2.6), the resulting geometric concentration ratio in the two-reflection regime becomes

$$C_{g,\text{2-ref regime}} = \frac{1}{\pi}\frac{\sin\omega_{\text{rim}}\left(\sin\left(\frac{1}{3}\pi-\frac{5}{3}\theta_i\right)+\sin\left(\frac{2}{3}\pi-\frac{1}{3}\theta_i\right)\right)}{\sin\left(\frac{1}{3}\pi-\frac{5}{3}\theta_i\right)\sin\left(\frac{1}{3}\pi+\frac{1}{3}\theta_i\right)-\sin\left(\frac{1}{6}\pi-\frac{4}{3}\theta_i\right)\sin\left(\frac{2}{3}\pi-\frac{1}{3}\theta_i\right)} \tag{2.35}$$

2.3.5. Final C_g formula

We may combine Eqs. (2.13), (2.32), and (2.35) together into a final C_g formula which covers both the one-reflection and two-reflection regimes

$$C_g = \begin{cases} \dfrac{1}{\pi}\dfrac{\sin\varphi_{\text{rim}}}{\sin\theta_i} & \varphi_{\text{rim}} \le 2\theta_i \\ \dfrac{1}{\pi}\dfrac{\sin\left(\frac{1}{2}\varphi_{\text{rim}}\right)\left(\sin\left(\frac{1}{2}\varphi_{\text{rim}}-\theta_i\right)+\sin\left(\varphi_{\text{rim}}+\theta_i\right)\right)}{\sin\left(\frac{1}{2}\varphi_{\text{rim}}-\theta_i\right)\sin\left(\frac{1}{2}\varphi_{\text{rim}}+\theta_i\right)-\sin\left(\frac{1}{4}\varphi_{\text{rim}}-\theta_i\right)\sin\left(\varphi_{\text{rim}}+\theta_i\right)} & 2\theta_i < \varphi_{\text{rim}} \le \varphi_{\text{crit}} \\ \dfrac{1}{\pi}\dfrac{\sin\left(\frac{1}{2}\varphi_{\text{rim}}\right)\left(\sin\left(\frac{1}{3}\pi-\frac{5}{3}\theta_i\right)+\sin\left(\frac{2}{3}\pi-\frac{1}{3}\theta_i\right)\right)}{\sin\left(\frac{1}{3}\pi-\frac{5}{3}\theta_i\right)\sin\left(\frac{1}{3}\pi+\frac{1}{3}\theta_i\right)-\sin\left(\frac{1}{6}\pi-\frac{4}{3}\theta_i\right)\sin\left(\frac{2}{3}\pi-\frac{1}{3}\theta_i\right)} & \varphi_{\text{crit}} < \varphi_{\text{rim}} \le \varphi_{\text{max,2-ref}} \end{cases} \tag{2.36}$$

where $\varphi_{\text{crit}} = \frac{2}{3}\pi - \frac{4}{3}\theta_i$ and $\varphi_{\text{max,2-ref}}$ may be read from **Figure 2.4**. In writing Eq. (2.36), ω has been recast using $\varphi = 2\omega$ to afford comparison to other concentrators, e.g. the parabola, where the polar angle φ is more relevant. Eq. (2.36) gives the achievable full collection geometric concentration for a circular trough coupled to a circular receiver for any rim angle up to $2\omega_{\text{max,2-ref}}$ and any acceptance angle. **Figure 2.5** shows the resulting C_g as a function of the rim angle for an acceptance angle of 1°, where the solid lines correspond to the rim ray and caustic regime, and the dashed lines correspond to the two-reflection regime.

It is observed that the highest concentration ratios occur for relatively small rim angles. For an acceptance angle of 1°, a peak C_g of 7.688× is achieved for a rim angle of 36°. As the rim angle is increased, the required receiver size increases dramatically resulting in a drop to a local minimum of 1.46× at a rim angle of 118.66°, which corresponds to ω_{crit}. As the rim angle is further increased, the receiver radius remains constant, with radiation incident on the mirror above ω_{crit} being directed to the receiver after two reflections off the mirror. While the receiver remains fixed, the inlet aperture width scales with $R\sin(½\varphi_{rim})$, resulting in a slight increase in geometric concentration with increasing rim angle. The curve terminates at a rim angle of 140.66° which corresponds to the end of the two-reflection regime. For rim angles larger than this, some radiation would begin to leak through the gap between the receiver and the mirror vertex

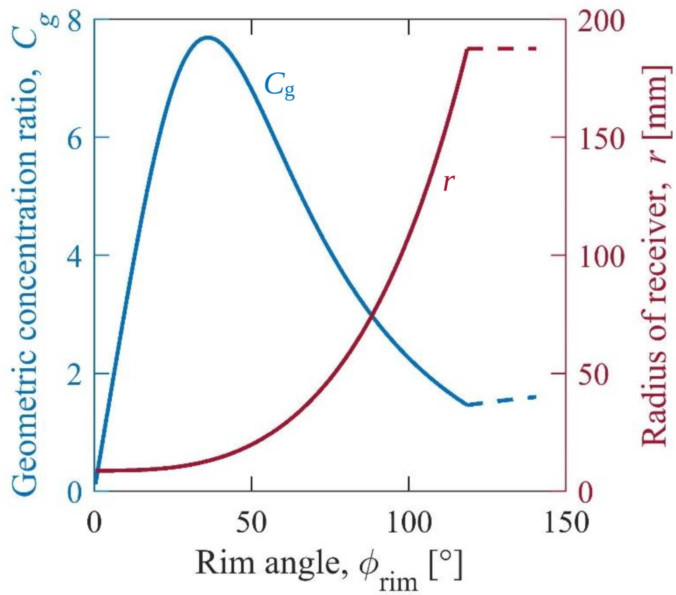

Figure 2.5. Geometric concentration ratio vs. rim angle for a collector designed for 1° acceptance using the approximate solution. The solid and dashed lines show the 1-reflection and 2-reflection concentration regimes, respectively. The receiver radius corresponds to a mirror radius of R = 1 m.

Figure 2.6 shows the influence of a changing acceptance angle on geometric concentration ratio for several rim angles. It is observed that although smaller rim angles produce the highest geometric concentration ratio, these configurations are more sensitive to changes in acceptance angle. Conversely, while large rim angle designs are low in C_g, they are also insensitive to imperfections in the mirror geometry such that any acceptance angle can be chosen without sacrificing much performance. This is confirmed by the shape of the transmission angle curves in *Section 2.4.3*. This finding is particularly useful since a promising application of the circular trough is as low-cost seasonally or periodically adjustable concentrators [11], [20].

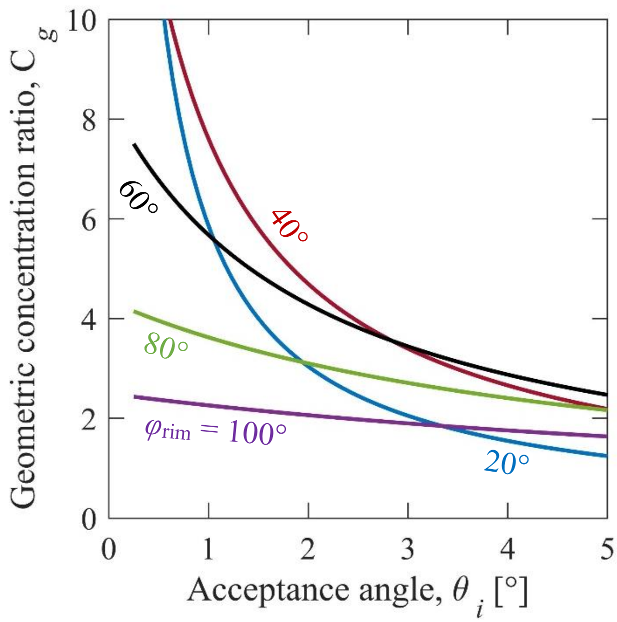

Figure 2.6. Dependence of geometric concentration ratio on acceptance angle for different values of φ_{rim}.

2.3.6. Towards a catalogue of *C*g formulas

With Eq. (2.36) being defined only in terms of the rim angle and acceptance angle, it becomes possible to compare the C_g to that attained by other existing concentrator geometries found in literature. Such a catalogue of C_g formulas would be of use to the optical designer for quickly comparing the performance of different reflector/receiver geometries, as well as performing initial sizing of the main collector components. Towards this goal, **Table 2.1** provides a summary of the C_g formula for several important line-focus concentrator geometries. While the list is not exhaustive, it does provide the limits for the most commonly employed symmetric imaging-type [21] concentrators. In addition to the limit formula, we provide the numerical value for the maximum full collection geometric concentration for each concentrator type (which occur a different rim angles) for an acceptance angle of 1°.

Table 2.1. Catalogue of full collection geometric concentration limits for different concentrator/receiver geometries

Concentrator type	**Limit formula**	**$C_{g,max}$ for 1° acceptance**	**Reference**
Circular mirror with circular receiver	Eq. (2.36)	7.68	This work
Circular mirror with flat receiver[a,b]	$C_g = \begin{cases} \dfrac{4\sin\left(\frac{1}{2}\varphi_{\mathrm{rim}}\right)}{3\sin\left(\frac{1}{2}\varphi_{\mathrm{rim}}\right) - \sin\left(\frac{3}{2}\varphi_{\mathrm{rim}} - 2\theta_i\right)} - 1 \\ \dfrac{\sin\varphi_{\mathrm{rim}}\cos\varphi_{\mathrm{rim}}}{\sin\theta_i\cos\theta_i} - 1 \end{cases}$	12.50	This work[5]
Parabolic trough with flat receiver positioned at the paraxial focus[a]	$C_g = \dfrac{\sin\varphi\cos\left(\varphi+\theta_i\right)}{\sin\theta_i} - 1$	27.65	[21]
Parabolic trough with flat receiver in the optimal position[a]	$C_g = \dfrac{\sin\varphi\cos\varphi}{\sin\theta_i\cos\theta_i} - 1$	27.14	[14], [21]–[23]
Parabolic trough with circular receiver	$C_g = \dfrac{\sin\varphi}{\pi\sin\theta_i}$	18.24	[21]

[a]The subtrahend (−1) accounts for shading on a one-sided absorber

[b]The first and second equation apply over the caustic and rim-ray regime, respectively. The correct regime is the one yielding the smaller C_g for any given θ_i and φ_{rim}.

[5] Material in this section has been submitted for review in Solar Energy under Timpano and Cooper “Concentration ratio for a circular trough with flat receiver”

Figure 2.7 shows a graphical comparison of the achievable C_g of the circular trough/circular receiver configuration vis-à-vis the other common geometries in **Table 2.1**. **Figure 2.7 a)** shows the result for θ_i = 1° where the parabolic trough with flat receiver unsurprisingly achieves the highest concentrations. The circular trough with circular receiver achieves a maximum C_g of 7.688× which is respectable compared to the 18.2× achieved by the parabolic trough with circular receiver given the relative simplicity of the circular profile. For an acceptance angle of 10°, shown in **Figure 2.7 b)**, the circular trough with circular receiver fares even better, matching the C_g of the parabolic trough for small acceptance angles, and with a maximum of 1.595×, just 13% shy of the maximum of 1.833× achieved by the parabola. The rim ray regime can be observed in both **Figure 2.7 a)** and **b)** as the portion of the circ/circ curve which overlaps the parab/circ curve at small rim angles.

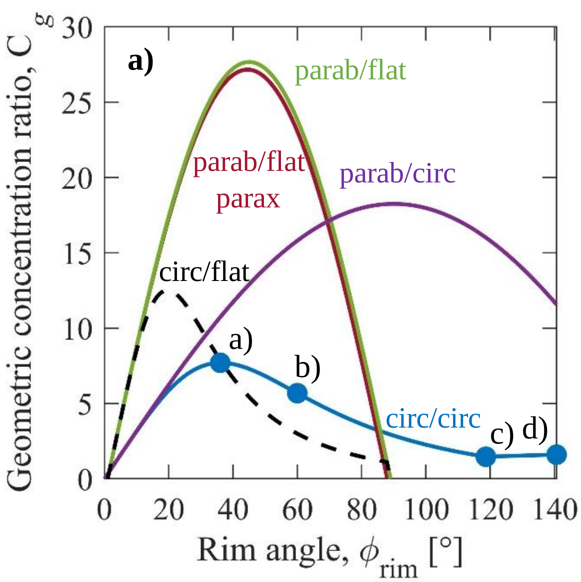

Figure 2.7. Comparison of geometric concentration limits for several concentrator geometries with an acceptance angle of **a)** 1° and **b)** 10°. The curves are labelled as follows: circ/circ – circular trough with circular receiver, circ/flat – circular trough with flat receiver, parab/flat parax – parabolic trough with flat receiver centered at the paraxial focus, parab/flat – parabolic trough with flat receiver placed at the optimal location, and parab/flat – parabolic trough with circular receiver.

2.4. Detailed performance analysis

2.4.1. Geometry of exemplary designs

To further probe the optical performance of the circular trough, we perform a detailed performance analysis on six exemplary designs. **Figure 2.8** shows a schematic of all exemplary designs, labeled a) through f). The markers superimposed in **Figure 2.7** identify the position of each exemplary design within the C_g vs. φ space. Designs a) through d) correspond to a 1° acceptance angle, while Designs e) and f) correspond to a 10° acceptance angle. Design a) corresponds to the maximum in the C_g curve and achieves C_g = 7.688× at φ_{rim} = 36°. Design c) corresponds to the local minimum in the C_g curve at φ_{crit} = 118.66° and achieves C_g = 1.457×. Design b) represents a practical compromise between concentration and compactness and achieves C_g = 5.677× at a rim angle of 60°. Design d) is a two-reflection design at $\varphi_{\mathrm{max,2\text{-}ref}}$ = 70.33° and achieves a slight improvement in concentration (C_g = 1.595×) vis-à-vis Design c).

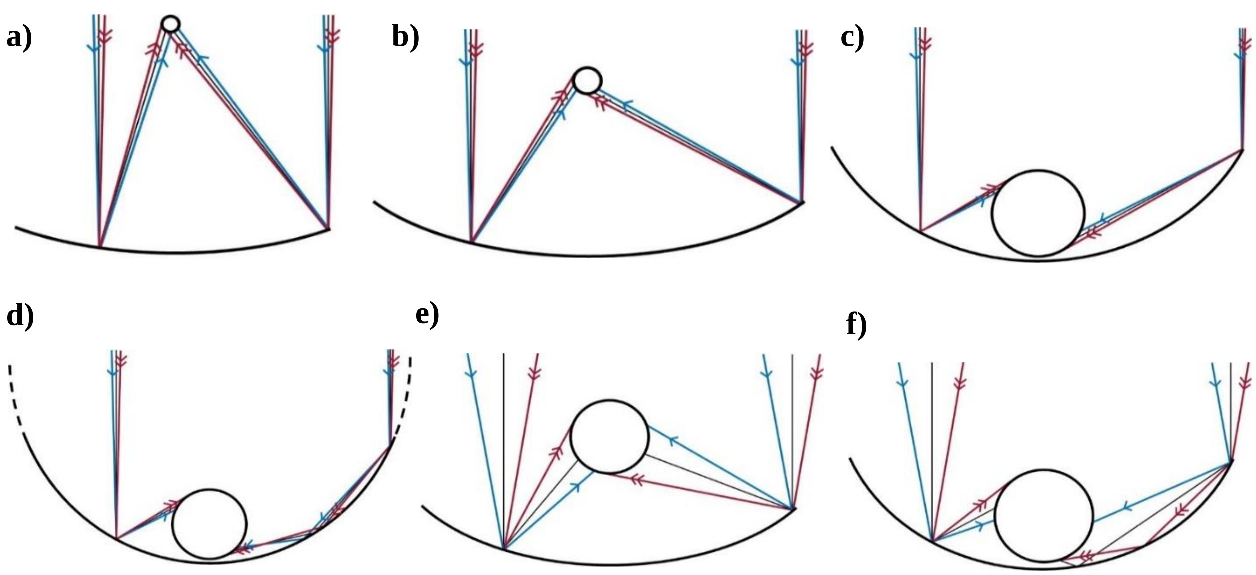

Figure 2.8. Schematics of six exemplary circular trough designs. Designs **a)** through **d)** correspond to an acceptance angle of 1° with rim angles $\varphi_{\mathrm{rim}} = 2\omega_{\mathrm{rim}}$ of 36°, 60°, 118.66°, 140.66° respectively. Designs **e)** and **f)** correspond to an acceptance angle of 10° with rim angles equal to 68° and 126.04° respectively. The corresponding concentration ratios for designs **a)** through **f)** are C_g = 7.689×, 5.677×, 1.457×, 1.595×, 1.478×, 1.242×, respectively. Designs **d)** and **f)** correspond to the two-reflection criterion.

For Designs e) and f), the acceptance angle of 10° was chosen to represent a "non-tracking" solar collector that enables >8 hours of collection while requiring only periodic (seasonal) adjustment [11], [20]. Design e) is located at the maximum of the C_g curve as seen in **Figure 2.7 b)** and achieves C_g = 1.478× at a rim angle of 68°. Design f) is located at the $\omega_{\mathrm{max,2\text{-}ref}}$ and achieves C_g = 1.242× at a rim angle of 126.04°. One additional design, corresponding to a maximum possible rim angle of 180°, is shown by the dashed line in **Figure 2.8**. This extended design achieves a 6.2% improvement in C_g (1.694×) vis-à-vis Design d), but at the expense of some spilled radiation since $\omega_{\mathrm{max,2\text{-}ref}}$ is surpassed. This design is elaborated upon in *Section 2.5.*

2.4.2. Monte Carlo ray tracing procedure

The Monte Carlo ray tracing (MCRT) approach is ubiquitously employed in optical studies due to its ability to incorporate detailed phenomena including sunshape and slope error into the performance analysis. For this reason, MCRT simulations[6] were performed to verify the concentration ratio derivations and further study the optical performance of the circular mirror/circular receiver configuration. First, the MCRT technique was applied to obtain transmission angle curves[7] by uniformly illuminating the inlet aperture with collimated radiation at varying incidence angles. To obtain a full transmission angle curve, the rays were deviated from the optical axis by an incidence angle θ ranging from 0 to 90° in 0.1° increments. The result of the simulation is the intercept factor defined as the radiant power incident on the receiver divided by the radiant power incident on the inlet aperture

$$\gamma = Q_{\mathrm{receiver}} / Q_{\mathrm{i}} \tag{2.37}$$

For all transmission angle cures, the mirror was assumed to have perfect specular reflectance (ρ = 1) and 10^6 rays were used per simulation.

The flux distribution over the surface of the receiver, which is of interest for verifying the uniformity of illumination and mitigating hotspots, is also readily obtained by MCRT. For each

[6] The Monte Carlo ray tracing code used was developed by the PREC research group of Prof. Steinfeld at ETH Zurich

[7] The term "transmission angle curve" has been used historically to quantify the directional acceptance or intercept factor as a function of the incidence angle

exemplary design, we therefore determined the flux distribution for two cases. In the first case, the mirror was assumed to be perfectly specular, and the source was chosen to fill the acceptance cone of the concentrator[8]. In the second case, we consider a realistic case which includes both slope error and terrestrial sunshape. For the sunshape, we use the model of Buie et al. [24] with a circumsolar ratio (CSR) of 5%. For the slope error we assign a random error to the local surface normal following a bivariate Gaussian with standard deviation of 2.9 mrad. Together with the sun (assuming the sun is roughly a 4.1 mrad Gaussian [25]), this results in approximately 95% of the reflected ray cone fitting inside the acceptance angle[9]. For all flux distributions 10^9 rays were used.

2.4.3. Transmission angle curves

Figure 2.9 shows the transmission angle curve for Design b) which features an acceptance angle of 1° and a rim angle of 60°, and highlights the notable behavior exhibited by the circular trough/circular receiver configuration. Most importantly, we observe four distinct zones in the transmission angle curve so long as $\omega_{\mathrm{max,2\text{-}ref}}$ is not surpassed. A snapshot of the MCRT simulation is superimposed in **Figure 2.9** to highlight the details of each transmission zone. Zone I spans from 0° to θ_i, in which the value of intercept factor is 1, confirming the fulfillment of full collection. Zone II occurs immediately following the acceptance angle and terminates at a local minimum occurring at some multiple of θ_i. In Zone II, some spillage occurs resulting in $\gamma < 1$. In Zone III, all rays reflecting off the mirror miss the receiver. However, the nonzero intercept factor can be understood by the fact that some rays strike the receiver directly from the top, as seen in the inlay in Zone III in **Figure 2.9**. As a result, the intercept factor in this zone is simply equal to

$$\gamma = \frac{D_{\mathrm{abs}}}{A_i \cos\theta} \tag{2.38}$$

where $D_{\mathrm{recevier}} = 2r$ is the projected width (diameter) of the receiver, θ is the incidence angle, and $A_i\cos\theta$ is the projected width of the mirror. As the incidence angle increases, the projected width

[8] For example the source for designs a) through d) was a Lambertian cone with a half angle of 1° whose main direction is centred on the optical axis.

[9] Given 2.9 mrad for the slope error (acting on the normal) and 4.1 mrad for the sun, the total reflected ray error standard deviation is approximately σ = sqrt((2·2.9 mrad)^2 + (4.1 mrad)^2) = 7.10 mrad. For a bivariate Gaussian, 95% of the energy lies within 2.45 standard deviations, which equates to 2.45·7.10 mrad ≈ 1°.

of the mirror decreases while the projected width of the receiver stays the same causing an apparent increase in the intercept factor. In Zone IV, all rays are spilled, and no radiation is directly incident on the receiver[10]. It should be noted, however, that Zone IV is simply an artifact of the simulation conditions. In reality, incoming solar radiation would not be limited to the inlet aperture defined by the simulation and some rays would directly strike the receiver as in Zone III. Nevertheless, Zone IV is stated for completeness.

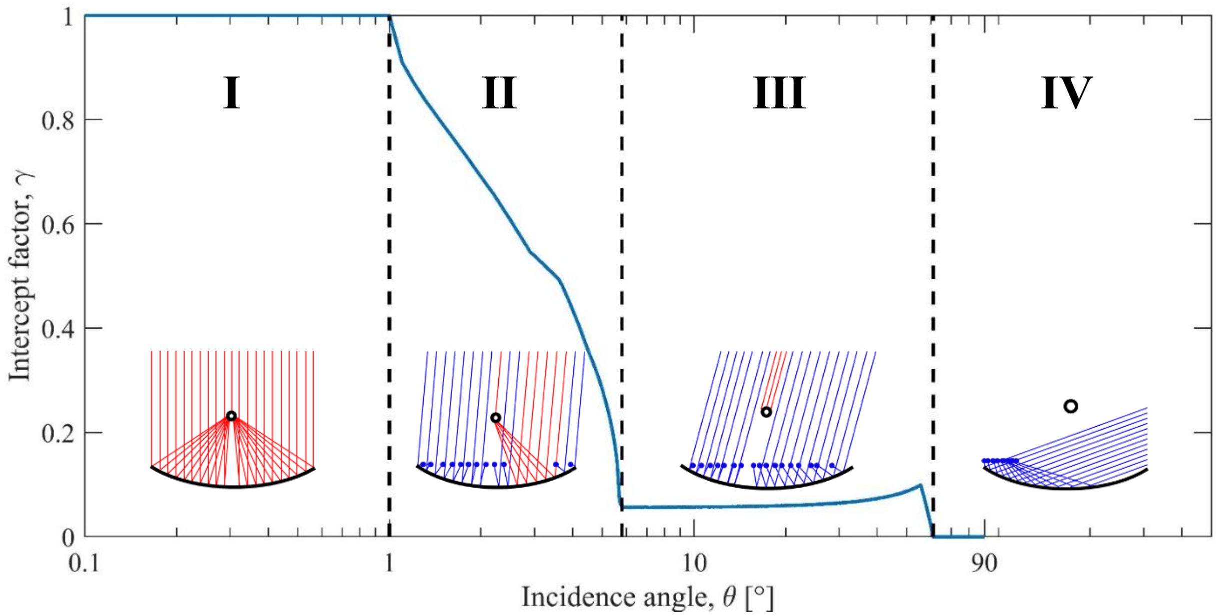

Figure 2.9. Full transmission angle curve for Design b) which has θ_i = 1° and φ_{rim} = 60°. The curve is divided into four separate transmission zones. Each zone is paired with a snapshot of the MCRT to highlight the salient features of each zone.

Figure 2.10 shows the resulting transmission angle curves for the 6 exemplary designs. With the full transmission behavior examined in detail for Design b) in **Figure 2.9**, we focus on Zones I and II in **Figure 2.10**, which are the most important zones for normal collector operation. As can be seen from **Figure 2.10** , larger rim angle designs are more tolerant to larger incidence angles. For example, for an acceptance angle of 1° and φ_{rim} = 36° (Design a), all rays are spilled at an incidence angle approximately equal to 2° and all absorbed radiation is intercepted directly by the receiver. Conversely, for the same acceptance angle and φ_{rim} = 140.66° (Design d), the concentrator

[10] In reality some radiation would be incident on the receiver even in Zone IV. However, for the purposes of determining the intercept factor, it is logical to illuminate only the inlet aperture of the concentrator rather than the full ground plane. Thus, for large enough incidence angles, the receiver will be missed as seen in the inlay for Zone IV in **Figure 2.9**.

continues to reflect some radiation up until an incidence angle of 35.7° (the end of Zone II). Additionally, the intercept factor at the end of Zone II is larger for larger rim angles. For example, the intercept factor at the end of Zone II is 0.04 and 0.43, for cases a) and d) respectively.

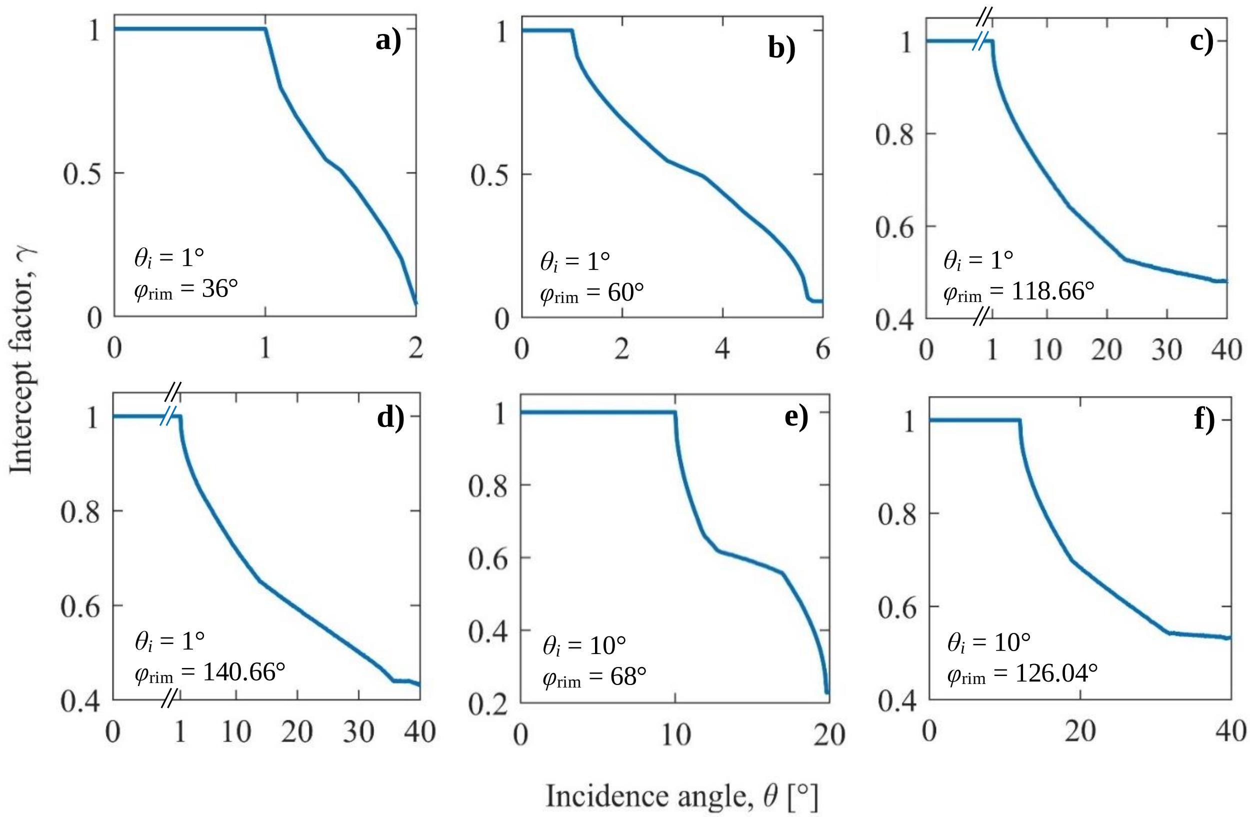

Figure 2.10. Transmission angle curves for the six exemplary designs specified in **Figure 2.8**

2.4.4. Flux distributions

Figure 2.11 shows a 3D view of the flux distribution for Design b) for the realistic case, and **Figure 2.12** shows a 2D representation of the flux distribution for the remaining designs. In both figures the concentrated flux (irradiance) is normalized by the direct normal irradiance (DNI) to yield the local flux concentration

$$C_{\text{flux}} = q_{\text{local}} / \text{DNI} \tag{2.39}$$

Among all the designs, a peak flux concentration of 30.2 suns is observed for design a) for the realistic case. Several interesting phenomena occur at larger rim angles. First, as expected, the value of the peak flux decreases with increasing rim angle. Additionally, at larger rim angles, the receiver significantly shades a portion of the mirror directly behind it. This is evidenced by the reduction in the flux concentration at ψ = 0° from a non-zero value in Design a) to a near-zero value in Design b) and identically to zero in Designs c). The flux at ψ = 0° does not drop to zero for the two-reflection Designs d) and f) because rays incident near the rim find their way to the bottom of the receiver after two reflections off the mirror c.f. **Figure 2.2 c)**. Simultaneously, the region of highest concentration migrates away from ψ = 0° with increasing rim angle. This results from a shift in the position of the receiver toward the vertex of the mirror, which causes the caustic to graze the receiver on its top side. Unique to Design d) is the existence of a strong second peak which occurs at smaller values of ψ. This is indicative of a secondary caustic forming from the rays experiencing two reflections before striking the receiver. A very small second peak can be observed in the ideal case (solid line) for Design f), which is also a two-reflection design.

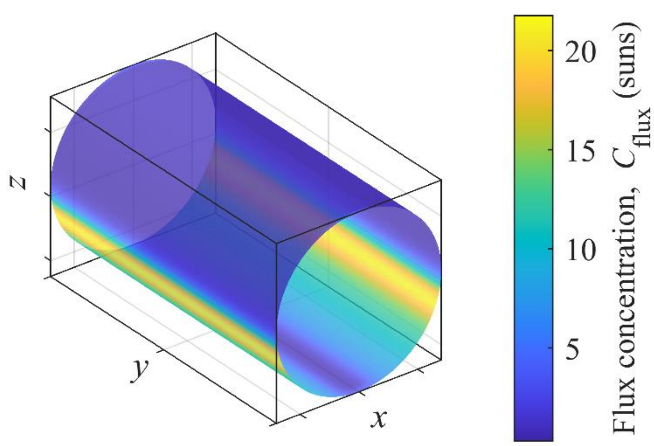

Figure 2.11. 3D flux distribution corresponding to the Design b) for the realistic case including surface error and sunshape.

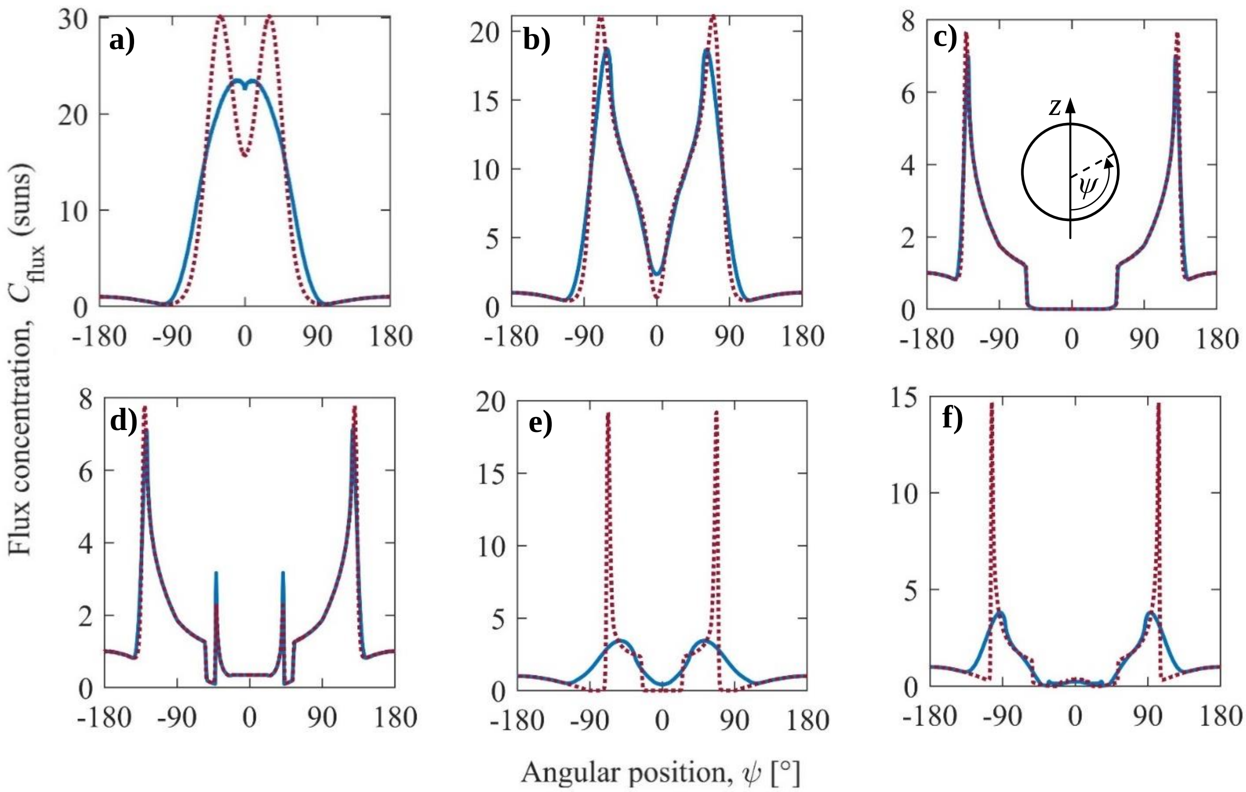

Figure 2.12. Flux distributions corresponding to the exemplary designs specified in Figure 8. Solid lines correspond to Case 1: perfectly specular mirrors with a source that fills the acceptance cone. Dashed lines correspond to Case 2: a realistic case with a normally distributed slope error of 2.9 mrad and a source following a terrestrial sunshape with CSR = 5%.

2.5. Practical design considerations

The designs presented thus far are of particular significance when comparing the construction costs of various solar trough concentrators. While the parabola generally outperforms the circular concentrator in terms of concentration, it often requires complex methods of producing the geometry thus increasing the associated construction costs. The circular trough is a natural choice for inflated designs as a membrane will naturally assume a circular cross section upon inflation [11]. Therefore, even though a perfect circle underperforms a perfect parabola, in practice it is likely much easier and less costly to approach a perfect circle than it is a parabola. For this reason, it is likely that the most practical embodiments of the circular trough will utilize an inflated polymer film construction. Nevertheless, some remarks should be made on how the mirror construction could constrain the rim angle, and the resulting effect this would have on the achievable C_g. The C_g formula in Eq. (2.36) assumes that the mirror spans from $-\varphi_{\rm rim}$ to $\varphi_{\rm rim}$. Selection of an appropriate rim angle depends on a balance of concentration, compactness, and material utilization. For an inflated polymer collector, perhaps the simplest approach is to construct a cylinder where the top half (exactly one half of the circumference) comprises a transparent polymer film, and the bottom half comprises a reflective film. This would result in an $\omega_{\rm rim}$ of identically 90° for the mirror, which in turn implies a rim angle of $\varphi_{\rm rim}$ = 180°. A concentrator meeting this condition is shown by the dashed line in **Figure 2.8 d)**. This extended concentrator has the same receiver size as Design d), but its inlet aperture area is increased by a factor sin(180°/2)/sin(140.66°/2) c.f. Eq. (2.6) to yield an overall geometric concentration of 1.694×. However, since this value of $\omega_{\rm rim}$ is above $\omega_{\rm max,2\text{-}ref}$, the resulting concentrator will not achieve full collection, as some rays will be spilled through the gap between the bottom of the receiver and the vertex of the mirror. The question then arises: is it better to constrain the mirror to the maximum $\varphi_{\rm rim} = \varphi_{\rm max,2\text{-}ref}$ = 140.66° (for θ_i = 1°) and maintain full collection, or to extend the mirror to $\varphi_{\rm rim}$ = 180°? To probe this tradeoff, we simulated the extended $\varphi_{\rm rim}$ = 180° concentrator, and found an intercept factor of 0.9585. Multiplying this intercept factor with the geometric concentration yields the average flux concentration, which amounts to 1.623 suns. Therefore, even though some rays are spilled, the average flux concentration increases, albeit marginally, vs. the 1.595 suns achieved by the full collection design, d). Additionally considering the potential convenience of having the mirror spanning exactly one-half a circle, it is likely that this extended $\varphi_{\rm rim}$ = 180° design is a more practical choice. Beyond this specific design, the above analysis shows how the C_g formula can be a useful tool for establishing a baseline design which can then be elaborated upon by combining practical considerations with more detailed MCRT simulations.

2.6. The need for tracking

In section 2.1 it was shown that the concentration ratio of a solar collector is inversely proportional to sine of the acceptance angle. Then, in order to maximize the concentration ratio, the acceptance angle is to be made as small as possible, approaching the limit of the angular size of the sun. These operating conditions, however, are contingent on the position of the collector with respect to the sun. For example, consider a general configuration of a vertically oriented solar collector as shown in **Figure 2.13**. For a given acceptance angle, θ_i, full collection occurs when the sun vector, $\vec{s}$, is coplanar with the axial plane. Since, to an earthly observer, the sun appears to move throughout the sky, so to must the collector in order to preserve these conditions. Simply put, the collector must be able to track the sun throughout the day.

Figure 2.13 also shows an important parameter, ϑ, called the skew angle. The skew angle is defined as the angle between the aperture normal, $\hat{n}$, and the sun vector, $\hat{s}$. While the collector is able to rotate such that the aperture normal is coplanar with the axial plane, there are insufficient degrees of freedom to achieve normal incidence for all rays [4]. Therefore, the irradiance that will actually be captured is reduced by a factor of $\cos\vartheta$. Fortunately for a vertical collector, the skew angle is easily quantified and is simply equal to the angle of elevation.

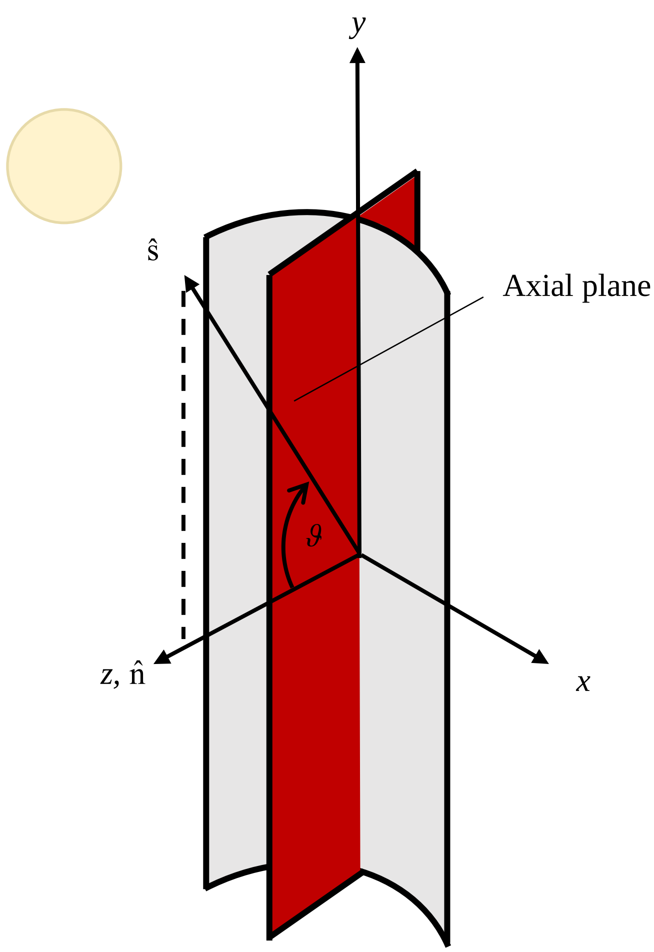

Figure 2.13. Vertically oriented solar collector perfectly tracking the sun. $\hat{n}$ denotes the inlet aperture normal and $\hat{s}$ denotes the sun vector. The global coordinate system is (*x*, *y*, *z*). The axial plane is the plane formed with the *y*-axis and the inlet aperture normal.

2.7 Other important quantities

While the majority of this chapter was dedicated to understanding a few fundamental optical quantities that form the theory behind solar trough concentrators, there are still several quantities that have yet to be discussed. For the sake of clarity, the extra background will be provided in subsequent chapters as they are needed. In short, *Chapter 3* will present the structural theory behind erecting a vertical trough concentrator, *Chapter 4* will present some additional optical quantities from a simulative approach, and *Chapter 5* will present thermal quantities as part of a thermal simulation.

Chapter 3

Design and material selection

In the previous chapters, it has been noted that one of the primary objectives of the vertical circular concentrator is to drive down the cost per m^2 of aperture area. The minimization of cost occurs primarily in two parts: due to the simple construction of the circular geometry in comparison to the traditional parabola and due to the major reduction of structural framing. In this chapter, the design and methodology of constructing a circular concentrator will be discussed.

3.1. Structural design modelling

The design of inflatable cantilevered beams is of great importance to space and aerospace applications [26]. The inflation pressure is used to place a synthetic fabric or thin-film beam into a state of tension, thus enabling it to carry loads. However, the inflatable beam is prone to local buckling (characterized by a wrinkle) and possibly collapse if subject to significant external forces [26]. Fortunately for the current work, a plethora of previous research has been conducted into quantifying the mechanics of inflatable cylindrical beams including the accurate prediction of the wrinkling moment.

Summarized by Zhu et al., there are two approaches to modelling the inflated beam found in literature: the beam-type and the membrane/shell type [26]. In the former, the inflated beam is assumed to behave according to Euler-Bernoulli beam theory, wherein the cross-section remains unchanged as it is deformed. The two methods that will be considered for the current research is the wrinkling moment developed with respect to compressive stresses as studied by Leonard et al. [27] and Comer and Levy [28] and the wrinkling moment developed with respect to compressive strains as studied by Main et al [29].

3.1.1. Wrinkling and collapse moments

The method studied by Leonard et al. [27] and Comer and Levy [28] and verified in the experiment by Zhu [26] considers an inflated cylindrical beam subject to a lateral tip load as shown in **Figure 3.1**. According to Euler-Bernoulli beam theory, the longitudinal stresses in the fabric of the wall will be a combination of the longitudinal stress produced by tension (as a result of the inflation pressure) and the bending stress produced by the load, whereas the circumferential stress consists only of the hoop stress. Then, according to Stein and Hedgepeth, there are three possible stress regimes classified by the principal stresses in the fabric of the membrane [30]

$$\begin{array}{ll} \sigma_{11} = \sigma_{22} = 0 & \text{Membrane is unloaded and wrinkle free} \\ \sigma_{11} > \sigma_{22} > 0 & \text{Membrane is taut and wrinkle free} \\ \sigma_{11} > 0, \sigma_{22} = 0 & \text{Membrane is wrinkled} \end{array} \tag{3.1}$$

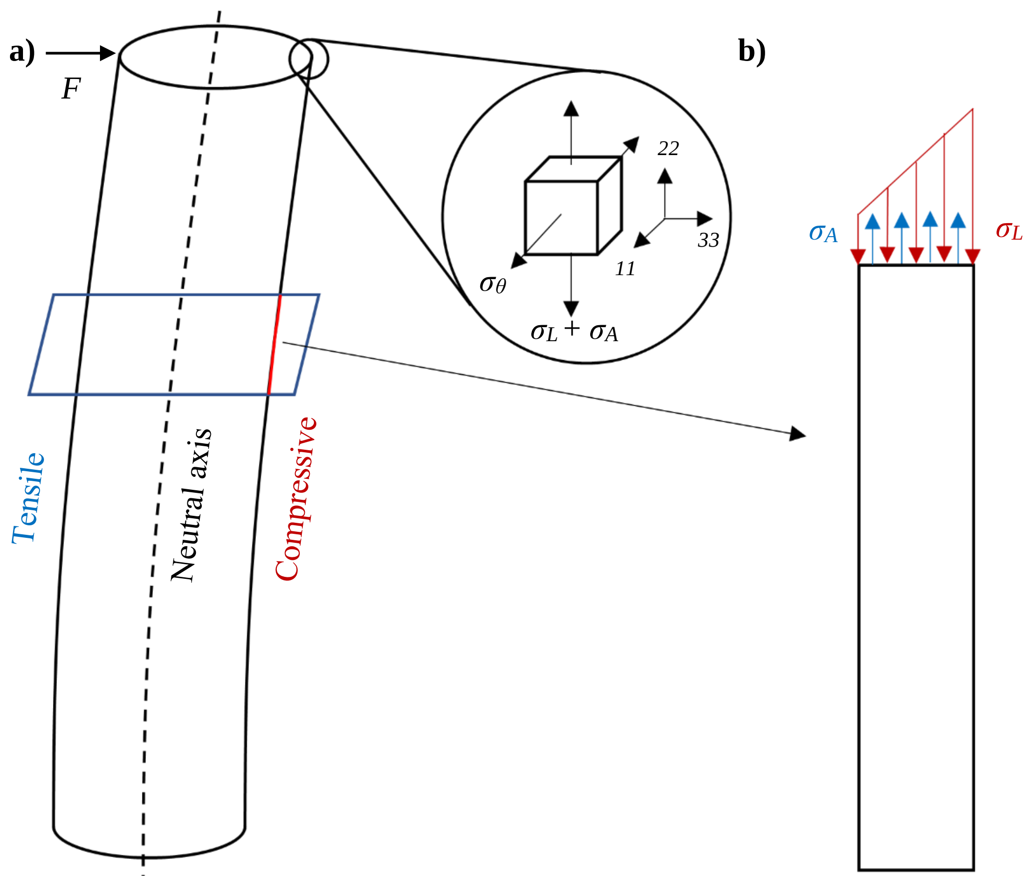

Figure 3.1. State of stress within an inflated membrane undergoing a lateral tip load. **a)** displays the stress cube at the first wrinkling point; and **b)** shows the stress distribution within the wall at the first wrinkling point. F is the applied load, σ_A is the bending stress due to the applied load, σ_L is the longitudinal stress produced by the inflation pressure, and σ_θ is the hoop stress.

Essentially, an inflated member is represented mathematically by a non-zero principal stress in the circumferential direction. Then, since an inflated member cannot support a compressive stress, a wrinkle will form when the second principal stress is exactly zero, indicating that the longitudinal and applied stresses are balanced in the fabric of the beam. The first wrinkling point will always occur on the side of the inflated beam where the applied load produces a maximum compressive stress (which will be the furthest away from the neutral axis as shown in **Figure 3.1 b)**. Solving for the principal stress yields the following equation for σ_{22}

$$\sigma_{22} = \sigma_L - \sigma_A \tag{3.2}$$

Setting Eq. (3.2) equal to 0 and solving yields the following expression for the stress-based wrinkling moment denoted by subscript STN for Stein [26], [30]

$$M_{W,\mathrm{STN}} = FL = \frac{\pi p R^3}{2} \tag{3.3}$$

As the applied load increases beyond this critical value, the wrinkle propagates in the axial and circumferential direction. Collapse occurs when the wrinkle has progressed all the way to the lowest extreme fibres (wraps all the way around the beam) as shown in **Figure 3.2** [27]. The collapse moment can then be determined from a simple force balance. At collapse, the lowest extreme fibres must balance the internal pressure of the system. If the resulting pressure force is given by *pA*, then the lowest extreme fibres must resist a moment equal to *pAR* [27]. The collapse moment is then given as

$$M_{C,\mathrm{STN}} = \pi p R^3 \tag{3.4}$$

Main et al. argued that the stress-based wrinkle criterion was insufficient, as the axial strain became compressive prior to the axial stress due to the Poisson effect [26], [29], [31]. The strain-based wrinkle criterion was then formulated as

$$\varepsilon_{x,\min} = \frac{1}{E}\left(\sigma_{x\_min} - \nu_{\theta x}\sigma_\theta\right) = \frac{1}{E}\left(\frac{pR}{2t} - \frac{FL}{\pi R^2 t} - \nu_{\theta x}\sigma_\theta \frac{pR}{t}\right) = 0 \tag{3.5}$$

Thus, the strain-based wrinkling moment is found by solving the above equation and is denoted by subscript M for Main [29], [31]

$$M_{W,\mathrm{M}} = FL = \frac{\pi p R^3}{2}\left(1-2\nu_{\theta x}\right) \tag{3.6}$$

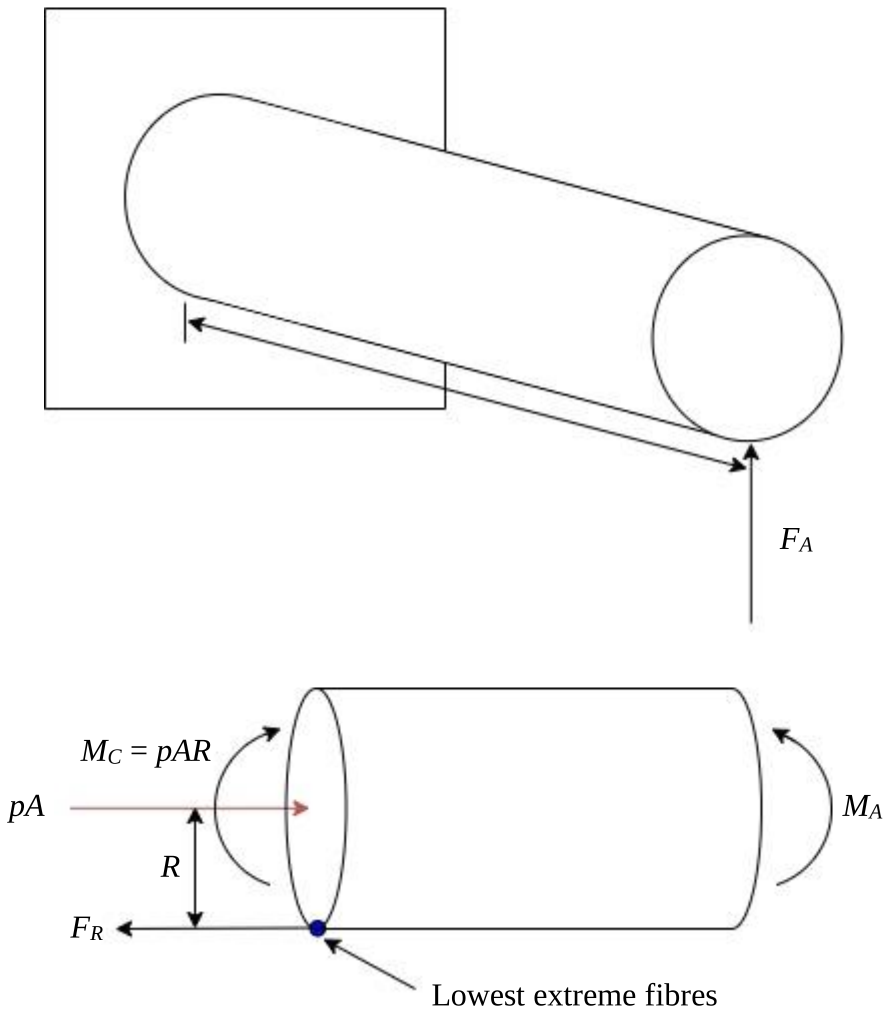

Figure 3.2. Collapse moment as identified by a simple cantilever beam undergoing applied force F_A and corresponding applied moment M_A. The internal pressure is pA, the resultant force at the lowest extreme fibres is F_R, and the collapse moment is M_C.

Using a similar argument to find Eq. (3.4), the strain-based collapse moment is found as [26]

$$M_{C,\mathrm{M}} = \pi p R^3\left(1-2\nu_{\theta x}\right) \tag{3.7}$$

Zhu et al. attempted to verify the stress- and strain-based wrinkle criterion using a fibre reinforced polyethylene hose with $\upsilon_{\theta x}$ = 0.14 [26]. In their work, both the stress- and strain-based wrinkling moment were non-dimensionalized according to the following equation

$$m^* = \frac{M}{\pi p R^3} \tag{3.8}$$

The non-dimensional wrinkling moments were given as $m_{W,S}^*$ = 0.5 and $m_{W,M}^*$ = 0.36, for the Stein and Main methods respectively [26]. Zhu et al. concluded that the actual wrinkling moment occurred somewhere in between the two and the stress-based collapse moment served as an upper bound for the actual collapse [26]. The strain-based collapse moment served to be inaccurate and is only stated here for completeness.

For the works presented here, only the stress-based wrinkle criterion is adhered to, as the lack of equipment renders $\upsilon_{\theta x}$ incalculable. In addition, the stress-based wrinkle criterion is more appropriate as it does not require extra material parameters which could exacerbate the difference between the fibre reinforced polyethylene hose used in the works by Zhu et al., and the thin films used for the concentrator.

3.1.2. Deflection and stability of horizontal vs. vertical solar concentrators

The studies mentioned previously sought out to determine the wrinkling and collapse moments of inflated cylindrical beams to quantify their load carrying capacity in space and aerospace applications. While the equations can be extended to the present case, they do not fully describe the permissible operating conditions for a solar concentrator. For example, the solar concentrator may also deflect due to wind-loading. Therefore, it becomes important to quantify the deflection (and later, the optical inefficiencies due to deflection) as well as determine the geometrical parameters which produce an optimal solar concentrator.

For the purposes of simplicity, wind-loading will be taken as a uniformly distributed load over the length of the concentrator. Assuming Euler-Bernoulli beam theory applies, the elastic curve equations by R.C. Hibbeler [32] for a cantilevered beam experiencing a distributed load can be used to describe the slope and deflection of the vertical concentrator (subscript *V*)

$$\theta_V = \frac{\omega l^3}{6EI} \tag{3.9}$$

$$\delta_V = \frac{\omega x^2}{24EI}\left(x^2 + 6l^2 - 4lx\right) \tag{3.10}$$

where ω is the distributed load, l is the length of the beam, E is the elastic modulus, and I is the area moment of inertia [32] equal to the following

$$I = \pi R^3 t = \frac{\pi}{8} D^3 t \tag{3.11}$$

A similar derivation can be applied to a simply supported inflated beam (pinned at both ends) subject to a uniform load, representative of a horizontal concentrator (subscript *H*)

$$\theta_H = \frac{\omega l^3}{24EI} \tag{3.12}$$

$$\delta_H = \frac{\omega x^2}{24EI}\left(l^3 - 2lx^2 + x^3\right) \tag{3.13}$$

The maximum deflection in the vertical configuration occurs at the tip of the beam and is given by substituting $x = L$, while the maximum deflection in the horizontal configuration occurs at the centre of the beam and is given by substituting $x = ½L$. The maximum deflections are then calculated as

$$\delta_{V,\max} = \frac{\omega L^4}{8EI} \tag{3.14}$$

$$\delta_{H,\max} = \frac{5\omega L^4}{384EI} \tag{3.15}$$

From Eqs. (3.14) and (3.15), it can be seen that for equivalent geometrical parameters, the vertical concentrator experiences 9.6 times the deflection of its horizontal counterpart. It is also important to note that reinforcing members can be added between the fixed ends to the horizontal configuration to further reduce the maximum deflection, whereas the vertical configuration must be unchanged to keep within the initial objective of reducing cost.

It remains to be determined the set of geometrical parameters *L*, *D*, and *t* that produces a concentrator that operates under the widest range of environmental conditions. To that end, the dependence of deflection on aspect ratio (defined as *L/D*) was identified. The distributed load is identified as the drag force per unit length

$$\frac{F_D}{L} = \omega = \frac{1}{2} C_D D \rho V^2 \tag{3.16}$$

where C_D is the coefficient of drag and ρ and V are the density and velocity of air, respectively. Eq. (3.16) is then substituted into Eq. (3.14) and non-dimensionalized to give

$$\frac{\delta_{V,\max}}{D} = \frac{1}{2\pi} \frac{C_D \rho V^2}{E} \frac{L^4}{D^3 t} = \frac{1}{2\pi} \frac{P_{\text{wind}}}{E} \frac{AR^4}{t/D} \tag{3.17}$$

Eq. (3.17) is split up into three non-dimensional groups. The first group (or coefficient) affords comparison to the deflection experienced by other concentrator configurations. That is, the non-dimensionalized deflection equation is general to all concentrator configurations (horizontal or vertical) with only the first group changing to scale the magnitude of deflection experienced. The second group is the ratio of wind pressure to the Young’s modulus of the material of the outer-envelope and represents the relative stiffness of the collector. The last group shows how deflection scales with the geometrical parameters. From Eq. (3.17) it can be seen that the non-dimensionalized deflection is highly sensitive to changes in aspect ratio, scaling to the power of 4.

The geometrical parameters that constitute a structurally optimized solar concentrator then needed to be determined. To that end, we impose two constraints based on the previous discussion. First, the constraint on moments states that the applied moment must be less than or equal to the wrinkling moment provided by Stein to ensure that the load-deflection relationship remains linear.

Non-dimensionalizing with respect to $\pi p R^3$ to remove the dependence on physical parameters, this condition can be written mathematically as

$$m^* \le \frac{M_{W,\mathrm{STN}}}{\pi p R^3} = 0.5 \tag{3.18}$$

It will be later shown in *Section 4.1.6.* that the optical performance of the collector reduces with deflection produced by wind-loading. The exact reduction in optical performance is dependent on the deflection of the receiver in relation to the outer-envelope. However, the receiver is in a statically indeterminate state and therefore the exact receiver deflection is unknown. For this reason, we impose a permissible deflection at the tip of the beam using Eq. (3.17) to pre-emptively mitigate these losses. This constraint states that the deflection at the tip must remain less than 25% of the diameter, written mathematically as

$$\frac{\delta}{D} \le 0.25 \tag{3.19}$$

In order to proceed with the above calculations, a material was first chosen to specify both the thickness and the elastic modulus. Then, since the diameter appears in the denominator of the last term of Eq. (3.17), it was fixed at approximately 12" corresponding to commercially available components. We then set Eq. (3.17) equal to 0.25 (as per the condition in Eq. (3.19)) and solve for the velocity. For each aspect ratio chosen, the coefficient of drag was taken from Cengel and Cimbala [33]. Finally, we choose a characteristic value of 1 psi[11] to calculate the non-dimensionalized moment equation. **Figure 3.3** shows the results of this analysis assuming a concentrator made of polyester with elastic modulus equal to 920 MPa, thickness of 0.002", diameter of 11.27", and an internal pressure of 1 psi.

The results of **Figure 3.3** suggest that the aspect ratio be as small as possible such that the constraints are satisfied for larger wind-loads. However, lower aspect ratios yield incompact designs. Thus, we suggest that the aspect ratio be in the range of 5-10. In this range, the constraint on moment is typically violated first. However, this constraint can be loosened as small wrinkles may be permissible and because the stress-based wrinkle moment is still a conservative estimation.

[11] The value of 1 psi corresponds to an experimentally determined pressure from the laser experiments in *Chapter 6*.

That is, the load-deflection curve is still somewhat linear past the wrinkling moment point [26]. The specific aspect ratio throughout this text changes across experiments, however, the final thermal prototype uses an aspect ratio of 9.

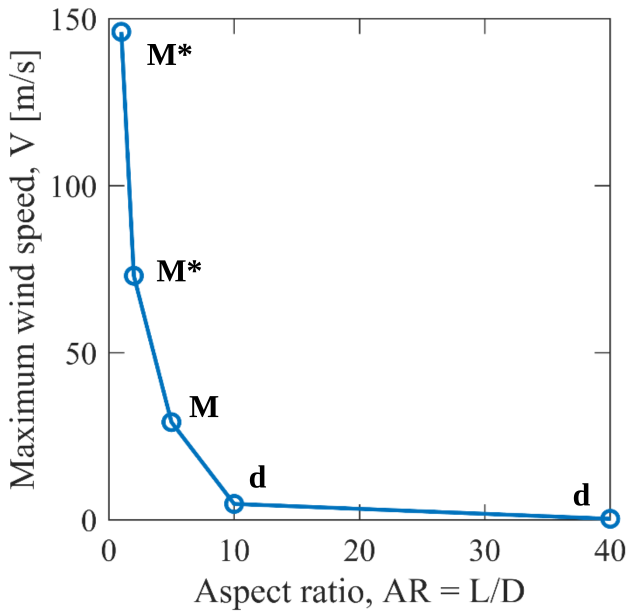

Figure 3.3. A plot of maximum wind speed versus aspect ratio. The data points correspond to known values of the drag coefficient by Cengel and Cimbala. The M or d beside each data point determines which criterion fails first, *M* for moment and *d* for deflection. The asterisk represents failure in the turbulent regime, where the values for the drag coefficient may not be entirely correct (Cengel and Cimbala give the drag coefficient only for the laminar regime).

3.2. Construction of a vertically oriented solar concentrator

Construction of an inflated trough concentrator begins with the polymer envelope comprising two sections – a mirror capable of reflecting incident radiation to a focus and a transparent top-sheet used to enclose the membrane. Despite its seemingly simple nature, several variants of this subassembly exist within literature. The arcspline concentrator produced by the research group at ETH Zurich [9] and the "double-bubble" concentrator [4] are just two of many potential configurations. For the present work, we prefer the simplest approach of a half-mirror half-transparent topsheet, herein referred to as "the bag", to minimize complexity and cost.

3.2.1. Bag materials

The choice of mirror material results from three factors: high specular reflectance, high tensile strength, and low cost. Fortunately, previous works have shown metallized polyester (or Mylar) to be an ideal candidate. Metallized polyester films have a high yield strength of around 98 MPa [4], an extremely low cost per m^2 [4], and exhibits a very high specular reflectance of around 0.89 [12]. It is for these reasons that metallized polyester was used for all configurations performed in this work.

On the other hand, the transparent top-sheet must exhibit several qualities including a high solar transmittance, capable of resisting weathering, and must be low-cost to accommodate the initial project objectives [4]. In addition, a low coefficient of friction is preferable as it essentially makes these membranes self cleaning [4]. It is for these reasons that fluoropolymers such as ETFE (τ = 0.92) and FEP (τ = 0.96) are typically used. One such configuration of the vertical solar collector was constructed using a half-ETFE half-metallized polyester membrane. However, due to the mismatch in yield strength between the two materials, the ETFE yielded in tension quite quickly causing plastic deformation as seen in **Figure 3.4**. Hence, FEP was not a suitable choice either as the yield strength is less than that of ETFE (12 MPa vs. 19 MPa, respectively [4]). It was for this reason that clear polyester was chosen. While clear polyester is not as transmitting (τ = 0.874) as either fluoropolymer, the shape of the bag can be ensured as the two materials are nearly identical.

Figure 3.4. A vertical concentrator with a bag made from metallized polyester and ETFE experiencing plastic deformation due to the mismatch in the yield strength.

3.2.2. Bag construction

Due to the delicate nature of constructing the bag, specific steps were taken to reduce wrinkling and surface errors. The process is both outlined here and shown visually in *Appendix A.*

1. Starting with the metallized polyester, one edge of the sheet is cut square.

2. Clamp the four corners of the sheet to a rigid surface and pull taut. This was achieved by clamping the sheet to two separate workbenches and separating the workbenches such that any visible wrinkling and/or deformities disappeared.
3. Cut the sheet square and to length at the opposite side.
4. With the sheet still pulled taut, scribe intermittent measurements of the desired width across the film. An extra 1" was allocated for both sides of the mirror material to provide an overlap for when the sheet is taped.
5. Lay a large flat surface of equal length to the desired length over top the scribe marks and clamp both edges down square to the film. This was done with an 8′ ruler. Cut the film using the flat surface as a guide.
6. Scribe intermittent measurements of the desired overlap across the non-metallized side of the mirror (1" for the present case).
7. Align a large flat surface or ruler across the scribe marks and clamp down. Scribe a lengthwise line using the surface or ruler as a guide.
8. Remove all clamps and intermittently tape down the film across its length.
9. Delicately (so as to not induce any wrinkles) fold the opposite side over.
10. Line up the free end of the sheet with the taped end so as to not induce any shape error. Tape can be used to hold down the free end once both edges are perfectly coincident.
11. Crease the seam.
12. Repeat steps 1-11 for the transparent sheet. Steps 6-7 may be skipped.
13. Clamp the folded metallized polyester sheet to the work surface and pull taut.
14. Bring the free ends of the two films together such that the mirror material is seated inside the transparent sheet. Align the free edge of the transparent sheet overtop the scribed line across the length of the mirror.
15. Manually eliminate any leak pathways in the overlapping region.
16. Using two skilled persons, cut a length of tape equal to the length of the bag. Several pieces of tape should not be used as this increases the chances of leaks forming.
17. With both persons holding one end of the tape, simultaneously place the tap over the seam. It is critical that one person apply pressure to all sections of the tape once it has been placed.

3.2.3. Bag sealing

Throughout all prototypes, the sealing method at the bottom of the concentrator remained constant. A 3" tall and 11.27" in diameter duct flange was procured and used as the point of contact for the bag. The diameter was chosen considering the aspect ratio analysis performed earlier, as well as considering commercially available components. The bag is seated around the duct flange and wrapped by a silicone gasket. Several hose clamps are tightened around the silicone gasket to form an airtight seal. The gasket also provides a buffer to protect the bag from being punctured. **Figure 3.5** displays the interface between the bottom seal and the duct flange.

The top seal varied across the works presented here. The very first prototype, made entirely of polyethylene and used strictly for mechanical validation, was impulse welded at the free end to form a permanent airtight seal **Figure 3.6 a)**. This, however, proved to be challenging to work with if modifications were to be made. For example, in the optical and thermal prototypes it was imperative that the seal was capable of being removed if necessary. In the former, a screw-on pail lid and retaining ring were used to seal the top. The bag was pulled through the retaining ring and the pail lid was inserted inside the bag itself. The lid was then screwed onto the retaining ring where a seal was formed as shown in **Figure 3.6 b)**. While this method proved to be somewhat effective, it did have its challenges. Because the pail lid and bag were matched in diameter, it was difficult to fit the pail lid inside the bag without tearing the fabric. Additionally, placement of the receiver within the bag is a critical parameter, and the pail lid provided no means of precisely fixing the receiver vertically. It was for this reason that the final prototype utilized two half-rounds that provided a uniform clamping pressure across the top of the bag as shown in **Figure 3.6 c)**. In practice, the end of the outer envelope was punctured intermittently to allow for a screw to pass through. Then, counterbored holes were made into each of the half rounds such that a screw could clamp the two together, through the holes made in the fabric. This method provided the cleanest means of creating an airtight seal and allowed for the receiver to be positioned accordingly.

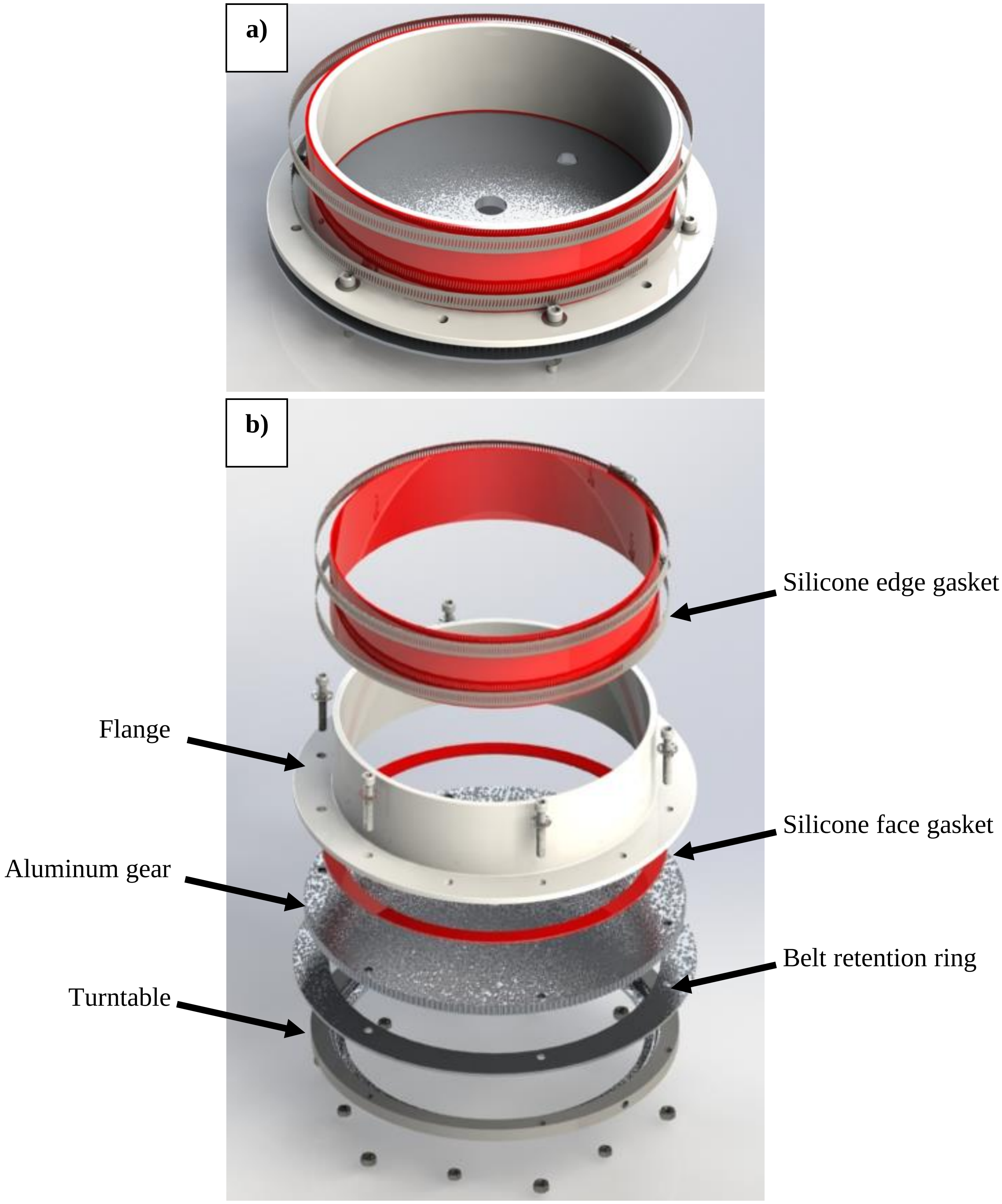

Figure 3.5. a) Assembled concentrator base; and **b)** exploded view of concentrator base with labels.

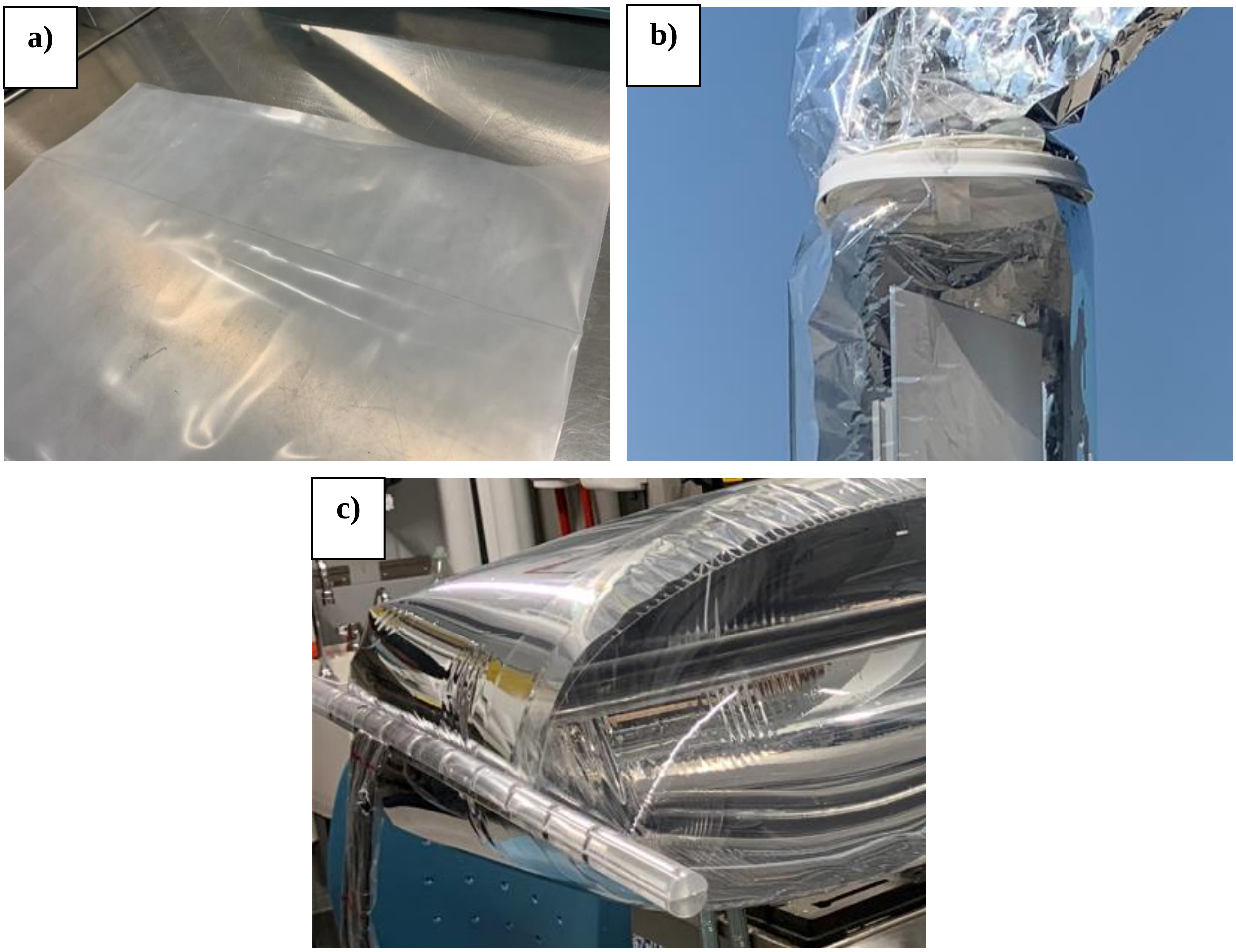

Figure 3.6. Various methods used to seal the top of the bag. **a)** Seal formed by using an impulse welder; **b)** seal formed by a friction fit between a screw-on pail lid and retaining ring; and **c)** seal formed by sandwiching the top of the film between two half rounds.

3.2. Concentrator base subassemblies

The concentrator base is a point of heavy machinery within the system. It must consist of subassemblies that enable rotation of the concentrator, adjust and monitor inflation of the bag and receiver, and include equipment for monitoring thermal performance. This section will describe the mechanical subassemblies of the concentrator base and base frame. The inflation and thermal set-up will be described in a later section.

The concentrator base serves two primary functions: enabling rotation of the concentrator and providing access-ways for inflation. Both of these functions are accomplished through the use of a custom-made aluminum gear. A 3/8" thick aluminum sheet was waterjet cut into a gear assuming interface with an XL series timing belt using the specification provided by MISUMI. The gear is then placed underneath the flange (separated by a silicone ring gasket). A custom-made belt retention ring was also waterjet cut to match the diameter of the flange and placed underneath the gear to constrain the timing belt. Finally, an aluminum turntable was placed underneath the belt retention ring to allow for rotation. The bolt holes of all components were matched to the aluminum turntable and screwed together. The concentrator base subassembly is shown in **Figure 3.5**. The base connects to the inner race of the turntable to allow for rotation, while threaded rods are screwed into the outer race and connected to the base frame. Several holes were drilled into the gear to allow for fittings to be used in inflation.

The concentrator base frame is much more simplistic. The base frame provides for enough clearance from the ground to make room for the inflation components which will be described shortly. Additionally, the base frame features levelling feet to ensure that the concentrator remains straight during tests. All pressure control components were tied into the base frame. The concentrator base frame subassembly is shown in **Figure 3.7**.

3.3. Inflation

The mechanisms by which the concentrator inflates evolved over several prototypes. In the earliest prototypes where the receiver had not yet been constructed, the bag had been inflated through a pressure regulated line connecting to a push to connect valve. In this section, the final inflation design (with receiver) will be discussed as it is shows the complete picture of the inflation mechanisms.

3.3.1. Inflation and pressure regulation

For all experiments, the concentrator was inflated through a single line connected to the air supply in the Bergeron Centre of Engineering Excellence. However, the delivery pressure from this line was too high to be used directly. The pressure regulation system as shown in **Figure 3.8** was used to simultaneously drop the pressure of the air and divert it to several locations throughout the

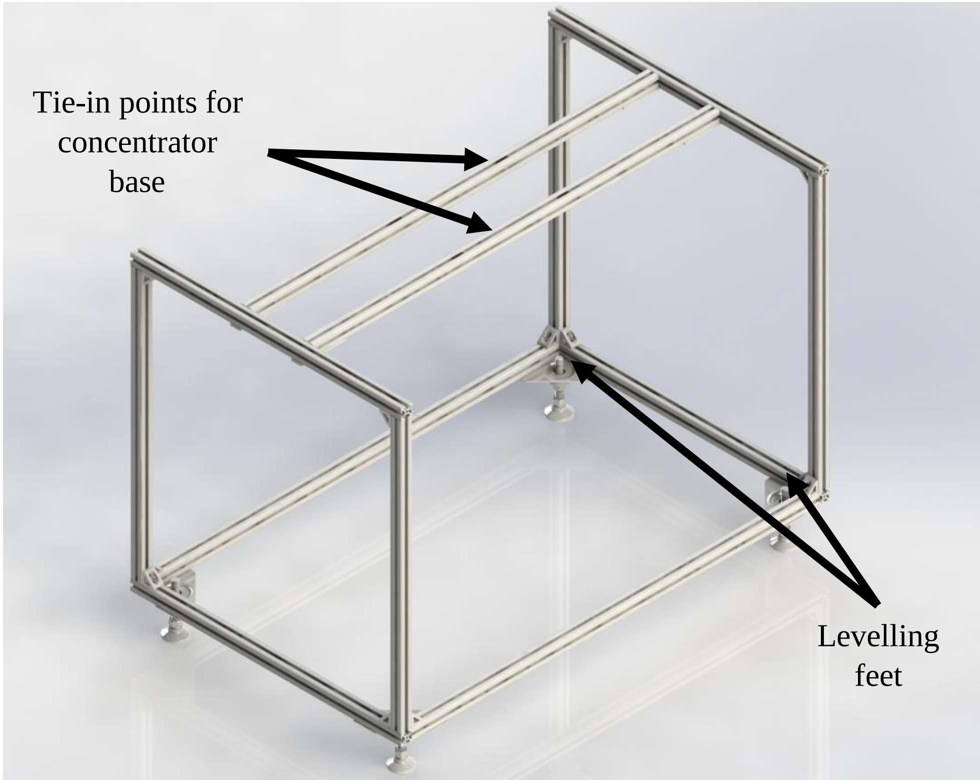

Figure 3.7. Concentrator base frame with labels

system. First, air is brought through a Wilkerson relieving air regulator with built in gauge rated for 0-125 psi to drop the pressure to around 20-30 psi. The air leaves the regulator and enters into a 1/4" PTC wye where the pathways for the receiver and central chamber are split. One path of the wye leads to a Control Air Type 800 subminiature precision regulator rated for 0-5 psi to provide a leak pressure for the stagnant air in the bag. The outlet of the regulator leads into a 1/4" PTC tee, with one end terminating in a pressure gauge to read the delivery pressure. The second end leads to a 360° swivel PTC fitting connected to a Yor-Lok bulkhead fitting connected through the wall of the aluminum gear which ultimately inflates the bag. A second bulkhead fitting is connected through the wall of the gear and connects to an external pressure gauge reading the internal bag pressure. The second pathway diverting from the 1/4" PTC wye enters into a second 1/4" PTC tee with one end connecting to an adjustable knob rotameter rated for 0.8 – 8.2 scfm and the other connected to a gauge for reading the receiver delivery pressure. The exit from the rotameter enters the receiver sub-assembly where the flow rate can be adjusted.

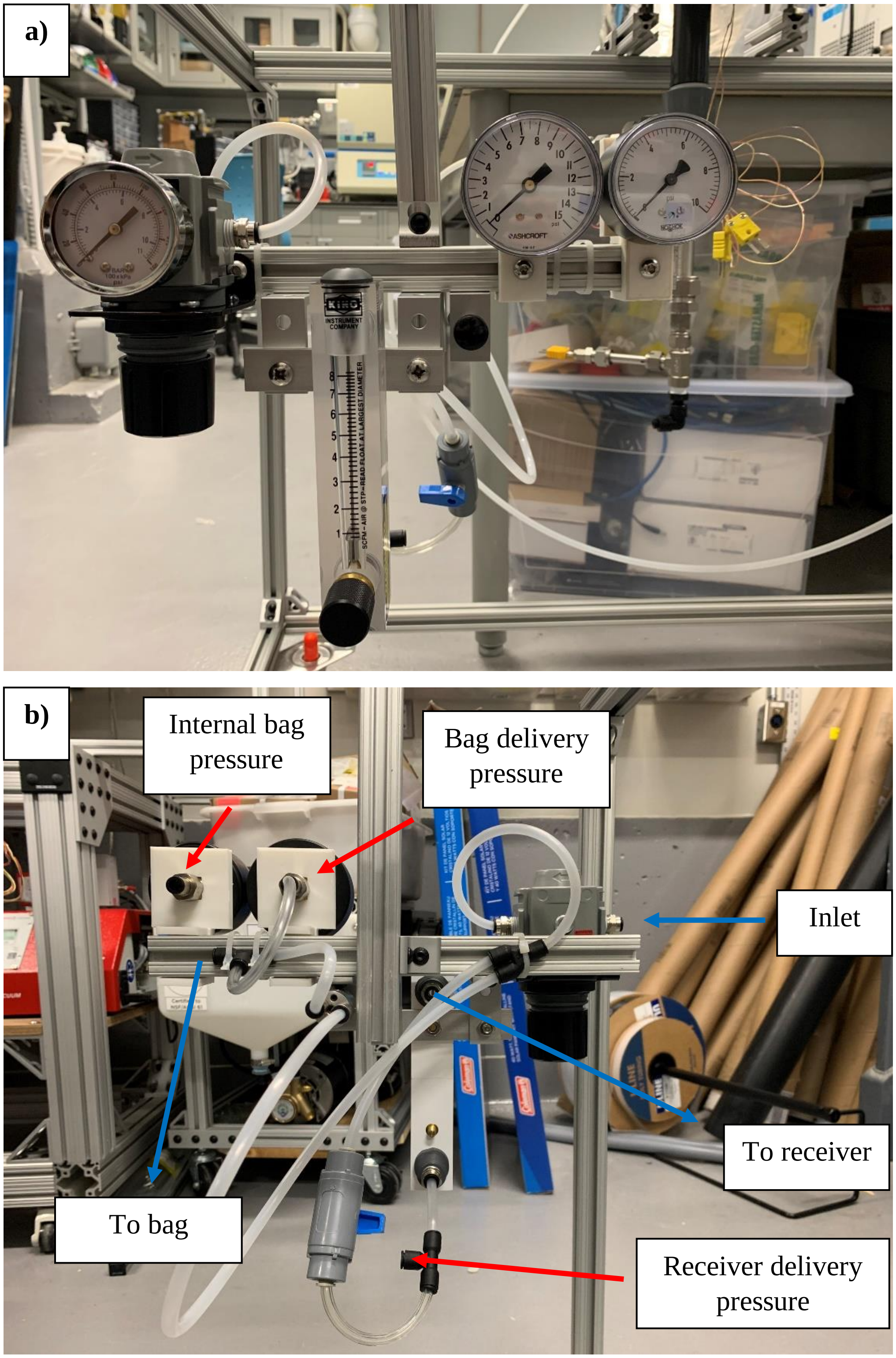

Figure 3.8. a) Front face of inflation sub-assembly; and **b)** back face of inflation sub-assembly with blue arrows representing flows and red arrows representing pressure readings. The gauge for reading the delivery pressure of the receiver is not connected in this image.

3.3.2. Receiver design – flow path

While the vertical solar concentrator is, by itself, a novel concept, the fully flexible and inflated receiver further justifies the low-cost design and opens the possibility of controlled deployment. The vertical concentrator, however, complicates the inflation and thermal extraction processes. In the horizontal configuration, the heat transfer fluid may enter from one side and be extracted from the other after it is heated. In the vertical configuration, the air must flow upwards. However, having a thermal extraction point at the top of the concentrator both complicates deployment and adds unnecessary weight to the self-supported structure. Therefore, a novel annular receiver is proposed where the air must first flow upwards through the internal tube to bring it to the top, and subsequently flows downwards through the outer top where it is heated and flows towards the exit. This allows for both the inlet and outlet to be fixed within the base of the concentrator.

3.3.3. Receiver inflation sub-assembly

Since the dummy tube and receiver are concentric, so too must be the inlet and outlet of the inflation sub-assembly. Unlike the main inflation system, however, the receiver inflation sub-assembly is complicated, and will be described directly through a labelled schematic in **Figure 3.9**. **Figure 3.10** displays a cross-section of the sub-assembly and displays the flow paths and thermocouple connection points.

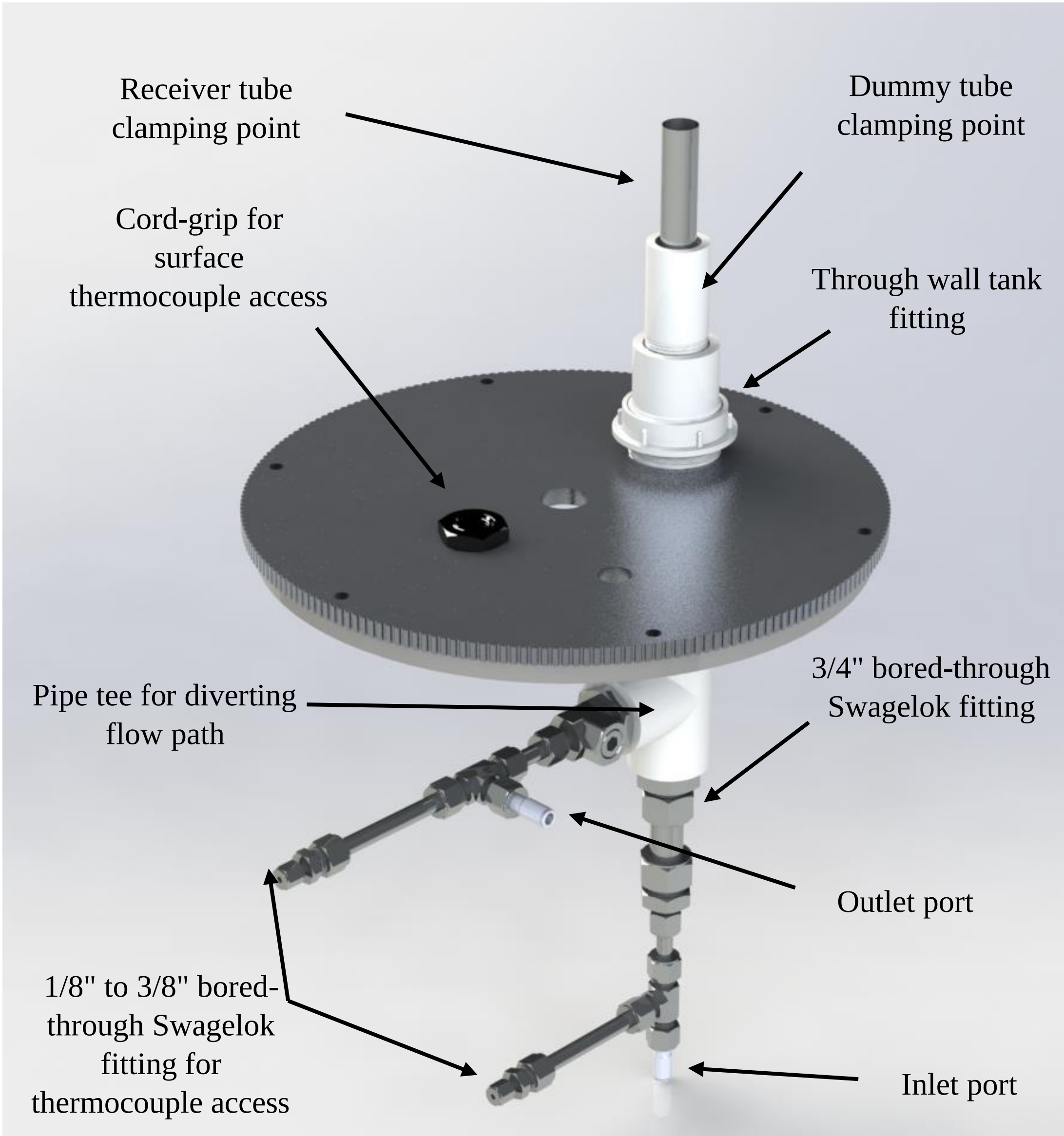

Figure 3.9. Isometric view of the receiver inflation sub-assembly with labelled components. The non-labelled components are an assortment of 3/8″ tubing and 3/8″ Yor-Lok fittings.

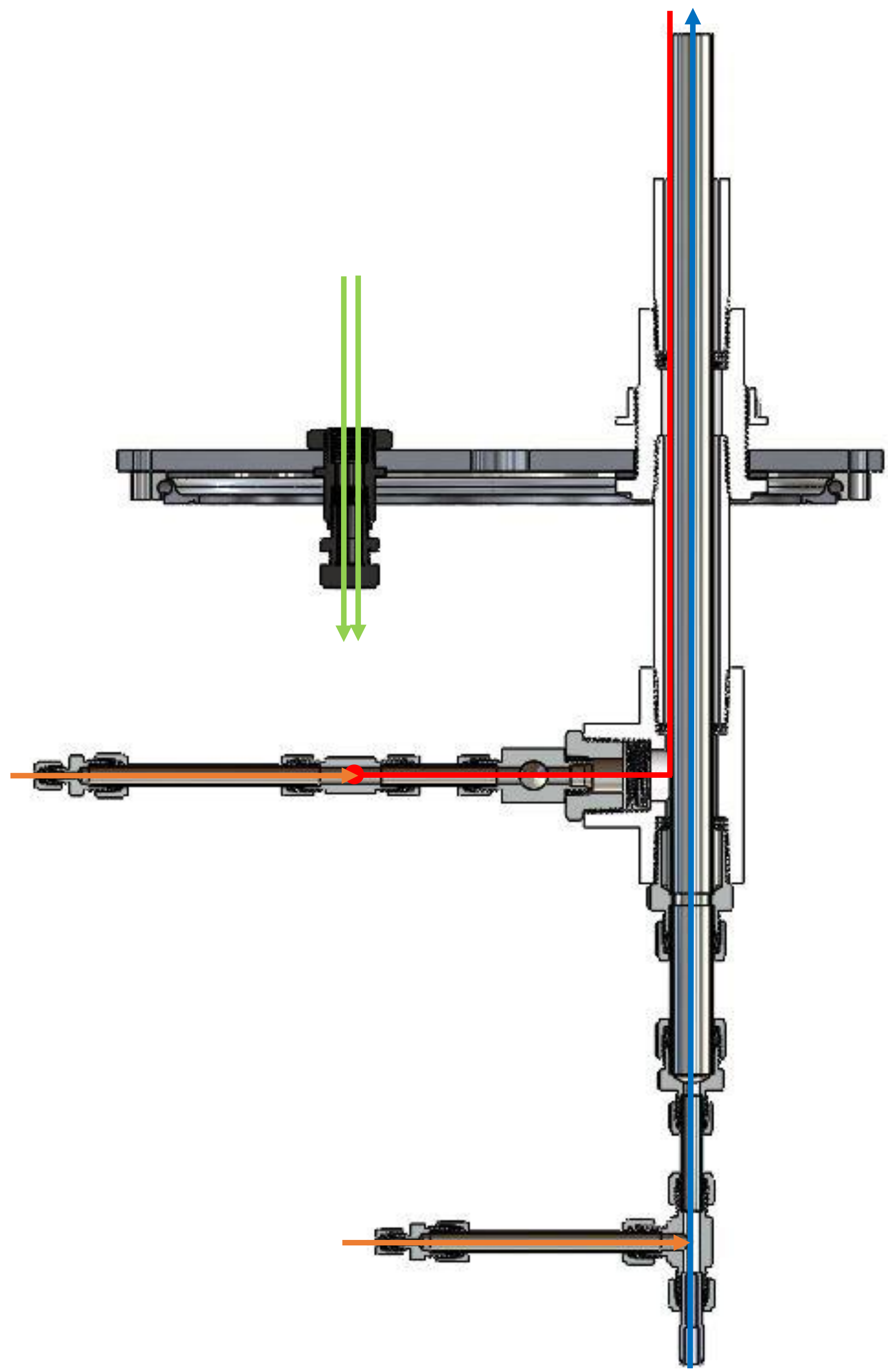

Figure 3.10. Cross-sectional view of the receiver inflation subassembly. The blue and red arrows represent the inlet and outlet flow respectively. The red dot that terminates the outlet flow represents flow out of the page. The orange arrows represent the thermocouples that read the inlet and outlet temperature. The green arrows represent the thermocouples that read the surface temperature of the receiver.

The 3/4" bored-through Swagelok fitting as shown in **Figure 3.9** is the most important component in the sub-assembly. By screwing this fitting into a pipe tee, it effectively separates the hot and cold fluid streams. The cold stream passes through the 3/4" tube through the bored-through connection, and the hot stream exits the pipe tee at a right angle without mixing. The bored-through 3/8" to 1/8" Swagelok compression-fit adapter is equally as important. This compression fitting allows for a thermocouple to pass through and read the inlet/outlet temperature while simultaneously preventing leaks though the use of a nut and ferrule. The 4" of tubing that separates the two fittings is to maximize the conduction resistance between the thermocouple tip and the wall of the fitting. This is to ensure that the thermocouple is reading the temperature of the oncoming flow and not the temperature of the fitting wall. **Figure 3.11** shows the thermocouple subassembly and how it aims to maximize conduction resistance and **Figure 3.12** shows the inlet and outlet thermocouples embedded within the inflation sub-assembly.

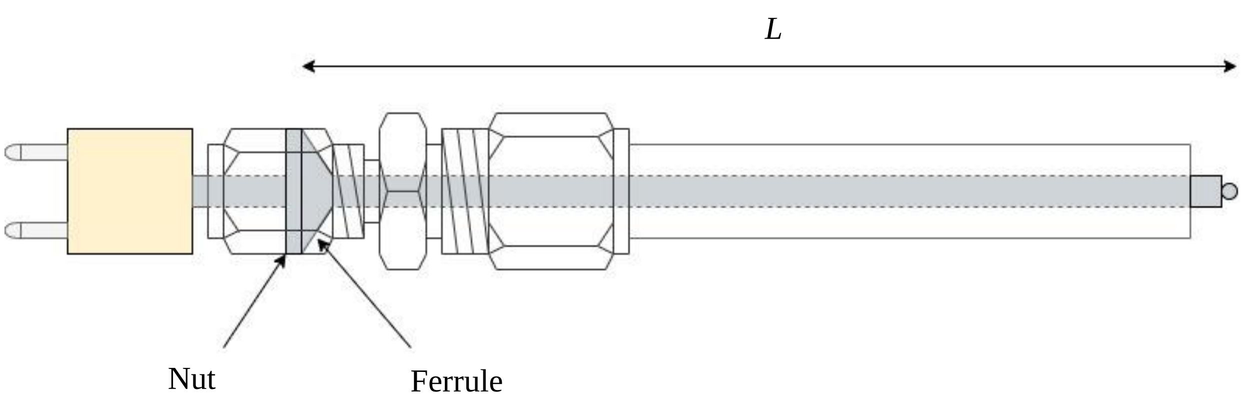

Figure 3.11. Thermocouple fed through a Swagelok bored-through fitting with connection point separated from the tip by distance *L* to maximize conductive resistance.

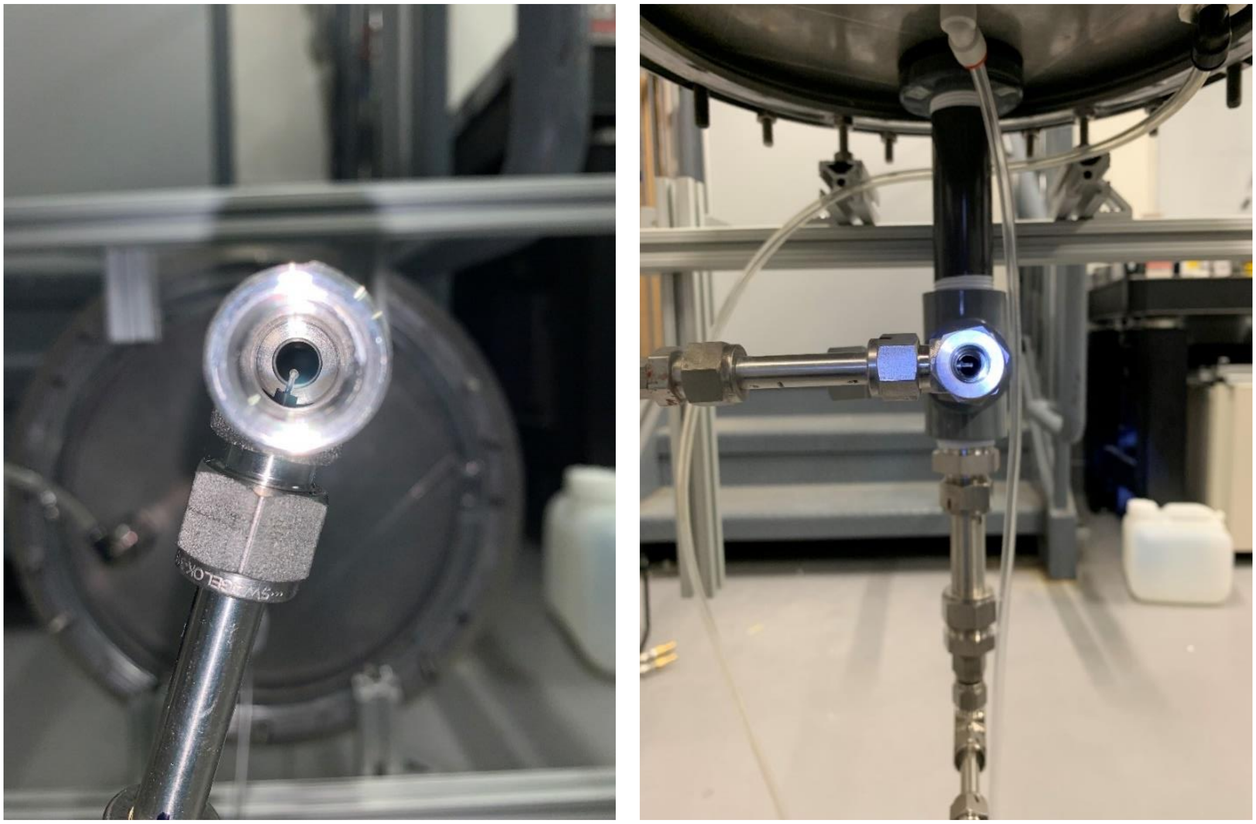

Figure 3.12. Inlet and outlet thermocouples secured in a cross-flow configuration with the heat transfer fluid within the inflation sub-assembly.

3.4. Concentric receiver material

The choice of material for the thermal receiver is critical in determining the performance of the collector. Consider the absorbing qualities of the receiver. Radiation from the sun is emitted at a nominal temperature of 5780 K. Then, according to Wien's displacement law, the peak wavelength being emitted is around 0.5 μm. That is, the majority of sunlight incident upon the receiver will be in the visible range. Conversely, the receiver will also thermally emit at its operating temperature. Consider a receiver that operates in the range of 50°C - 100°C. The peak wavelength for emission will be 8.97 μm and 7.77 μm, respectively. Therefore, the receiver will preferentially emit radiation from within the infrared spectrum. In the ideal case, the receiver will be made of a material with high absorption within the visible spectrum to maximally absorb incident radiation and a low emission within the infrared spectrum to mitigate radiative losses. This is also known as a high absorption to emission ratio or high solar selectivity. In the horizontal configuration, this is typically done by applying a solar selective coating over the surface of a rigid member[12]. These coatings, however, do not adhere well to flexible polymers and therefore cannot be coated on the surface of an inflated receiver. Therefore, several flexible polymers were analyzed for inherent solar selectivity. To do so, the spectral hemispherical transmittance and the spectral hemispherical reflectance over the visible and infrared wavelengths were measured using the Shimadzu UV-2600 spectrophotometer (UV-vis) and the Vertex 70 FTIR by Bruker, respectively. The total wavelength spectrum measured 220 – 28600 nm. Absorptance was calculated using $\alpha_\lambda = 1 - \rho_\lambda - \tau_\lambda$. Solar selectivity is then obtained by spectrally integrating the absorptance data over the wavelength range. The formal integral for doing so is as follows

$$\alpha = \frac{\int_0^\infty \alpha_\lambda E_{b\lambda} d\lambda}{\int_0^\infty E_{b\lambda} d\lambda} = \frac{\int_0^\infty \alpha_\lambda E_{b\lambda} d\lambda}{\sigma T_{\mathrm{sun}}^4} \tag{3.20}$$

$$\varepsilon = \frac{\int_0^\infty \varepsilon_\lambda E_{b\lambda} d\lambda}{\int_0^\infty E_{b\lambda} d\lambda} = \frac{\int_0^\infty \alpha_\lambda E_{b\lambda} d\lambda}{\sigma T_o^4} \tag{3.21}$$

where $E_{b\lambda}$ is the blackbody spectral emissive power at either T_{sun} (temperature of the sun) or T_{o} (operating temperature of the polymer). However, the spectrum measured by the UV-vis and FTIR are finite, and therefore the experimental values of total emittance and total absorptance will differ from the true value. The experimental values of total emittance and absorptance are calculated using

$$\alpha_{\mathrm{exp}} = \frac{\int_{\lambda_1}^{\lambda_2} \alpha_\lambda E_{b\lambda} d\lambda}{\int_{\lambda_1}^{\lambda_2} E_{b\lambda} d\lambda} \tag{3.22}$$

$$\varepsilon_{\mathrm{exp}} = \frac{\int_{\lambda_1}^{\lambda_2} \varepsilon_\lambda E_{b\lambda} d\lambda}{\int_{\lambda_1}^{\lambda_2} E_{b\lambda} d\lambda} \tag{3.23}$$

The error induced by using Eqs. (3.22) and (3.23) will be provided in the next section. **Table 3.1** provides the total spectral absorptance and emittance along with the solar selectivity for several thin film polymers.

Table 3.1. Total spectral data and selectivity for various polymers.

Polymer	**Total absorptance at T_{sun} = 5780 K**	**Total emittance at T_o = 373 K**	**Solar selectivity**
Butyl rubber[a,b]	0.9495	0.9052	1.0489
Kapton	0.9229	0.8783	1.0507
Black polyethylene	0.9439	0.8067	1.1700
EDPM rubber	0.8910	0.8630	1.0324
High temperature silicone	0.8949	0.9349	0.9572
Buna-N foam	0.9687	0.9478	1.0220
Oil resistant buna-N foam	0.9410	0.8921	1.0549
Oil resistant, high strength buna-N foam	0.9399	0.8935	1.0520
Viton	0.9267	0.8987	1.0311

[a]The NIR wavelength range (220 – 2000 nm) was not measured for all polymers except butyl rubber. Instead, this wavelength range was interpolated over.

[b]Measurements for butyl rubber were taken at a much higher resolution once it was chosen as the receiver material.

Unfortunately, all materials displayed a weak inherent solar selectivity. While butyl rubber does not display a very large value of solar selectivity, it is still the best option for several reasons: it has a comparatively large value of solar selectivity out of all thin films tested, it comes readily available in cylinders in the form of bicycle inner tubes, and it has a high melting point. The last point became quickly apparent as black polyethylene (the initial choice for receiver material) quickly melted in on sun tests. The final spectral data for butyl rubber is provided in **Figure 3.13**

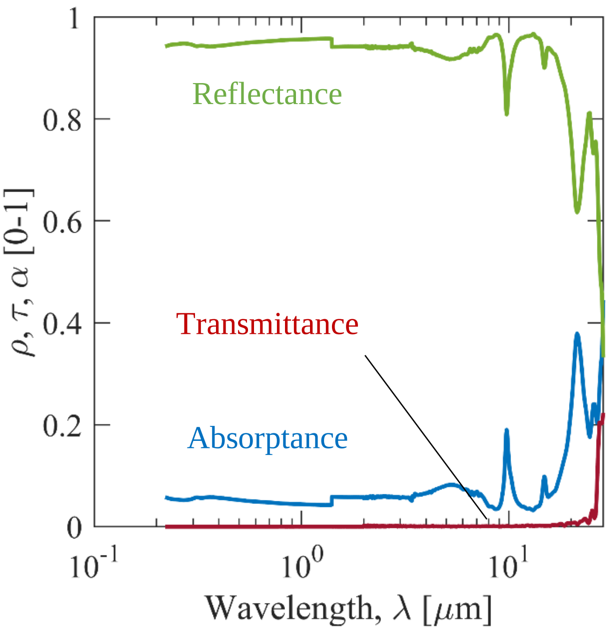

Figure 3.13. Spectral hemispherical data for butyl rubber analyzed using a Shimadzu UV-2600 spectrophotometer for the visible wavelength range and the Tensor 27 FTIR for the near- and mid-infrared wavelength range.

3.5. Error in total absorptance/emittance integration

While the calculated values of total emittance and absorptance are as accurate as they can be with the current measurement techniques, there still exists an induced error by integrating over a subset of the wavelength range. Interestingly, performing the integration in this way is equivalent to assuming that the spectral hemispherical absorptance and spectral hemispherical emittance from 0 to λ_1 and from λ_2 to ∞ is equal to the total (or average) absorptance and emittance. The derivation that proves this is shown in *Appendix B*. Nevertheless, an estimation of this error can be calculated by comparing the denominator of the integrals in Eq. (3.20) and (3.22) and Eq. (3.21) and (3.23) [12]. Fortunately, the majority of the $E_{b\lambda}$ distribution evaluated at T_{sun} falls within the region we can measure as shown in **Figure 3.14**. Thus, integrating over a subset of the wavelength range yields

[12] The exact error cannot be known as it would require knowledge of the value of ε_λ and α_λ outside the measured wavelength range.

a total absorptance that is approximately 0.5% lower than when integrated from 0 to ∞. However, the opposite is true for the total emittance. Consider the total emittance at an operating temperature equal to 100°C as shown in **Figure 3.14**. Since a significant portion of the wavelength range falls outside that which can be measured, there will be a larger induced error. **Figure 3.15** provides the approximate values of total emittance and their associated errors for a range of operating temperatures.

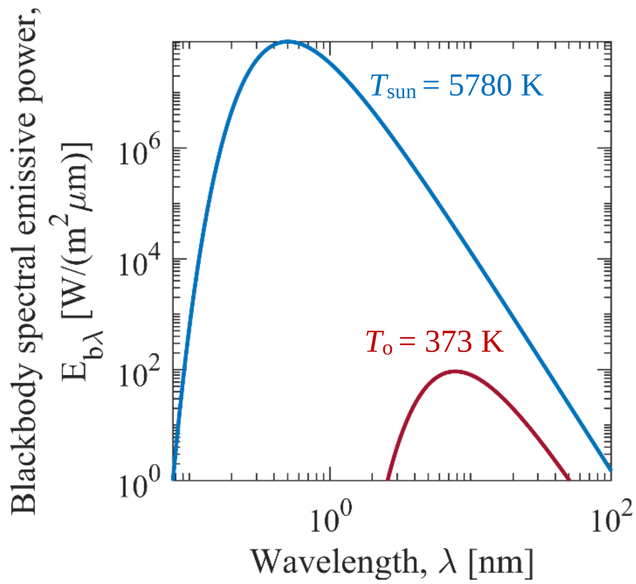

Figure 3.14. Distribution of the blackbody spectral emissive power at T_{sun} = 5780K and at a characteristic operating temperature T_o = 373K.

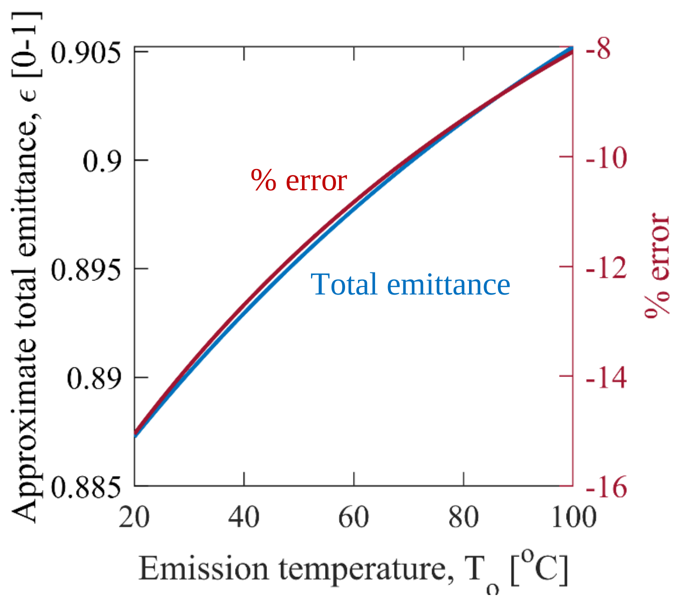

Figure 3.15. Dependence of the approximate total emittance of butyl rubber on operating temperature and the associated error when integrating $E_{b\lambda}$ over a subset of the entire wavelength range.

3.6. Concentric receiver design

Finally, the concentric receiver tube was constructed using two 6.5′ bicycle inner tubes made of butyl rubber. The dummy tube, measuring 3/4" in diameter, was placed inside the active receiver tube 1.315" in diameter. A 5/16" hole was punched through the top of the dummy tube to bleed air into the receiver after reaching the top. The receiver tube was also fit with two thermocouples used to measure the surface temperature at its midspan. One thermocouple was fastened on the side of the receiver closest to the mirror while the second was fastened on the side closest to the transparent sheet. A thin butyl rubber ring was then placed over top the two thermocouples. Once the receiver was mounted, it was stretched through the bag to a final length of 9′. The inflated thermal receiver and surface thermocouples are shown in **Figure 3.16**.

3.7. Final values of concentration

In addition to being thermally stable at higher temperatures, the bicycle inner tube was chosen as its size aligned well with the target regime of low-concentration. With a projected inlet aperture width equal to 11.27" and a receiver diameter equal to 1.315", the resulting geometric concentration is equal to 2.73. However, because we extended the rim to comprise half the outer-envelope for ease of construction and cost-consideration, the flux concentration will not be equal to the geometric concentration. For the present case, we will consider that the optical efficiency is equal to the intercept factor. Simulating the system results in an intercept factor equal to 0.7823. Then, the final value of flux concentration is equal to 2.13.

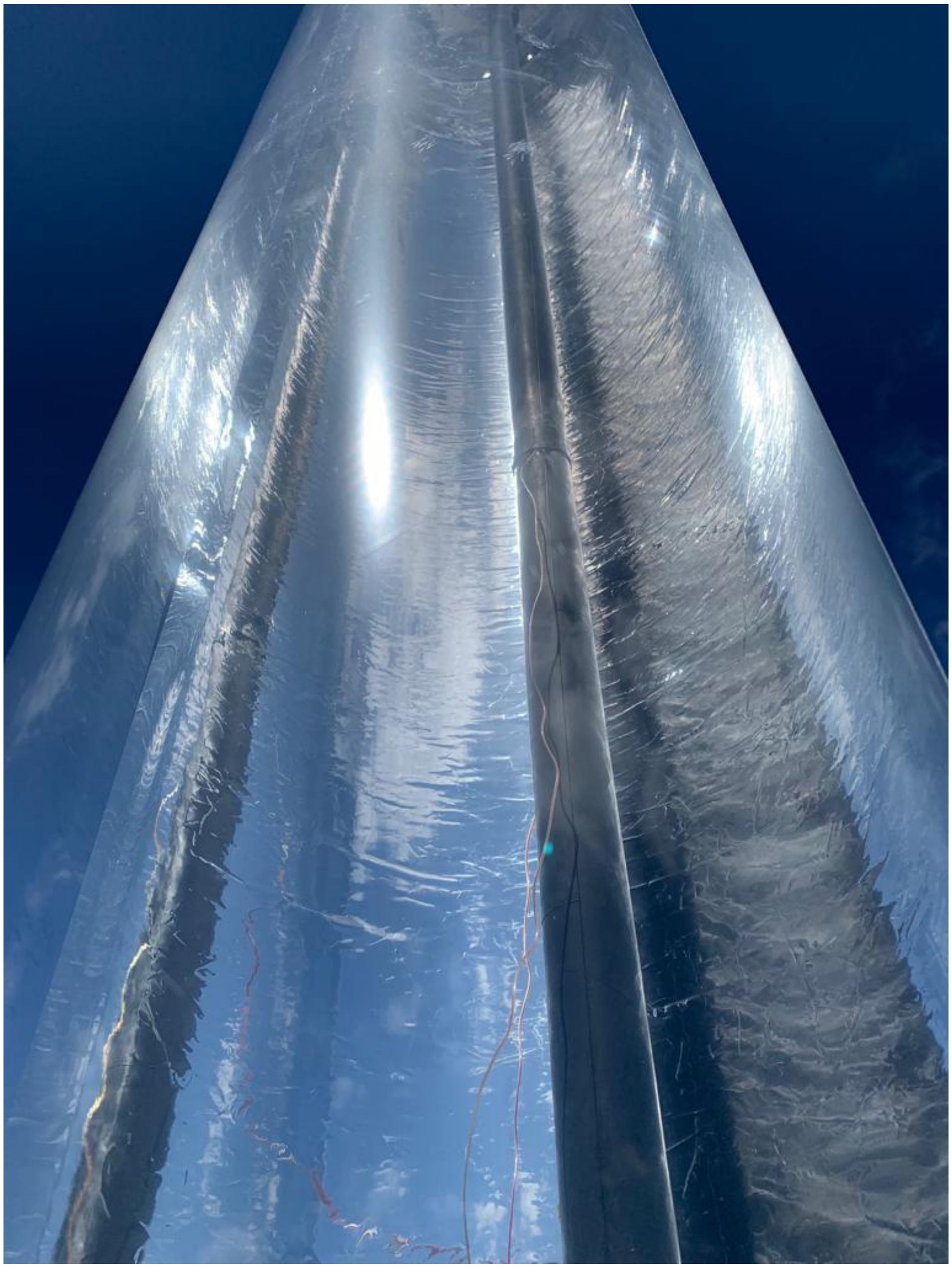

Figure 3.16. Inflated thermal receiver made of butyl rubber. Two thermocouples are fastened at the midspan of the receiver to measure the surface temperature.

3.8. Final prototype

The final prototype developed in this work is summarized in **Table 3.2** for quick reference throughout this text with the main dimensions shown schematically in **Figure 3.17**.

Table 3.2. Design parameters for the final prototype

Outer envelope	Diameter, D [m (in.)]	0.286 (11.27)
	Height, H [m (ft.)]	2.74 (9)
	Mirror rim angle, φ_{rim} [°]	180
	Projected width, $W_{\mathrm{proj.}}$ [m (in.)]	0.286 (11.27)
	Mirror material	Metallized polyester (BoPET)
	Transparent top-sheet material	Polyester (BoPET)
Receiver	Diameter, D [m (in.)]	0.0334 (1.315)
	Circumference, C [m (in.)]	0.105 (4.13)
	Distance from origin, k [m (in.)]	0.098 (3.85)
	Height, H [m (in.)]	2.74 (9)
	Material	Butyl rubber
Optical performance	Geometric concentration, C_g	2.73
	Intercept factor, γ	0.7823
	Flux concentration, C_{flux}	2.13

3.9. Cost consideration of final prototype

To afford comparison to other CSP technology, a surface level cost per m^2 will be determined for the prototype at commercial scale. For this analysis, only the polymers will be considered as the framing was developed for prototyping purposes and is subject to change. Furthermore, the prices are taken directly from the manufacturer at the time of procurement. Therefore, the prices of the metallized polyester, clear polyester, and butyl rubber are given as \$4.19/m^2, \$4.5/m^2, and \$18.24/m^2, respectively. Therefore, the total cost for the collector is approximately \$45.17/m^2 (accounting for both the receiver and the dummy tube). This estimate, however, will change once the material cost is reduced at scale.

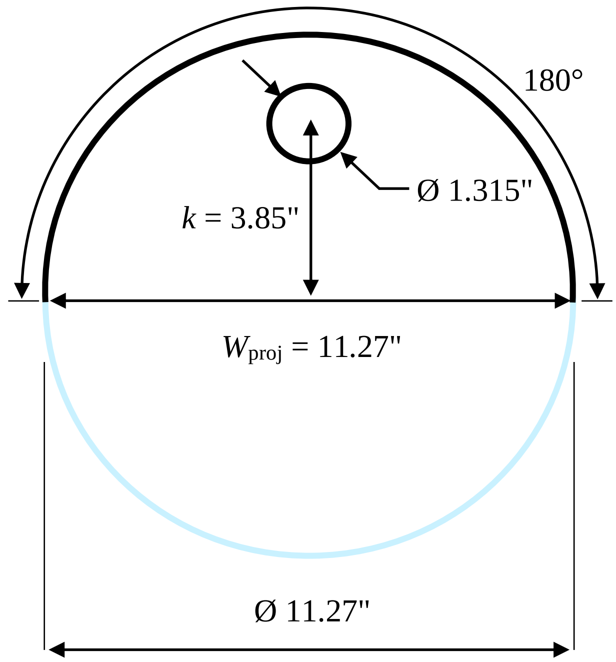

Figure 3.17. Cross-sectional schematic of the final prototype with dimensions.

3.10. Furling

While the vertically oriented solar concentrator was designed to operate under the widest range of environmental conditions, it must not be exposed to particularly strong winds that could permanently yield the material. It is for this reason that the concentrator must be capable of deployment and stowing at any given time.

The logistics of stowing the concentrator is simple; the valve controlling the flow to the inlet is to be shut off. However, there is concern over what happens to the bag is stowed. For example, as the internal pressure is released, the mirror membrane may wrinkle reducing optical performance (*see section 6.1*) or tear due to friction with nearby objects rendering the concentrator functionally useless. Letting the bag free-fall was the chosen method during experimentation, however, it cannot be concluded whether this is problematic as the bag was always stored after stowing.

It is for these reasons that the idea of furling was introduced. Furling is the concept whereby the bag would roll-up as the pressure is released to minimize risk. The idea of furling was tested in early prototypes with a bag made entirely of polyethylene film. Constant-force springs, or tape springs, were considered as the primary choice to accomplish furling. Manufactured in coils, a tape spring is elastic along its lengthwise direction; upon being pulled, a restoring force acts to retract the tape spring into its natural curvature. Tape springs are widely used in tape measurers

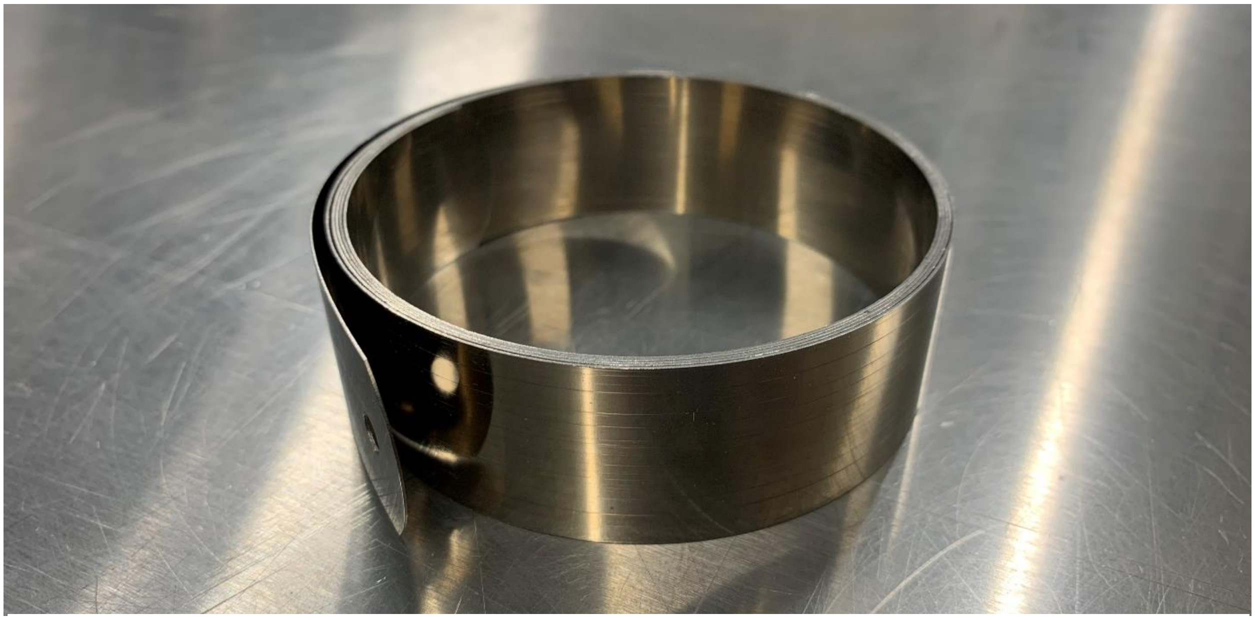

Figure 3.18. Tape spring in its naturally coiled state.

and shelving pushers to keep product at the front of a shelf as it is gradually removed. As the name suggests, the constant force spring experiences a constant load-deflection relationship after pulled 1.25 times its diameter. **Figure 3.18** shows a tape spring in its naturally coiled state.

Utilizing the tape spring requires a specific concentrator configuration. The top seal of the concentrator must be impulse welded to form a permanent connection. Extra fabric at the top (past the seal) is then then formed into a cylinder and fastened to the bag as shown in **Figure 3.19 a)**. This allows for a furling tube to be placed inside the pocket and will guide the bag as it rolls. The tape spring is then implemented by first fastening one end to the base of the concentrator (under the hose clamp around the flange in the present case), while the opposite end is brought through an incision in the fabric where it wraps around the furling tube. According to specification, the furling tube was 10-20% larger than the natural diameter of the coil and a minimum of 1.5 wraps was left on the spool at all times. Upon deflation, the tape spring retracts, coiling around the furling tube and furling the bag along with it. In contrast, when the bag is inflated, the pressure forces the tape spring to uncoil until it is fully elongated. A successfully furled and unfurled concentrator is shown in **Figure 3.19 b)** and **c)**.

Unfortunately, the tape springs faced major issues and a successful coil was not repeatable. At full elongation, the tape springs tended to buckle as they retracted, in addition to sliding laterally along the concentrator spine as shown in **Figure 3.20**. Most importantly, the tape spring tended to lift off the spine where the coil meets the furling tube, just before the incision. This produced erratic results, and the bag did not coil cleanly nor repeatedly across tests. It can be said, however, that many of the problems faced here may be eliminated by physically fastening the tape spring against the spine of the concentrator.

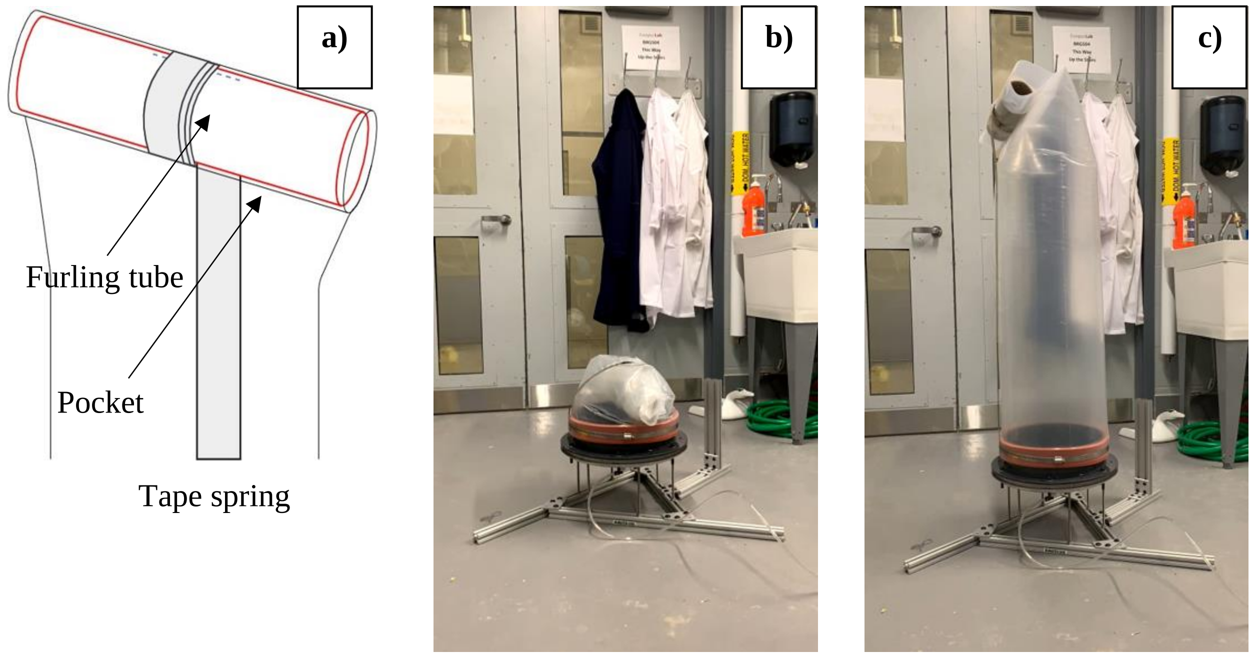

Figure 3.19. a) Tape spring configuration where the furling tube (red) is embedded within a cylindrical pocket and the tape spring (grey) is wrapped around the furling tube before exiting through an incision (blue dashed line) and travelling down the spine of the concentrator; **b)** concentrator in the furled state; and **c)** concentrator in the unfurled state.

Another approach for furling was using a pulley and winch. To utilize this method of furling, the top seal of the concentrator must use the half round method. Two pulleys were fastened onto the end of the half-rounds and fishing line roughly equal to the length of the concentrator was wrapped around each as shown in **Figure 3.21**. The fishing line was then coiled onto two winches fastened into the rotatable base. Some success was found with this method, however, it too faced challenges. It proved to be problematic if the speed at which the winches were rotated did not match the deflation speed of the bag; coiling too fast resulted in over-tensioning the bag while coiling too slow caused the line to spill off the pulley. Additionally, this method requires the concentrator to be manually stowed and deployed. Ultimately, this method of furling was not thoroughly tested and was removed in later prototypes.

Figure 3.20. A buckled tape spring that has slid laterally causing the bag to furl in an uncontrolled direction. This tape spring was confined within a second pocket along the spine of the concentrator but was not physically constrained due to loose tolerances.

Figure 3.21. Furling method by winch and pulley as shown on a 10′ concentrator.

3.11. Tracking

In order to achieve tracking, the collector was designed to fit on a turntable. The inner race of the turntable would provide structural support by connecting to the collector base frame while the outer race would enable tracking. The waterjet cut gear was initially going to interface with an XL series timing belt connected to a closed loop stepper motor. The motor was chosen such that the step size was significantly smaller than the angular size of the sun allowing for perfect tracking of the solar disk. The implementation of the tracking mechanism, however, was foregone to prioritize the thermal analysis. Instead, the tracking was performed manually in the thermal experiments with the use of a "shadow stick" as shown in **Figure 3.22**. The shadow stick is an aluminum tube positioned in the centre of the base of the collector such that it would project a shadow when the collector was rotated into view of the sun. When the shadow was cast directly in the centre of the receiver, the collector was considered to be appropriately tracking the sun. Because this method was rudimentary in nature, the collector was designed to have a large acceptance angle of 1° such that a visual technique would provide accurate results.

Figure 3.22. Aluminum tube (shadow stick) projecting a shadow onto the receiver indicating the collector is tracked.

Chapter 4

Optical modelling

In Chapter 3, the mechanics of an inflated beam made of thin-film membranes was discussed at length. The functional relationship between the aspect ratio and moment and deflection was determined, thus providing a guideline for constructing structurally viable concentrators. These conditions alone, however, are not sufficient in producing an optimal concentrator, as it lacks sufficient optical and thermal analysis. In this chapter, the solar concentrator will be analyzed from an optical perspective using various simulation techniques.

4.1. Quasi-analytical Monte Carlo ray tracing

The fundamental function of the solar concentrator is the ability to reflect thermal radiation in a deterministic manner. Parabolic surfaces have been known to focus incoming radiation to a perfect line, while circular surfaces result in spilled radiation [7]. While previous research has aimed to quantify the effect of imperfectly matching the parabola, lengthwise curvature has not been considered given the focus on structural stability. However, the deflection experienced by vertical concentrators can significantly impact the operating efficiency of these devices by skewing reflected radiation. To date, no Monte Carlo ray tracing software is capable of producing an analytical, or semi-analytical, solution for free form surfaces. To that end, it was necessary to develop a quasi-analytical Monte Carlo ray tracing algorithm (Qa-MCRT) in Matlab for the purposes of reflecting surfaces that deflect according to Euler-Bernoulli beam theory.

4.1.1. Ray and surface parameterization

The starting points of each ray are generated on an inlet aperture that spans from one corner of the mirror to the opposite corner. The inlet aperture is defined at an offset specified by the user. The starting coordinates of each ray are then given by

$$x_e = L\left(\mathbb{R} - 0.5\right) \pm \left(\frac{L}{2} - R\sin\left(\frac{\varphi_{\mathrm{rim}}}{2}\right)\right) \tag{4.1}$$

$$y_e = \text{offset} \tag{4.2}$$

$$z_e = H\mathbb{R} \tag{4.3}$$

where L is the length of the receiver, $\mathbb{R}$ is a random number from 0 to 1, R is the radius of the outer-envelope, φ_{rim} is the rim angle, and H is the height of the bag. The second term in Eq. (4.1) ensures that the rays are always being generated on the inlet aperture, since its centreline is not always coplanar with the x-z plane in global coordinate system (GCS). Each ray is then assigned a direction vector that is generated within a cone subtended by an angle of 0.266° (corresponding to the angular size of the sun). In the GCS, the equation of the ray is described by

$$\vec{\mathbf{r}} = \begin{bmatrix} x_e \\ y_e \\ z_e \end{bmatrix} + D \begin{bmatrix} s_x \\ s_y \\ s_z \end{bmatrix} \tag{4.4}$$

Since the inflated concentrator deflects according to Euler-Bernoulli beam theory according to the discussion provided in *Section 3.1*, the relevant assumptions and equations can be applied to form the parameterization of the mirror surface. One of the critical assumptions regarding Euler-Bernoulli beam theory is that the cross-section remains unchanged after deflection occurs. Thus, the surface parameterization of the mirror is the parameterization of a cylinder plus the deflection at the infinitesimal cross section

$$\vec{\mathbf{s}} = \begin{bmatrix} r\cos\theta + \cos(\theta_w)\delta(z) \\ r\sin\theta + \sin(\theta_w)\delta(z) \\ z \end{bmatrix} \tag{4.5}$$

where θ_w is the direction of the wind and $\delta(z)$ is taken from Eq. (3.10), reiterated here for convenience

$$\delta(z) = f\,\frac{\omega x^2}{24EI}\left(x^2 + 6l^2 - 4lx\right) \tag{4.6}$$

Depending on the construction of the concentrator, the receiver may experience the same, partial, or none of the deflection experienced by the outer-envelope. For this reason, Eq. (4.6) is multiplied by a factor of f which ranges from 0 to 1. Typically, the value of f will be set to 0 which indicates that the receiver is not physically constrained within the bag, that is, the bag is shielding the receiver from experiencing any deflection. **Figure 4.1** shows a general configuration with an arbitrary rim angle for visual purposes.

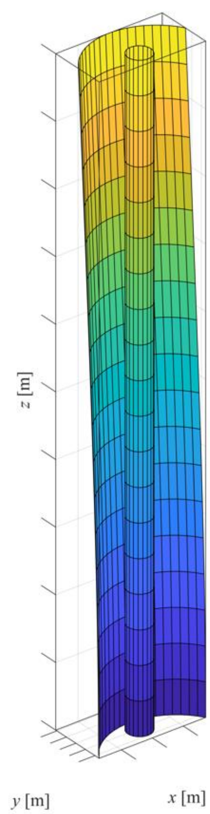

Figure 4.1. General configuration of a solar collector with $f = 0$ experiencing an arbitrary force.

4.1.2. Intersection calculation

Eq. (4.5) is a multi-variable parameterization; it uses the circumferential parameter θ and the height parameter z. Therefore, the intersection calculation must be performed numerically. First, the mirror and receiver are segmented into cross-sections of infinitesimal thickness. Then, applying Euler-Bernoulli beam theory, each cross section is a circle (for the receiver), or sector of a circle (for the mirror) displaced by an amount given by Eq. (4.6). Each cross-section then has a centre point given by

$$\mathbf{C} = \begin{bmatrix} \delta(z)\cos(\theta_w) \\ \delta(z)\sin(\theta_w) \\ l \end{bmatrix} \tag{4.7}$$

where the x- and z-components of Eq. (4.7) are modified by a factor of $\cos(\theta_w)$ and $\sin(\theta_w)$ corresponding to the directional impact of the wind. Eq. (4.7) can be subtracted from Eq. (4.4) and Eq. (4.5) to transfer all of the surfaces to a local coordinate system (LCS) giving the following equations

$$\vec{\mathbf{r}} = \begin{bmatrix} x_e - \delta(z)\cos(\theta_w) \\ y_e - \delta_y(z)\sin(\theta_w) \\ z_e - l \end{bmatrix} + D \begin{bmatrix} s_x \\ s_y \\ s_z \end{bmatrix} \tag{4.8}$$

$$\vec{\mathbf{s}} = \begin{bmatrix} r\cos\theta \\ r\sin\theta \\ 0 \end{bmatrix} \tag{4.9}$$

Figure 4.2 shows the geometrical interpretation of the result of transferring all components to the LCS. Now the ray effectively carries all the information regarding the displacement function and the height function whereas all of the cross sections of infinitesimal thickness are located at the origin of the GCS. However, since the value of z that produces the intersection is not known a priori, an infinite number of rays are generated when transferring the initial ray to the LCS. The true intersection will be found using an intersection algorithm in Matlab.

All function minimization calculations in Matlab utilize an objective function that is minimized with respect to a single variable. The objective function is formulated using the geometrical constraint that for a ray to intersect the mirror or receiver, it must satisfy the following equation

$$r^2 = x_{\text{surf}}^2 + y_{\text{surf}}^2 \tag{4.10}$$

Therefore, for an intersection to exist, x_{surf} and y_{surf} must equal the x- and y-components of the ray; that is, Eq. (4.8) must intersect Eq. (4.10)

$$x_{\text{surf}} = x_e - \delta(z)\cos(\theta_w) + Ds_{\text{loc},x} \tag{4.11}$$

$$y_{\text{surf}} = y_e - \delta(z)\sin(\theta_w) + Ds_{\text{loc},y} \tag{4.12}$$

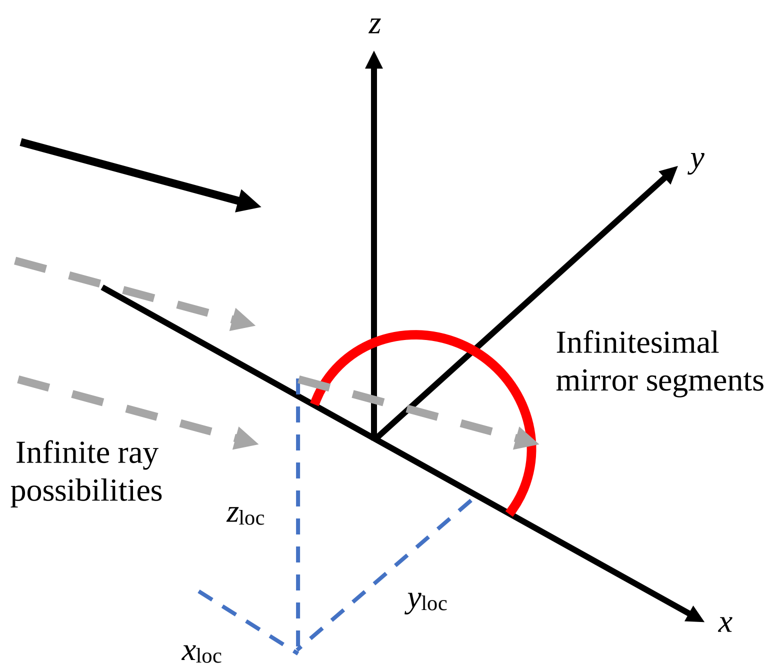

Figure 4.2. Mirror surface segmented into cross-sections of infinitesimal thickness and placed at the origin of the global coordinate system. Transferring the original ray (black arrows) in the GCS to the local coordinate system produces an infinite number of rays (grey dashed arrows) where the true ray is taken as the one that intersects the mirror.

Substituting Eqs. (4.11) and (4.12) into Eq. (4.10) and rearranging

$$0=\left[\left(x_e-\cos\left(\theta_w\right)\delta\left(z\right)+Ds_x\right)^2+\left(y_e-\sin\left(\theta_w\right)\delta\left(z\right)+Ds_y\right)\right]^{1/2}-r \tag{4.13}$$

where r is the radius of the mirror or receiver depending on which intersection is being calculated during run-time.

Eq. (4.13) is the objective function that needs to be satisfied with respect to the ray parameter D. There are three possible outcomes: 1) two solutions, one for each side of the mirror/receiver; 2) one solution where the ray is tangent to the receiver or mirror; or 3) no solutions where the ray does not intersect the system. In the most general case, all solutions must be known to fully constrain the system.

The objective function is very sensitive and can span many numerical magnitudes whereas the solvers required for this problem expect a tolerance on the order of 10^{-12} or less to be accurate. In order to be computationally inexpensive, we first solve for the value of D which produces the absolute minimum of Eq. (4.13) using the *fzero* solver. This is because the value of $D_{\min}$ is extremely close to those values of D which satisfy Eq. (4.13) as the ray does not have to travel far before intersecting a surface. Therefore, instead of searching the entire domain for those values of

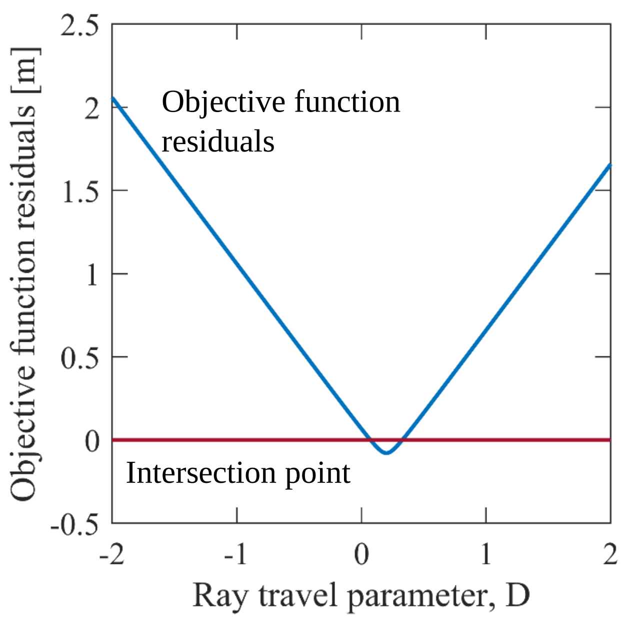

Figure 4.3. Objective function residuals during the objective function minimization process for intersection with the mirror. The blue line represents the residuals, while the orange line represents where the residuals equal 0, i.e. the point of intersection. The ray featured here intersects the mirror twice, producing one non-physical and one physical (true) solution.

D which satisfy Eq. (4.13), we instead only search a small range of values around D_{min} using the *fminbnd* solver. **Figure 4.3** shows the objective function residuals for the objective function minimization process.

In the case of the receiver intersection, we simply take the smallest, non-negative value of D that satisfies the objective function. Running the intersection algorithm on the mirror, however, may reveal a fictitious intersection. While the rim angle of the mirror may only span from 0 to 180°, the full equation of a circle (0 to 360°) is used to describe the mirror within the objective function. Therefore, after both values of D are found, we solve for their corresponding x- and y-coordinates and impose the constraint that the angle formed between the intersection point and the $+x$-axis in the GCS must be within the rim angle of the mirror, that is

$$\theta_{\min} \leq \theta \leq \theta_{\max} \tag{4.14}$$

For computational purposes, sequential MCRT methods are employed. The intersection algorithm is first run with respect to receiver; if the ray is absorbed by the receiver, the algorithm is terminated. If the intersection algorithm yields no intersection with the receiver, it then runs with respect to the mirror surface; if the ray is reflected by the mirror, the process loops and the receiver algorithm is run once more. The process continually repeats until either the ray is absorbed by the receiver or it is lost to the surroundings.

4.1.3. Specular reflection

If the ray intersects with the mirror, it must be reflected in a deterministic manner and continue to be traced until it is either terminated at the receiver or is lost to the surroundings. In order to properly trace the reflected ray, the normal vector at the point of intersection must be known. Consider for the moment the two-dimensional case where a ray reflects off a circle as given in **Figure 4.4 a)**. In this case the reflected ray must be directed towards the centre of the circle given by

$$x_{n,2D} = -r\cos\theta \tag{4.15}$$

$$y_{n,2D} = -r\sin\theta \tag{4.16}$$

where θ is given as

$$\theta = \tan^{-1}\left(\frac{y_{\text{int}}}{x_{\text{int}}}\right) \tag{4.17}$$

Now consider a beam experiencing a uniform load that deflects according to Euler-Bernoulli beam theory as given by **Figure 4.4 b)**. The slope is given as Eq. (3.9), reiterated here with a different variable for clarity

$$\beta = \frac{\omega l^3}{6EI} \tag{4.18}$$

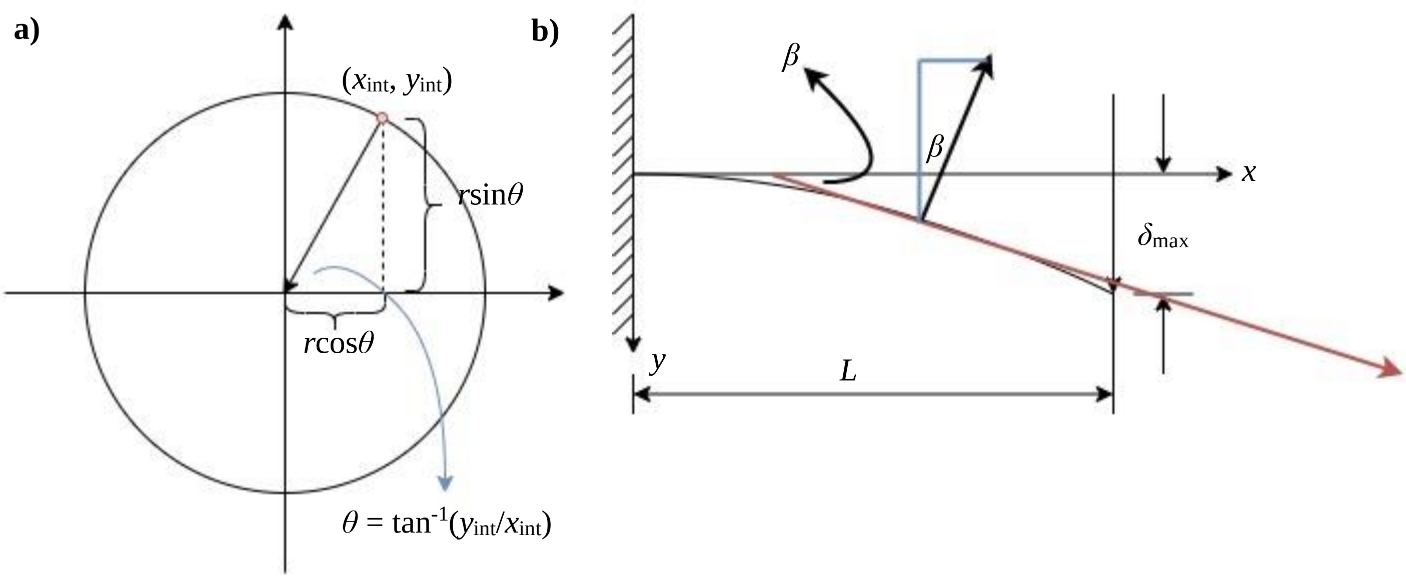

Figure 4.4. Two-dimensional analogues of the slope vector; **a)** shows a ray intersecting the two-dimensional mirror cross-section and **b)** shows the slope of a beam experiencing a uniform distributed load according to Euler-Bernoulli beam theory.

The z-direction vector is then given by

$$z_{n,2D} = r\sin\beta \tag{4.19}$$

The two-dimensional analogues can then be extended to three dimensions by considering the general three-dimensional mirror surface as shown in **Figure 4.5**.

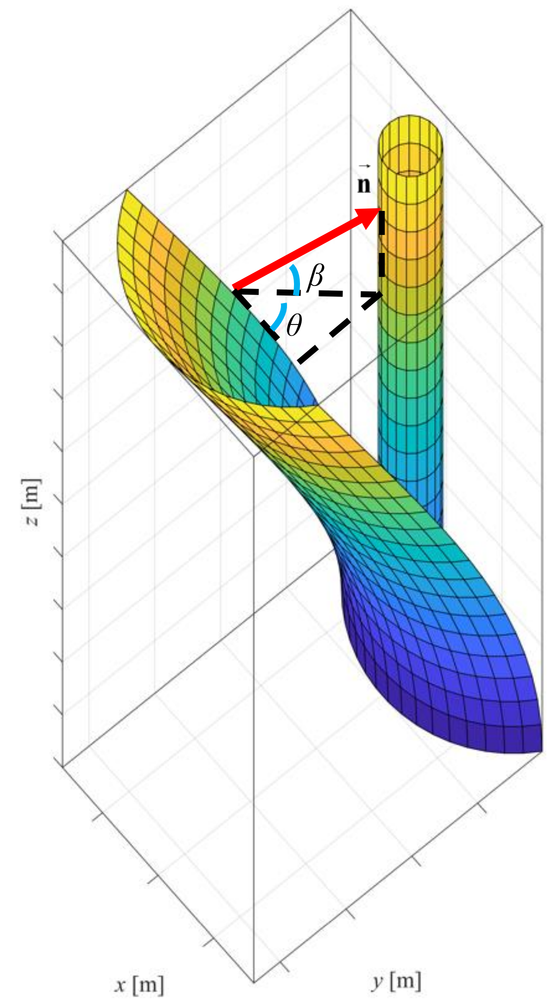

Figure 4.5. General three-dimensional slope vector constructed from the two-dimensional analogues

The final unit slope vector is given as

$$\mathbf{n} = \begin{bmatrix} -\dfrac{r\cos\theta\cos\beta}{\left\|\vec{\mathbf{n}}\right\|} \\ -\dfrac{r\sin\theta\cos\beta}{\left\|\vec{\mathbf{n}}\right\|} \\ \dfrac{r\sin\beta}{\left\|\vec{\mathbf{n}}\right\|} \end{bmatrix} \tag{4.20}$$

The signs on the *x*- and *y*-component of the slope vector are chosen such that the reflected ray always points in the correct direction. Finally, the formula for specular reflection can be applied

$$\vec{\mathbf{r}}_{\mathbf{spec}} = \hat{\mathbf{s}} - 2(\mathbf{n}\cdot\hat{\mathbf{s}})\mathbf{n} \tag{4.21}$$

where $\vec{\mathbf{r}}_{\text{spec}}$ is the reflected ray direction, $\hat{\mathbf{s}}$ is the unit direction vector of the incoming ray, and $\hat{\mathrm{n}}$ is the normal vector at the point of intersection.

The result of the Qa-MCRT is the intercept factor. In the strictest sense, the intercept factor is the ratio of the radiant power incident on the outlet aperture divided by the radiant power incident on the inlet aperture. However, because the Qa-MCRT does not consider the thermal aspect of each ray, the intercept factor is simply taken as the ratio of the number of rays incident on the receiver divided by the number of rays incident on the inlet aperture. The intercept factor provides a convenient means of understanding the optical losses, without having to thermally simulate the system.

4.1.4. Sensitivity analysis

One of the main benefits of commercial ray tracing softwares are that they can project a large number of rays for statistical significance. The numerical intersection algorithm along with Matlab's infrastructure is computationally expensive, requiring an abundance of memory to solve the system of equations presented here. The Qa-MCRT is typically run using 10000 rays, however, it remains to be determined whether this sample size is sufficient to achieve statistical significance. Using the geometry of the final prototype, the Qa-MCRT was run 5 times each using a sample size of 100, 1000, and 10000 rays. The results are shown in **Figure 4.6**. While it is normally beneficial to use a sample size of 10^7 to 10^8 rays, the Qa-MCRT shows reasonable convergence near 10000 rays, resulting in a standard deviation of 0.0024. Therefore, it can be concluded that this number of rays results in statistical significance for the case where the collector experiences no deflection.

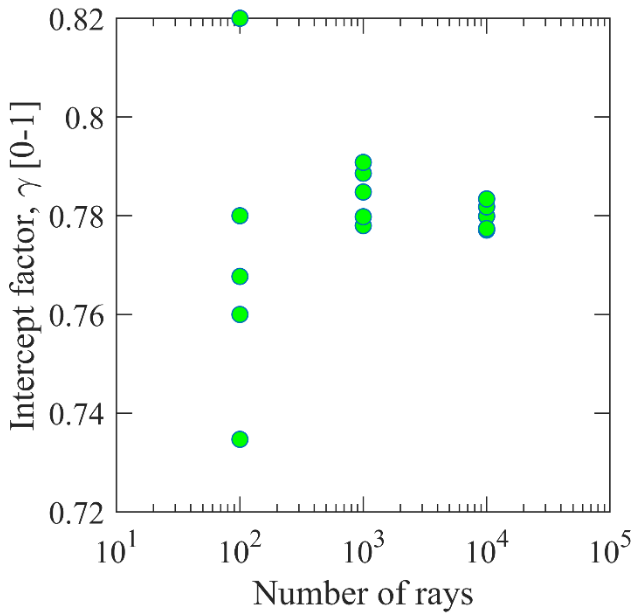

Figure 4.6. Qa-MCRT sensitivity analysis performed on a concentrator with dimensions equivalent to that of the final prototype developed.

4.1.5. Accuracy analysis

While the Qa-MCRT is novel in its application, its validity can still be verified by comparing the results of specific test cases to other Monte Carlo ray tracing packages. While other Monte Carlo ray tracing packages cannot analytically solve for the intersection of a surface that is curved along its length, they can solve for the simple case of a perfectly straight cylindrical concentrator. Hence, the Qa-MCRT can be verified by analyzing similar test cases using VeGaS. **Figure 4.7** shows the intercept factor for several test cases, the details of which will be provided in *Appendix C*. As can be seen from **Figure 4.7**, the Qa-MCRT performs almost identically to that of VeGaS, featuring an average difference of 0.0028 and a standard deviation of 0.0105. Therefore, the techniques used in the Qa-MCRT are verified.

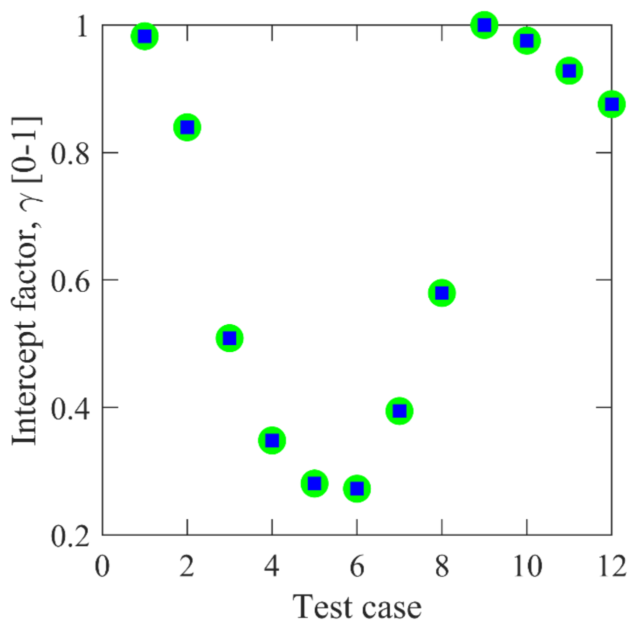

Figure 4.7. Verifying the validity of the Qa-MCRT by comparing the results of several test cases to that produced by VeGaS. The Qa-MCRT was run using 10^4 rays while VeGaS was run using 10^8 rays. The circle and square markers represent the result from the Qa-MCRT and VeGaS, respectively.

4.1.6. Qa-MCRT results

After verifying the sensitivity and accuracy of the Qa-MCRT it was then used to determine the intercept factor of a prototype solar collector under a variety of conditions. For this study, the independent parameter was chosen as wind speed and deflection for practicality with the understanding that the drag force can be obtained from either of these values. The Qa-MCRT was run using the geometry of the final prototype developed in the CooperLab with a sample size of 20,000 rays. In total, six test cases were analyzed. The first and second cases are representative of the solar collector experiencing a head and crosswind, respectively. The third case is representative of the solar collector experiencing a wind direction that is 45° from either the headwind or crosswind. Wind coming from this direction is referred to as “obliquewind”. In the first three cases the receiver is assumed to remain perfectly straight within the bag, that is, it experiences no deflection. In the remaining cases, the receiver is assumed to deflect the same amount as the collector. In all cases, the solar collector is assumed to perfectly track the sun. The results of the Qa-MCRT are given in **Figure 4.8**.

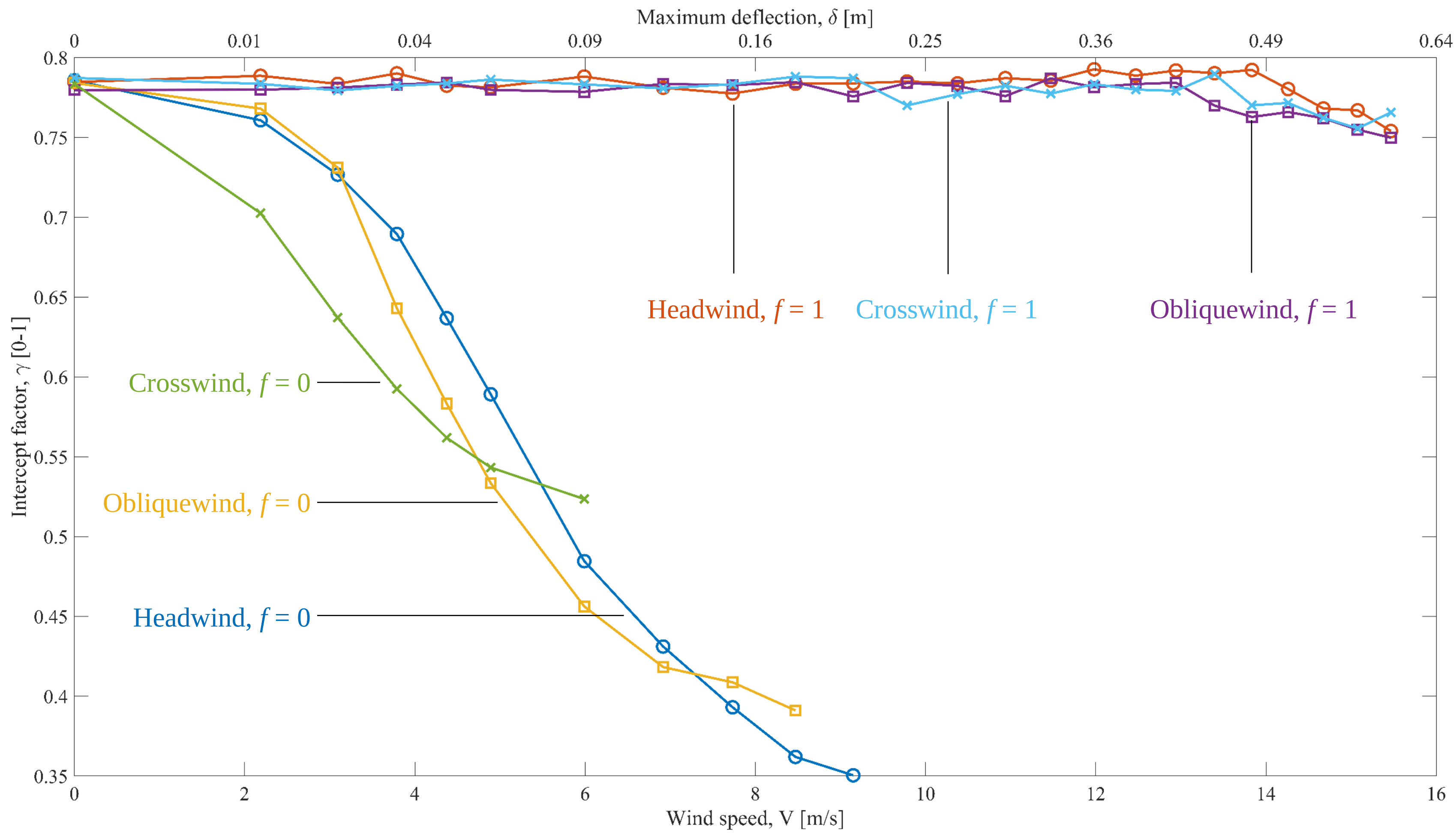

Figure 4.8. Results of the Qa-MCRT applied to three test cases. The geometry of the solar collector used in the simulation corresponds to that of the final prototype developed in the CooperLab. Obliquewind corresponds to a wind direction 45° from the headwind and crosswind. In all test cases, the solar collector is assumed to perfectly track the sun. The maximum deflection is given as the deflection at the tip of the collector. $f = 0$ indicates the case where the receiver experiences no deflection and $f = 1$ indicates the case where the receiver deflects the same amount as the collector. The markers correspond to the conditions for which the simulation was run.

It can be seen from **Figure 4.8**, that the results are subject to noise, especially in the latter half of the graph (greater than 10 m/s). This is due to the number of rays used in the analysis. For a vertical collector subject to no deflection, 10,000 rays is somewhat reasonable as the inlet aperture over which the rays are generated coincides with the inlet aperture of the collector itself. However, consider the case where the collector experiences a crosswind. The inlet aperture over which rays are generated will be larger than the inlet aperture of the collector. Then, many of the rays generated will be immediately lost before entering the system. This results in an immediate decrease in the denominator of the intercept factor, reducing the sample size and generating noise.

In the cases where the receiver experiences no deflection, the corresponding curves in **Figure 4.8** do not cover the full domain. This is due to a spatial constraint of the receiver within the bag. At the maximum deflection, the outer bag contacts the receiver – any further deflection would violate the verticality of the receiver. Nevertheless, it can be seen that even small deflections on the order of centimetres can produce significant spillage. At nearly 5 cm tip deflection, or wind speeds of 4 m/s, the intercept factor reduces to approximately 0.65 in the case of a crosswind. At higher wind speeds, the spillage increases even further significantly reducing the optical performance. Essentially, a significant deviation in the normal vector at the intersection point on the mirror causes reflected rays to miss the receiver. Conversely, there is no notable reduction in the intercept factor if the receiver deflects an amount equal to the outer-envelope ($f = 1$). However, both $f = 0$ and $f = 1$ are highly idealized scenarios. In reality, the receiver is in a statically indeterminate state and its exact curvature may not be readily calculated. Therefore, prescribing $f = 0$ and $f = 1$ gives a conservative and liberal estimate of the optical performance losses, respectively.

It should also be noted that the solar collectors prescribed by the geometric argument provided in *Chapter 3* would not be deployed over a large portion of the domain given in **Figure 4.8**. In fact, at an inflation pressure of 1.5 psi, the prototype used for the above analysis would begin to wrinkle at wind speeds of approximately 8 m/s and collapse at 16 m/s. Therefore, the load-deflection curve becomes non-linear in the latter half of **Figure 4.8**, and the deflection equations used may not be applicable. The region from 8 to 16 m/s then is only provided to complete the optical study. Therefore, even the noise in this region is insignificant since it occurs in an impractical range of **Figure 4.8**.

Chapter 5

Thermal modelling

Before performing a comprehensive on-sun experiment, it is necessary to characterize the system from a thermal perspective. In this chapter we first start by modelling the receiver tube using the approach of an equivalent thermal circuit. The thermal circuit is then modelled in Simulink which takes flow rate as the input and outputs the temperature of the heat transfer fluid, wall temperatures of the receiver and dummy tube, local heat transfer coefficients, and Q_{gain} and Q_{loss}. The results of the simulations are of great importance for two reasons. First, the results enable the direct characterization of the flow rate which optimizes thermal performance and second, the results provide the expected thermal performance in advance of the final on-sun experiment.

5.1. Energy flows and equivalent thermal circuit

A visual representation of the energy flows from the source to the receiver is shown in **Figure 5.1**. Once all of the thermal losses on the way to the receiver are accounted and we have a constitutive value for Q_{gain}, we can then focus our attention on the receiver to study the transfer of heat to the HTF. The equivalent thermal circuit of the concentric receiver tube is shown in **Figure 5.2**. Q_{in} represents the concentrated sunlight distributed uniformly over the outer receiver wall. As the receiver wall is heated, it may either contribute to Q_{gain} or Q_{loss}. That is, the heat may either be lost to the surroundings by natural convection or radiation (Q_{loss}) or may conduct through the outer receiver wall to the inner receiver wall (Q_{gain}). The HTF on the inside of the receiver (annulus) is then heated by the inner receiver wall by convection, but will simultaneously lose heat by convection to the outer wall of the dummy tube. Similarly, the dummy tube will conduct heat from its outer to its inner wall and the HTF on the inside of the dummy tube will be heated through convection. Since the flow paths of the receiver and dummy tube are linked at the top, the HTF on the inside of the dummy tube will eventually flow into the annular region of the receiver.

Therefore, a line connects the nodes of $T_{\text{air, inner}}$ and $T_{\text{air, annulus}}$ to represent that flow of energy by the HTF. Finally, the fluid is extracted through the bottom of the annular region of the receiver.ds

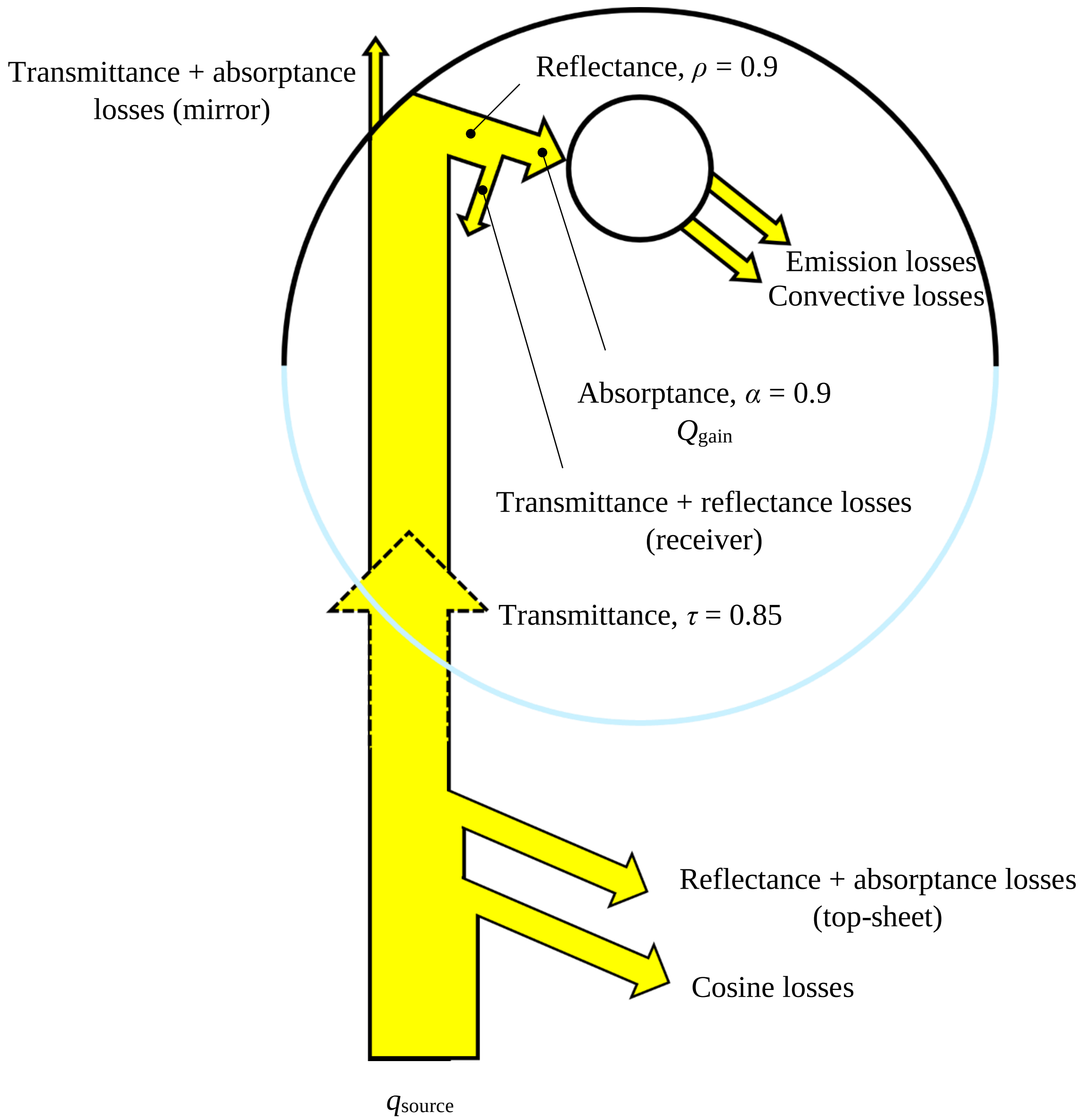

Figure 5.1. Energy flows from the source to the receiver.

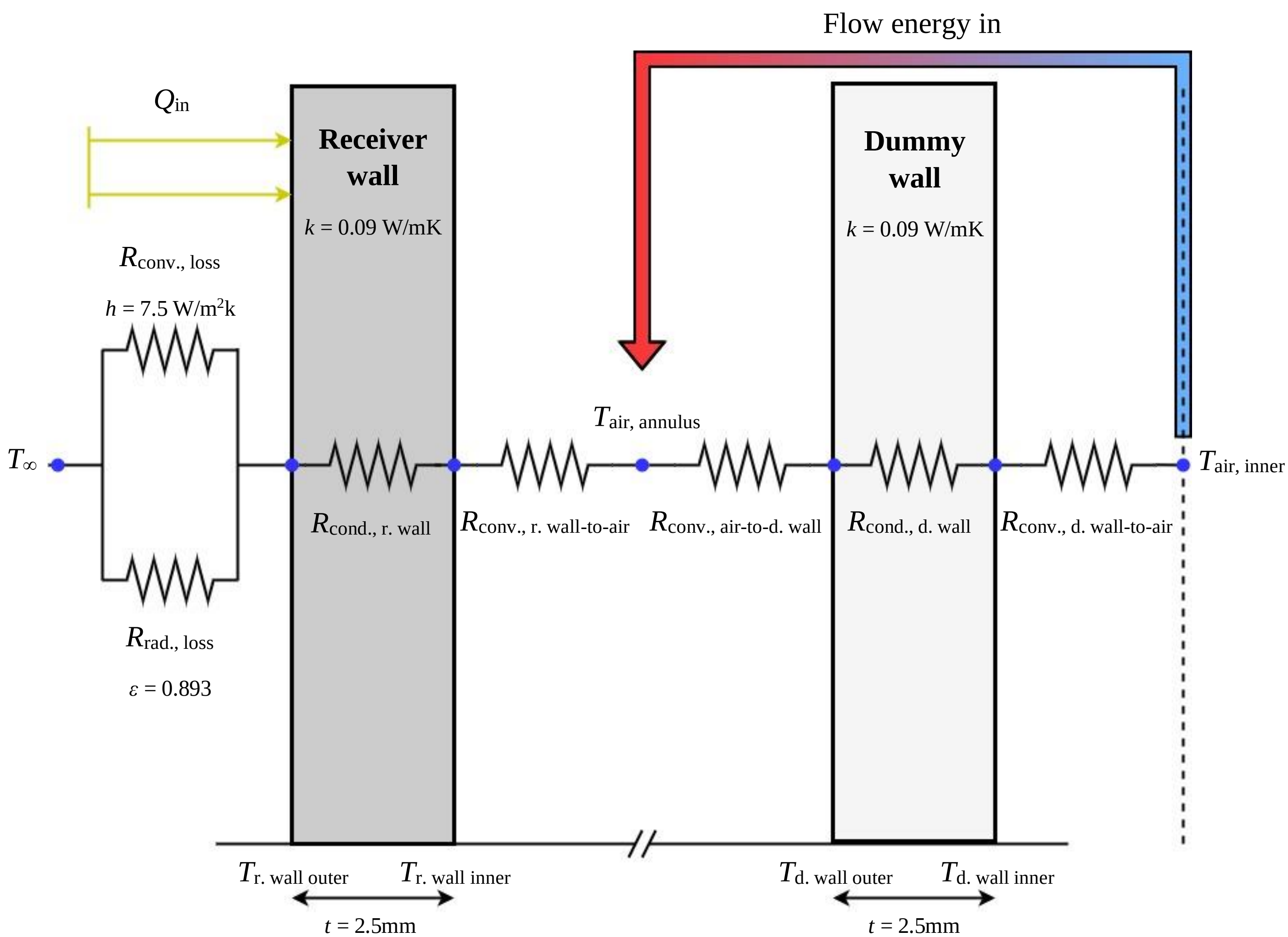

Figure 5.2. Receiver tube thermal circuit. The line labelled flow energy in represents the fluid as it flows from the dummy tube into the receiver tube and the line labelled flow out represents the fluid extraction point.

5.2. Thermal model in Simulink

The approach taken to simulate the vertically oriented solar collector was to model the concentric receiver tube alone. The effects of top sheet transparency, mirror reflectance, and cosine losses were introduced as static design variables in the heat input which will be explained shortly. Simulating the system in this way reduces the overall complexity of the simulation while still maintaining accuracy.

Both the dummy tube which brings the air upwards and the receiver tube which simultaneously heats the air and leads it towards the outlet were segmented into 6" long segments. The benefit of doing so is that we can obtain a profile of the wall temperature and temperature of the air as it is heated throughout the system. Each segment of the receiver tube was subjected to an irradiance equal to the following equation

$$Q_{\text{in,1-seg}} = \tfrac{1}{18}\tau\rho\alpha\gamma \cdot L_{\text{AP}}W_{\text{AP}} \cdot \text{DNI}\cos\theta \tag{5.1}$$

The optical properties of the various films in the system are built directly into Eq. (5.1): τ is the transmittance of the top-sheet equal to 0.85, ρ is the reflectance of the mirror equal to 0.9, α is the absorptance of the receiver equal to 0.9, and γ is the intercept factor equal to 0.7823. The intercept factor is not equal to 1 as the mirror was chosen to be exactly one-half of the outer-envelope for both ease of construction and cost-consideration. L_{AP} and W_{AP} are given as the total projected length and width of the collector. The DNI represents the direct normal irradiance which was input as a nominal value of 970 W/m^2. The equation is then multiplied by a factor of cosθ corresponding to the elevation angle and is divided by 18 as there are 18 uniformly illuminated segments. The total heat into a segment is then given as 11.31 W, or 203.6 W over the entire receiver.

While the thermal circuit is quite simple to understand, the Simulink model shown in **Figure 5.3** is much more nuanced. In the rest of this section, we will discuss the parts of the model that are not immediately apparent. First, the flow of heat from the outer receiver wall to the heat transfer fluid in the annulus is computed internally using a native Simulink component called “pipe element (G)”. The characteristic thickness and thermal conductivity of this component (modelled after butyl rubber) is equal to 2.5 mm and 0.09 W/mK, respectively. Once the HTF is flowing through the annular region it may also heat the wall of the dummy tube (which has the same thickness and thermal conductivity as the receiver). However, the thermal conserving port (port H on the receiver) cannot be directly connected to the wall of the dummy tube. Doing so will cause a portion of Q_{in} to flow into the dummy tube, causing an erroneous heat gain. Instead, we employ a clever technique whereby the HTF flows into a fictitious pipe element (after flowing through and being heated by the receiver) with hydraulic diameter equal to that of the annular region whose purpose is to only give up heat to the dummy tube wall. This will induce a fictitious pressure drop which can be set to 0. However, for the purposes of this simulation the pressure was ignored. Finally, since the value of emittance for radiative losses is dependent on operating temperature, its value was changed iteratively to obtain accurate results. The final value of emittance used was 0.893. Obtaining an accurate value for the heat transfer coefficient for convective losses, however, involves several assumptions regarding the flow regime over the receiver tube. For this reason, we attempt to solve for the heat transfer coefficient assuming the existence of both free and forced convection. According to Çengel and Ghajar [34], the Nusselt number for free convection over a vertical cylinder is identical to that of a vertical plate assuming the following is true

$$D \geq \frac{35L}{\mathrm{Gr}_L^{1/4}} \tag{5.2}$$

where L is the length of the collector and Gr_L is the Grashof number equal to

$$\mathrm{Gr}_L = \frac{g\beta(T_s - T_\infty)L^3}{\nu^2} \tag{5.3}$$

In Eq. (5.3), g is the constant for gravitational acceleration in $\mathrm{m/s^2}$, β is the coefficient of volume expansion in K, T_s is the surface temperature of the receiver in °C, T_∞ is the temperature of the fluid sufficiently far from the surface in °C, L is the characteristic length of the geometry (in this case the length of the collector), and ν is the kinematic viscosity of the fluid in $\mathrm{m^2/s}$. For the present analysis we assume that air is an ideal gas such that $\beta = 1/T$ where $T = 293$ K, $T_s = 323$ K, $T_\infty = 293$ K, $L = 2.74$ m, and $\nu = 1.516\times10^{-5}\ \mathrm{m^2/s}$, where all values are obtained iteratively. Solving Eq. (5.3) with these values gives a Grashof number equal to 8.71×10^{10} and therefore Eq. (5.2) is satisfied. Since Eq. (5.2) is satisfied, we can then use the following equation for the Nusselt number for free convection over a vertical plate [34]

$$\mathrm{Nu}_{\mathrm{free}} = \left\{ 0.825 + \frac{0.387\mathrm{Ra}_L^{1/6}}{\left[1 + \left(0.492/\mathrm{Pr}\right)^{9/16}\right]^{8/27}} \right\}^2 \tag{5.4}$$

where Pr is the Prandtl number equal to 0.73 and Ra_L is the Rayleigh number defined as [34]

$$\mathrm{Ra}_L = \mathrm{Gr}_L\,\mathrm{Pr} \tag{5.5}$$

Solving Eq. (5.4) gives a Nusselt number equal to 456.43.

In addition to free convection, we then check if forced convection is prominent within the system. Unfortunately, correlations for forced convection over vertical cylinders are scarce, and are often given within literature only for highly specific cases. Even amongst the correlations that do exist, they often show contradictory results [35]. Nevertheless, we assume that a flow is induced by a leak in the top of the bag (near the clamping point) equal to 10% of the inlet flow rate. Assuming the flow rate is equal to 1 scfm, the flow rate induced in the bag in SI units is given as 4.72×10^{-5} m^3/s. Dividing by the cross-sectional area of the collectors gives the average flow velocity within the bag (and thus, around the receiver) of $V = 7.33\times10^{-4}$ m/s. The Reynolds number is then calculated using

$$\mathrm{Re}_L = \frac{VL_c}{\nu} \tag{5.6}$$

which is equal to 132. For the present case, we assume the correlation for forced convection over a flat plate subject to a uniform heat flux according to Çengel and Ghajar [34] given as

$$\mathrm{Nu}_{L,\mathrm{forced}} = 0.453\,\mathrm{Re}_L^{\,0.5}\,\mathrm{Pr}^{1/3} \tag{5.7}$$

Eq. (5.7) gives the Nusselt number for laminar flow at the top of the receiver (where heat transfer is the greatest) and is equal to 4.69. Due to the significant difference between the Nusselt number for free and forced convection, it can be seen that free convection dominates. Nevertheless, we can calculate the combined Nusselt number using [34]

$$\mathrm{Nu}_{\mathrm{combined}} = \left(\mathrm{Nu}^n{}_{\mathrm{forced}} + \mathrm{Nu}^n{}_{\mathrm{free}}\right)^{1/n} \tag{5.8}$$

where n is equal to 3 for the vertical orientation. Therefore, the combined Nusselt number is equal to 456.42. Then, the heat transfer coefficient is calculated using

$$h = \frac{\mathrm{Nu}_{\mathrm{combined}}\,k}{L} \tag{5.9}$$

where k is the thermal conductivity of air given as 0.025 W/mK. The final value of h is equal to 4.2 W/m^{2}K, however, this value was later increased to 7.5 W/m^{2}K to capture some of the complexities in the flow regime within the outer-envelope and to better match reality.

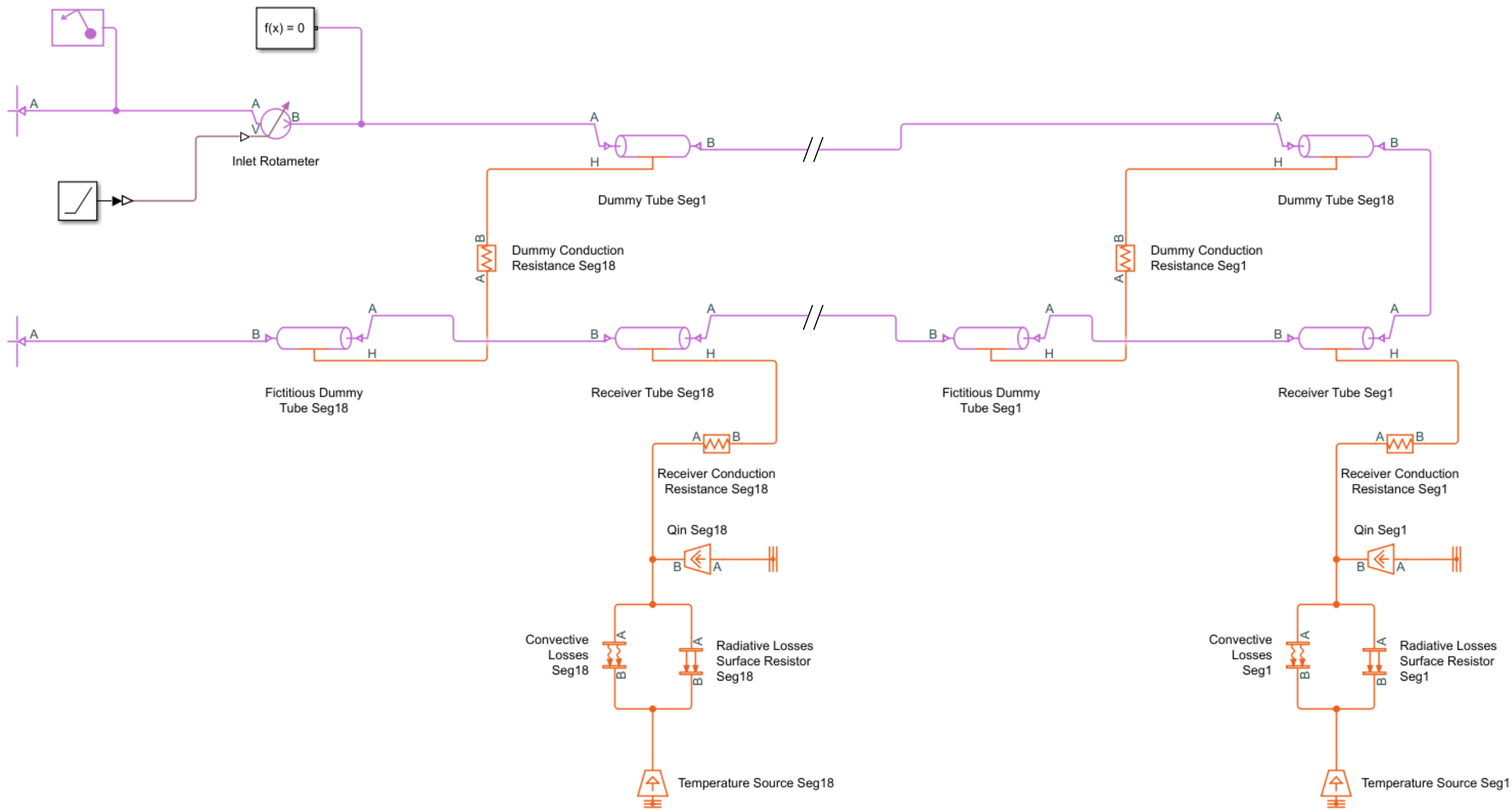

Figure 5.3. Simulink block diagram. The purple lines represent the flow path of the fluid, and the orange lines represent the heat flow path.

5.3. Flow setup

It was hypothesized a priori, that there would be two competing effects that govern the outlet temperature. The overall heat gained by the receiver can be characterized using the following equation utilizing the specific heat capacity

$$Q_{\text{gain}} = \dot{m}c_p \left(T_{\text{out}} - T_{\text{in}}\right) \tag{5.10}$$

Conversely, Newton's law of cooling can be used to describe the local heat gain at any point along the receiver using the following equation

$$Q = hA\Delta T \tag{5.11}$$

According to Eq. (5.10), for a specific Q_{gain}, decreasing the velocity of the fluid must be accompanied by a corresponding increase in $T_{\text{out}} - T_{\text{in}}$. According to Eq. (5.11), however, an increase in the velocity of the fluid will cause a direct increase to the heat transfer coefficient and thus more heat will be absorbed. Therefore, in addition to the simulation providing the expected thermal performance, it will also determine the optimal design parameters when performing an on-sun experiment.

5.4. Simulation results

The results of the simulation are given in four separate plots. **Figure 5.4** displays the dependence of temperatures and efficiency on flow rate, the average local heat transfer coefficient, and the power output determined by Eq. (5.10). Three different heat transfer coefficients were provided as recommended in Transport Phenomena by R. Byron Bird, Warren E. Stewart, and Edwin N. Lightfoot [36]

$$h_1 = \frac{Q_{\text{gain,local}}}{\left(\pi DL\right)\left(T_{01} - T_{b1}\right)} \tag{5.12}$$

$$h_a = \frac{Q_{\text{gain,local}}}{\left(\pi DL\right)\dfrac{\left(T_{01} - T_{b1}\right) + \left(T_{02} - T_{b2}\right)}{2}} \tag{5.13}$$

$$h_{\ln} = \frac{Q_{\text{gain,local}}}{\left(\pi DL\right)\dfrac{\left(T_{01}-T_{b1}\right)-\left(T_{02}-T_{b2}\right)}{\ln\left(T_{01}-T_{b1}\right)-\ln\left(T_{02}-T_{b2}\right)}} \tag{5.14}$$

where T_{01} and T_{02} represent the wall temperature at the inlet and outlet, respectively and T_{b1} and T_{b2} represent the bulk fluid temperature at the inlet and outlet, respectively. That is, h_1 is based only on the temperature difference at the inlet, h_a is based on the arithmetic mean of the temperature difference from the inlet to the outlet, and h_{ln} is based on the logarithmic mean of the temperature difference from the inlet to the outlet [36]. According to Byron Bird, Stewart, and Lightfoot, the logarithmic heat transfer coefficient is most preferable as it is less dependent on aspect ratios [36]. Furthermore, the efficiency is rigorously defined as

$$\eta = \frac{Q_{\text{gain}}}{Q_{\text{in}}} = \frac{\dot{m}c_p\left(T_{\text{out}}-T_{\text{in}}\right)}{\text{DNI}\cos\theta A_i} \tag{5.15}$$

Since energy is conserved, we can break down Q_{gain} in the first representation of efficiency in Eq. (5.15) as

$$Q_{\text{in}} = Q_{\text{gain}} + Q_{\text{loss}} \tag{5.16}$$

or alternatively

$$Q_{\text{gain}} = Q_{\text{in}} - Q_{\text{loss}} \tag{5.17}$$

Substituting Eq. (5.17) into Eq. (5.15) we arrive at a simple definition of efficiency defined as

$$\eta = 1 - \frac{Q_{\text{losses}}}{Q_{\text{in}}} \tag{5.18}$$

Figure 5.5 displays an area plot of how much heat is being gained by the system and how much heat is lost due to convection and radiation. **Figure 5.6** and **Figure 5.7** looks at the evolution of temperatures throughout the system. **Figure 5.6** displays the temperature of the air as it evolves throughout the system and **Figure 5.7** displays the wall temperatures of the receiver and dummy tube.

It is apparent from **Figure 5.4 a)** that there exists a flow rate which produces the maximum operating temperature by balancing the opposing effects of Eq. (5.10) and Eq. (5.11). Fortunately, the optimal flow rate of around 1 scfm is on the lower end of the scale thus requiring less energy to produce. Additionally, this flow rate is easily replicable on any analog system. For a flow rate of 1 scfm it can be from **Figure 5.4 c)** that the expected output power is approximately equal to 12.7 W, increasing with increasing flow rate. Conversely, the efficiency is quite low, equaling approximately 7%. **Figure 5.5** explains this phenomenon as only a fraction of Q_{in} actually contributes to Q_{gain}. That is, since re-radiation is minimally supressed by the receiver, and since nothing is being done to prevent convection currents from forming, Q_{gain} will be significantly lower than Q_{in}. At the operating temperature of about 44°C, 39% of the incident heat (or 79.17 W) is being re-emitted by the receiver and a further 54% (or 109 W) is convecting off the surface of the receiver. At higher flow rates, these losses tend to decrease, however the compromising effect of increasing flow rate will result in an overall decrease in $T_{\mathrm{out}} - T_{\mathrm{in}}$ according to Eq. (5.10). Recommendations for increasing outlet temperature and efficiency will be provided in a later section.

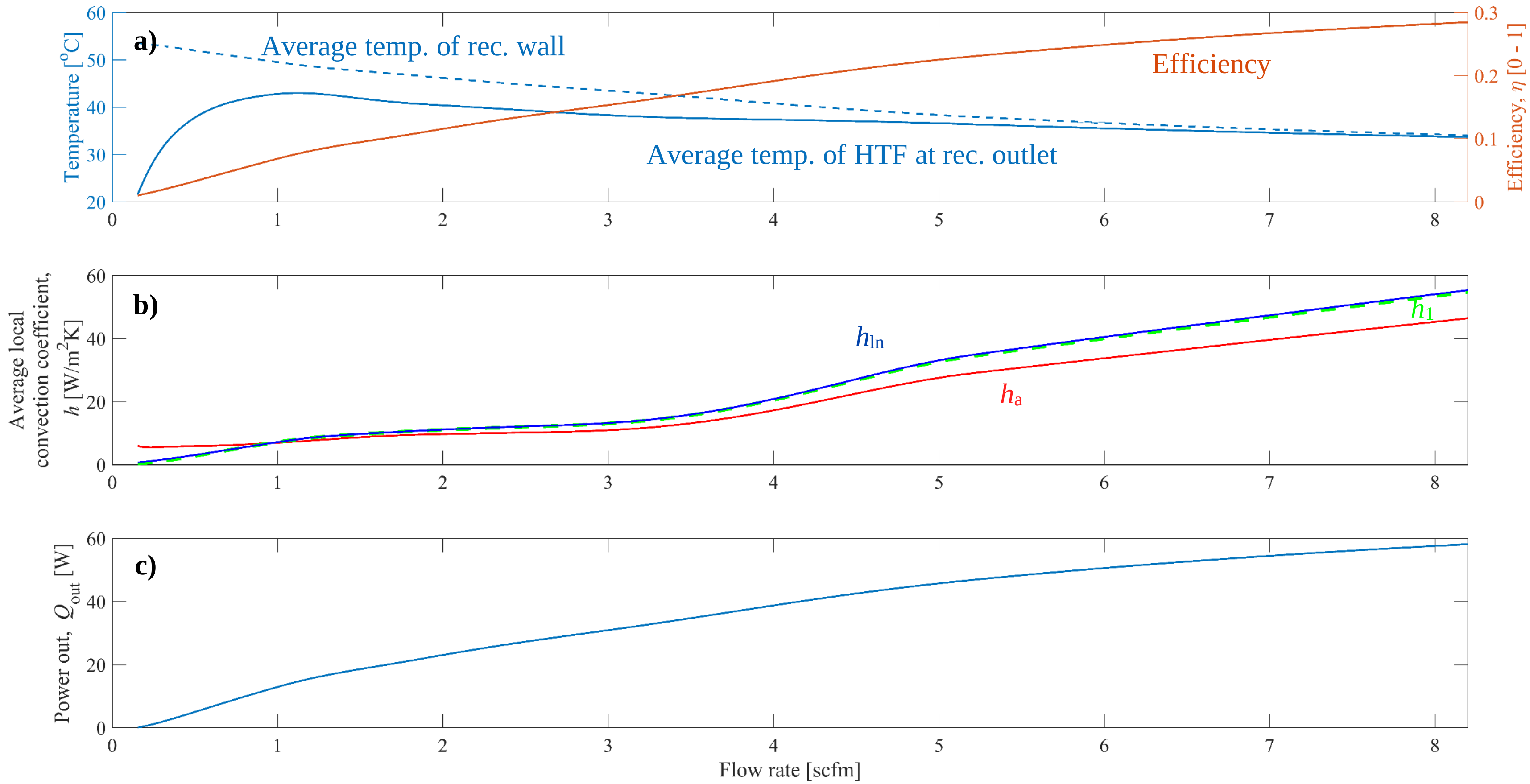

Figure 5.4. Results of thermal simulation showing the effect of changing flow rate on: **a)** outlet fluid temperature, wall temperature, and efficiency; **b)** average local heat transfer coefficients h_1, h_a, and h_{ln} (h_a is represented visually by the dashed green line); and **c)** the power output in W.

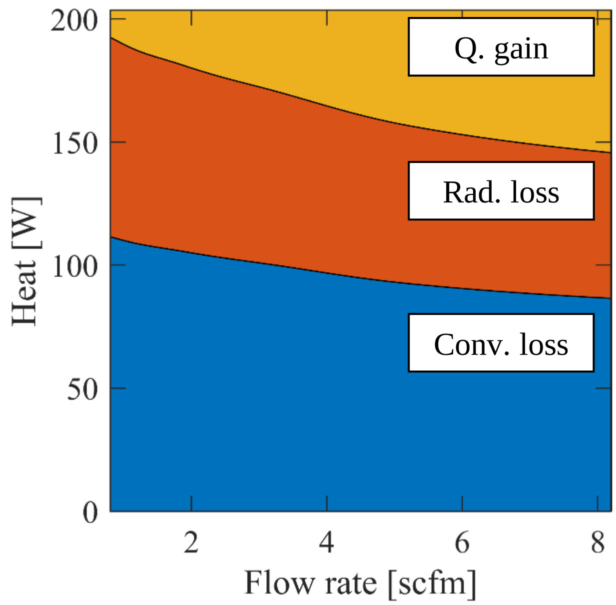

Figure 5.5. Dependence of Q_{in} and Q_{loss} on flow rate.

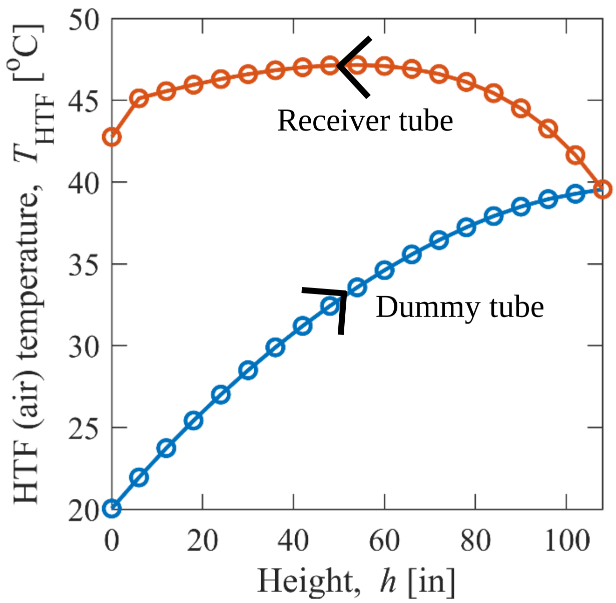

Figure 5.6. Evolution of air temperature throughout the concentric receiver at 1 scfm. The arrows represent the flow direction.

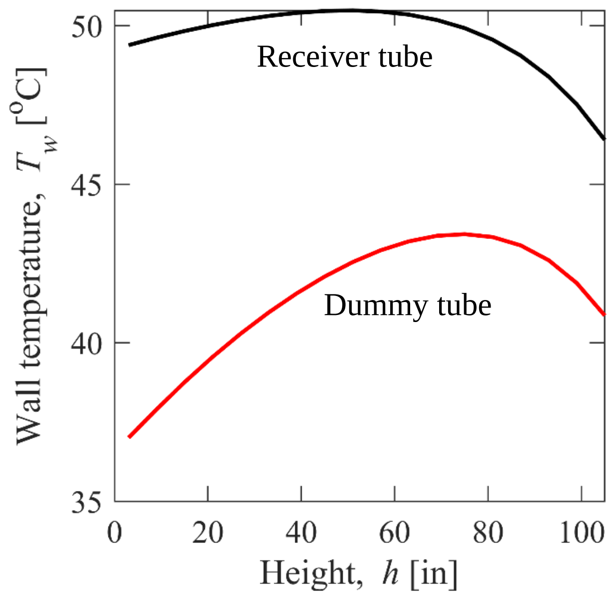

Figure 5.7. Evolution of the wall temperature across the concentric receiver.

All three local heat transfer coefficients in **Figure 5.4 b)** are steadily increasing with flow rate as expected. That is, at greater flow rates the difference between the temperature of the wall and the temperature of the bulk fluid decreases, thus resulting in a greater heat transfer coefficient due to the inverse relationship. In other words, as the velocity increases, so does the local heat transfer coefficient.

Figure 5.6 displays very interesting results. First, the difference in temperature between the inlet and outlet of the dummy tube is greater than the difference between the inlet and outlet of the receiver. This indicates that there is a significant transfer of heat from the air in the annulus to the air in the dummy tube. This is of no detriment to the system, however, as the air in the dummy tube eventually flows back into the receiver. Interestingly, but not unsurprisingly, the temperature of the air in the second half of the receiver actually decreases by a few degrees. This is because the hot air towards the bottom of the receiver is in thermal contact with the supply air through the wall of the dummy tube. Because the supply air has not been sufficiently heated at this point, the stark temperature difference draws a large amount of heat away from the heat in the receiver and thus decreasing the overall temperature. Finally, the air at the outlet of the receiver experiences a temperature drop. This can be attributed to the sudden expansion of the fluid as it leaves the system. For example, consider the density of the fluid to be approximately constant. Then due to the inverse relationship of pressure and temperature, a drop in pressure to atmospheric must cause a corresponding decrease in temperature. Therefore, the simulation indicates that the maximum achievable outlet temperature is roughly 42°C resulting in a temperature difference of 22°C.

Figure 5.7 displays nearly the same shape as **Figure 5.6** as the walls of the receiver and the heat transfer fluid are in thermal contact. Interestingly, the temperature of the wall of the dummy tube does not monotonically increase like the heat transfer fluid flowing through it. For example, in the region of the dummy tube spanning from h = 75" to h = 105", the temperature of the wall decreases from 43°C to 40°C, while the corresponding temperature of the HTF increases from 37°C to 39°C. Additionally, the temperature of the HTF in the receiver and the receiver wall plateau around h = 66" to h = 42" indicating that the two are in thermal equilibrium. Finally, the outlet of the dummy tube and the inlet of the receiver tube are not at the same temperature as the receiver tube is being irradiated while the dummy tube is subject only to convection.

Chapter 6

Experimental results

Chapters 4 and 5 provided a unique perspective into the expected operating conditions of a vertically oriented solar concentrator from an optical and thermal perspective. In this chapter we construct several prototypes to characterize optical quantities that cannot be simulated, such as the effects of wrinkling on concentration. We then perform an on-sun optical test to determine the experimental flux distribution over a Lambertian target. Finally, we conclude with a cumulative on-sun thermal experiment to determine the exact thermal performance of the concentrator.

6.1. Laser experiment overview

Previous researchers found a great deal of success in quantifying the effect of surface imperfections by implementing surface error into a Monte Carlo ray tracing simulation for a parabolic trough concentrator [7]. The surface errors, although microscopic in nature (on the order of σ = 0-10 mrad), were found to have a significant effect on the concentration ratio on the target plane [7]. Although these errors are inevitable due to the manufacturing processes that produces the mirror, it was hypothesized that the vertical configuration would be subject to macroscopic errors as well in the form of wrinkling arising from severe working of the fabric. It is for this reason that we attempted to characterize the effects of wrinkling on the target plane.

While microscopic slope errors can be generated fairly simply by imposing a probability density distribution within a simulation [7], macroscopic errors are much more difficult to characterize. The sizes of a wrinkle may vary substantially in magnitude, and reflection off a wrinkle may not be as simple as imposing a deviation in the normal vector by a specified amount. It is for this reason that studying the effects of wrinkling had to be done experimentally as opposed to simulative. A physical experiment also allows for the inclusion of pressure in the study, in that it can be determined whether increasing the bag pressure will smoothen out the mirror and reduce the effect of wrinkling. The downside of a physical experiment, as will be shown shortly, is that the results are largely qualitative.

6.1.1. Laser experiment methodology

For the following experiment, a laser was fixed to a track that could move both vertically along the length of the concentrator and laterally across its width. Rulers were used in both dimensions such that the position of the laser was repeatable between tests. The laser was used to target specific points along the surface of the mirror to simulate incoming radiation, and its output was captured on a Lambertian target positioned at the focal plane. The Lambertian target was made of a 98% diffuse reflector film from WhiteOptics. Due to the structural framing, however, only one half of the mirror could be utilized. The Lambertian target is shown in **Figure 6.1**. The diffusely reflected radiation was recorded with a Sony a6000 mirrorless camera. By moving the laser a set amount in the vertical and horizontal directions, and imaging each time, a set of images with discrete laser locations was produced. These images were then superimposed to produce a single map of discrete laser points that qualitatively describes the performance of the mirror. The experiment itself was fixed atop an optical table supported by air columns to reduce the effect of vibrations from within the building. **Figure 6.2** shows the general set-up for all laser tests.

Figure 6.1. Lambertian target made of a 98% diffuse reflector film from WhiteOptics supported by aluminum framing. Due to the framing, the Lambertian target can only map 1 side of the mirror.

The discrete images were superimposed using a masking technique. Before each experiment, a template was taken where the Lambertian target was not illuminated by the laser. The static, or template image, was then imported into Matlab along with the images from the experiment, where each picture was represented by a 3D array of 8-bit unsigned integer (uint-8) values. The *i* and *j* components of each array correspond to the location, whereas the value within each cell represents the intensity of a specific colour. The first array spanning in the third

Figure 6.2. Experimental set-up for laser tests. The laser is mounted atop a track which slides both vertically and horizontally to fully define the system. A level is mounted to the cross member where the laser is fixed to ensure that it stays level with respect to the frame.

dimension holds the data of interest, as it represents the intensity of red within each picture and therefore holds the spatial data of the laser. This array from the template is subtracted from the red array of each image in the set, giving a Δred array. All values within the array are then turned to 0 unless they are equal to or greater than an intensity value corresponding to the colour of the laser. At this point, we have an array which is 0 everywhere, except for the cluster which holds both the position data and the intensity of the laser, referred to as a mask. The equivalent entries of the red array in the static image are then turned off and substituted with the data corresponding to the mask to superimpose the final results. It is for these reasons that the physical set-up must remain undisturbed throughout the entirety of the tests, otherwise the position data of the static image and the images taken during the experiment will not be identical. Finally, the results had their perspectives corrected to account for the fact that the camera was not perpendicular to the Lambertian target.

6.1.2. On-axis laser experiment

The first set of laser experiments was performed by keeping the laser perfectly straight to mimic on-axis rays. The laser was moved in increments of 5" vertically and 1" horizontally across the entirety of the surface of the mirror. The mirror was intentionally worked physically so as to induce a significant amount of wrinkling across the surface. The results of the on-axis experiment are shown in **Figure 6.3**.

As can be seen from **Figure 6.3**, operating pressure has a significant effect on reducing wrinkling. At 0.5 psi, the laser at the majority of points loses its point focus and scatters in a non-deterministic manner. The integrity of the vertical and horizontal lines is not maintained as the wrinkles reflect the rays in random directions. The wrinkling towards the middle of the target is particularly noticeable. The wrinkling towards the middle of the target is particularly noticeable. Either the laser splits into multiple foci on the target or scatters so significantly that it forms an area of contiguous illumination. At 1 psi, the vertical and horizontal nature of the test is preserved. That is, the majority of points are distributed along a perfect vertical and horizontal line. The reflected rays have also reduced to a discrete point corresponding to the incoming ray. Some scattering may be observed towards the middle of the target, however, it is less exaggerated than in the 0.5 psi case. At 1.5 psi, these effects are further reduced, albeit minorly. The improvements are noted particularly towards the middle where the wrinkling has proven to be more significant. Following the experiment, areas of particularly bad wrinkling were intentionally targeted to isolate their effects on the reflected rays and further exacerbate the results shown here. These results are shown in **Figure 6.4**.

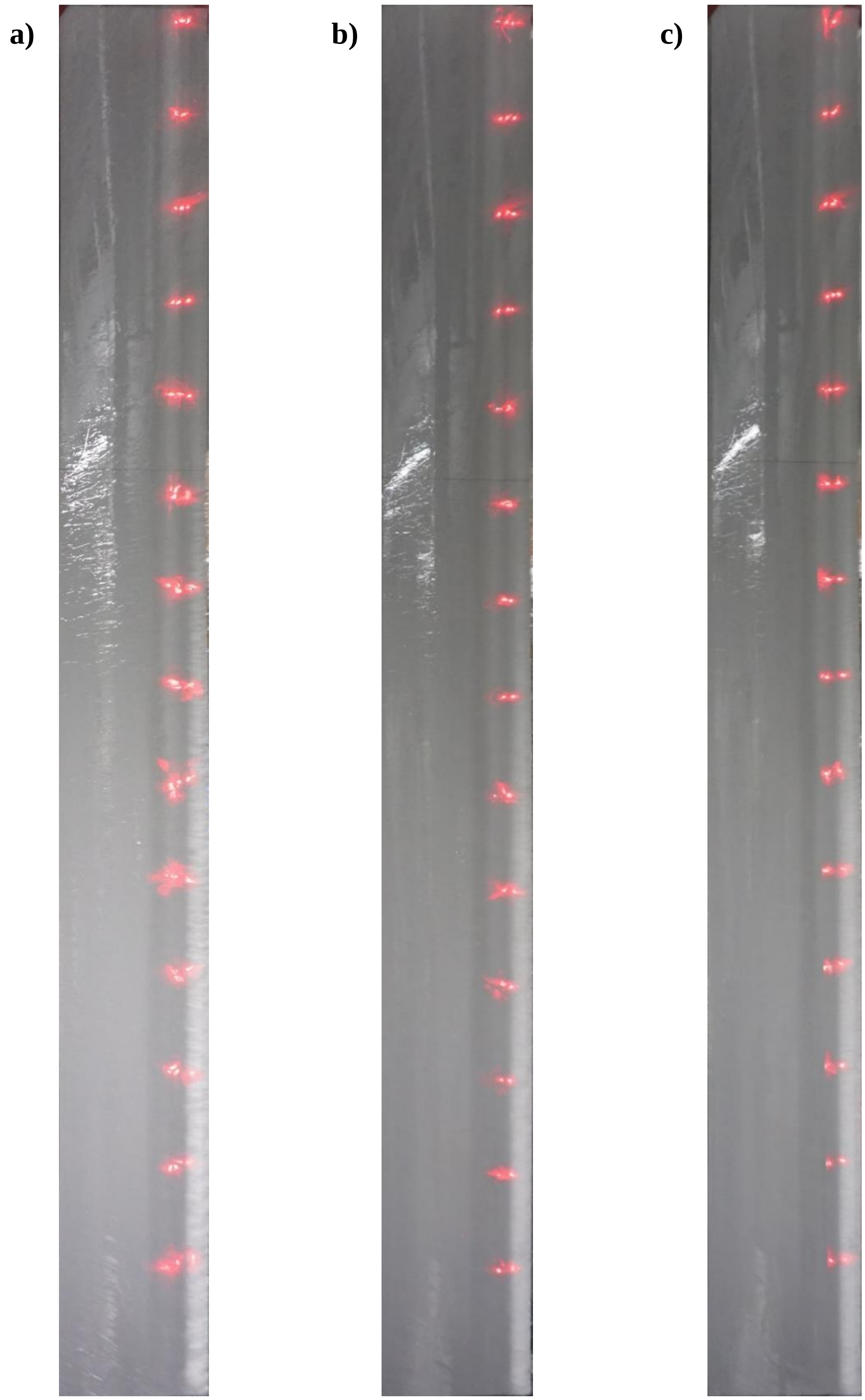

Figure 6.3. Results of the on-axis laser tests after perspective correction. The laser points were taken 5" apart vertically and 1" horizontally on a heavily worked mirror with rim angle φ = 180°. The internal bag pressure was taken at: **a)** 0.5 psi; **b)** 1 psi; and **c)** 1.5 psi.

Figure 6.4. The effect of targeting regions of severe wrinkling.

6.1.3. The effect of beam spread due to edge rays

To supplement the results of the on-axis experiment, the effect of beam spread due to edge rays was also identified. In addition to the vertical and horizontal sliding motion produced by the track, the laser itself was mounted on a rotating base, thus allowing the laser to mimic edge rays. For this experiment, the laser was restricted to moving only horizontally across the radius of the mirror. First, the laser was positioned such that an on-axis ray would target a specific point on the mirror and the target was imaged. The laser was then translated a specified distance from its initial point, but rotated by an amount equal to an incidence angle of 1° such that the laser would intercept the same point on the mirror. This would simulate the edge rays of a cone subtended by a 1° acceptance angle and therefore enable us to investigate beam spread on the target. The laser was imaged in three locations: close to the vertex of the mirror, close to the rim of the mirror, and at a point in between the two. These three locations correspond to a lateral distance of 1" apart on the track. **Figure 6.5** displays the nomenclature used for this experiment while the results of the test are given in **Figure 6.6**. The colour of the laser is changed in post-processing to easily identify each ray. The red laser corresponds to an on-axis ray, while the green and blue lasers represent rays that form a positive and negative angle with the optical axis, respectively.

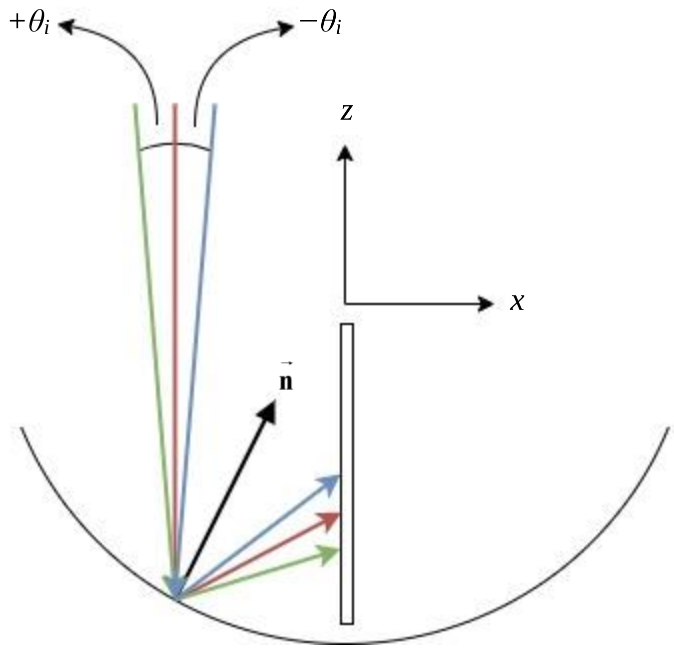

Figure 6.5. Nomenclature for the edge ray laser experiment. The red laser corresponds to the on-axis ray and the green and blue laser correspond to the rays which make a positive and negative angle with the optical axis, respectively.

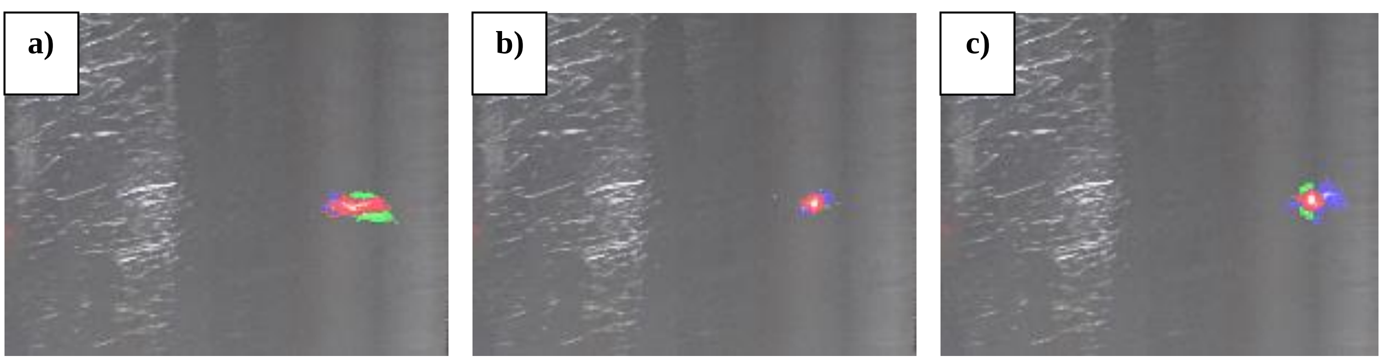

Figure 6.6. Effect of wrinkling on edge rays after perspective correction. The red laser represents the on-axis ray whereas the green and blue laser form the edge rays of a cone subtended by an acceptance angle of 1°. Each picture corresponds to a different laser location along the radius of the mirror: **a)** close to the back vertex of the mirror; **b)** in between the back vertex and the rim; and **c)** close to the rim of the mirror. The images were taken at a bag pressure equal to 1 psi.

It can be seen from **Figure 6.6 b)** that the effect of beam spread towards the middle of the mirror is almost non-existent. All three rays, despite their incidence angle, converge to nearly the same point on the target. However, the beam spread is much more pronounced towards the vertex and the rim of the mirror. Therefore, two competing effects determine the spread between an on-axis and edge ray: the distance from the mirror to the target and the reflection angle. These competing effects can be seen in **Figure 6.7**. Towards the rim, the ray travel distance from the mirror to the target is quite large and therefore the effect of incidence angle is more pronounced. Towards the vertex of the mirror however, the reflection angle is quite small, but the steep normal vector significantly spreads the reflected rays. Towards the middle however, these two effects are minimized. In addition, the overlapping rays in the centre of the mirror should not be attributed to reflection off a smooth patch of mirror; repeated testing at different locations along the length of the mirror resulted in the same outcome.

The results of this experiment are three-fold. Firstly, it investigates the effect of wrinkling in a completely controlled manner. While it would be entirely permissible to perform a comprehensive on-sun experiment to determine the concentration ratios across the target using a heavily wrinkled mirror at different pressures, we forego the need to do so by determining the correct operating pressure directly. Secondly, it decouples the on-axis rays from those incident on an angle. That is, while a certain design may be specified to accept rays within a cone subtended by the acceptance angle, using a laser separates these effects and allows us to study them individually. Finally, a method of producing discrete on-axis rays may be preferrable, as it allows for us to specifically target a wrinkle and observe its effect rather than having to interpret the results on a uniformly illuminated surface. Therefore, while this experiment is rather qualitative in nature, it provides an immense benefit in the overall optical study.

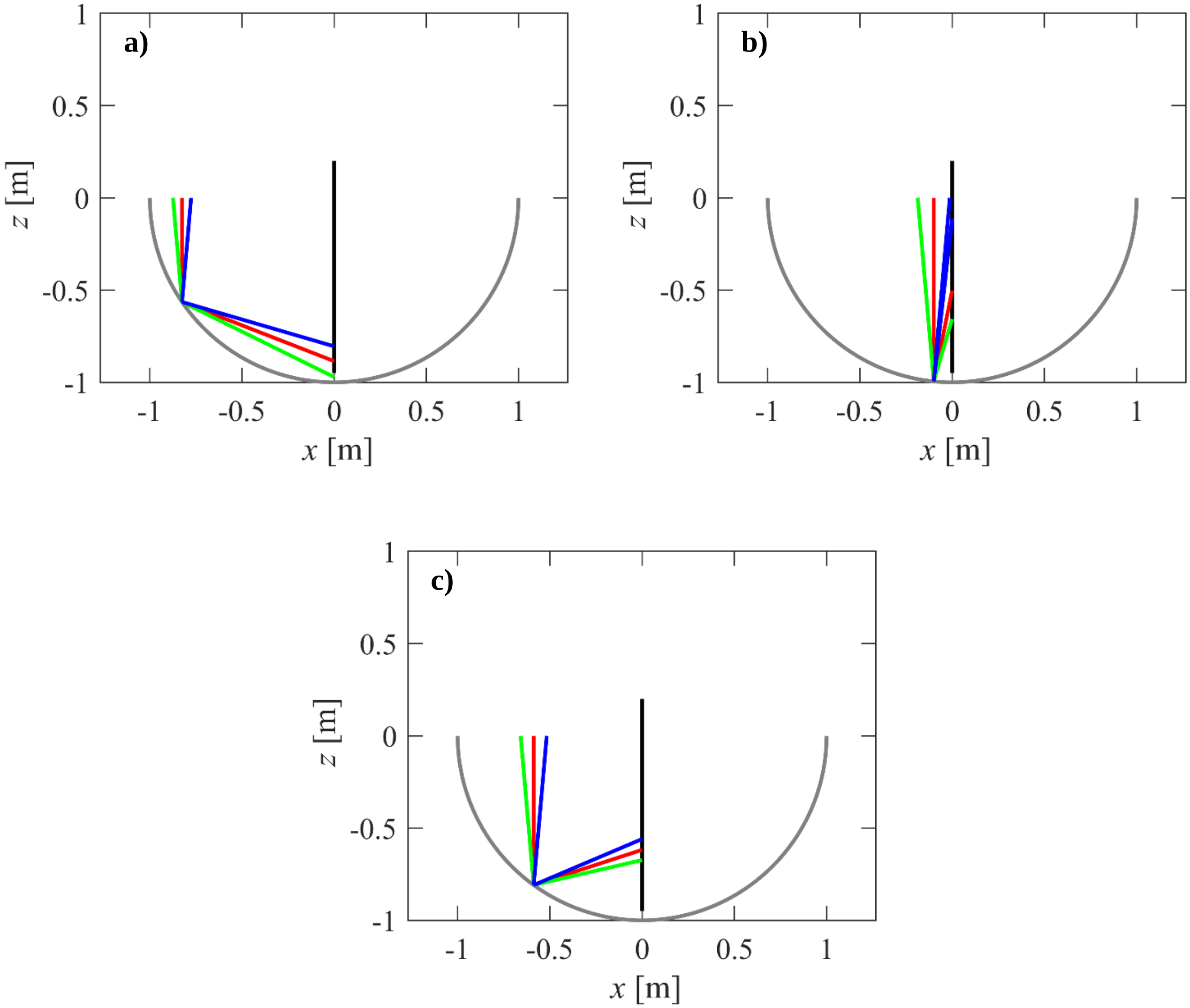

Figure 6.7. The competing effects of ray travel distance and angle of reflection on the point of intersection. **a)** and **b)** display the edge cases where the ray intercepts a point on the mirror close the rim and close to the vertex. The rim ray is largely controlled by the travel distance where the vertex ray is affected by the reflection angle. **c)** shows the minimization of the two competing effects as the ray intercepts a point in the centre of the mirror.

6.2. Flux mapping

Once the correct operating pressure of 1 psi was determined, the next step was to perform an on-sun experiment to create a flux map over the Lambertian target. The solar concentrator was deployed at ground level just south of the Bergeron Centre of Engineering Excellence (latitude 43.77°N, longitude 79.51°W, elevation 76 m). The same Sony a6000 mirrorless camera used in the laser experiment was used to image the surface of the Lambertian target and a Kipp and Zonen CHP1 pyrheliometer was used to measure the DNI throughout the experiment. The experiment was performed on October 19, 2021. The experimental set-up is shown in **Figure 6.8**.

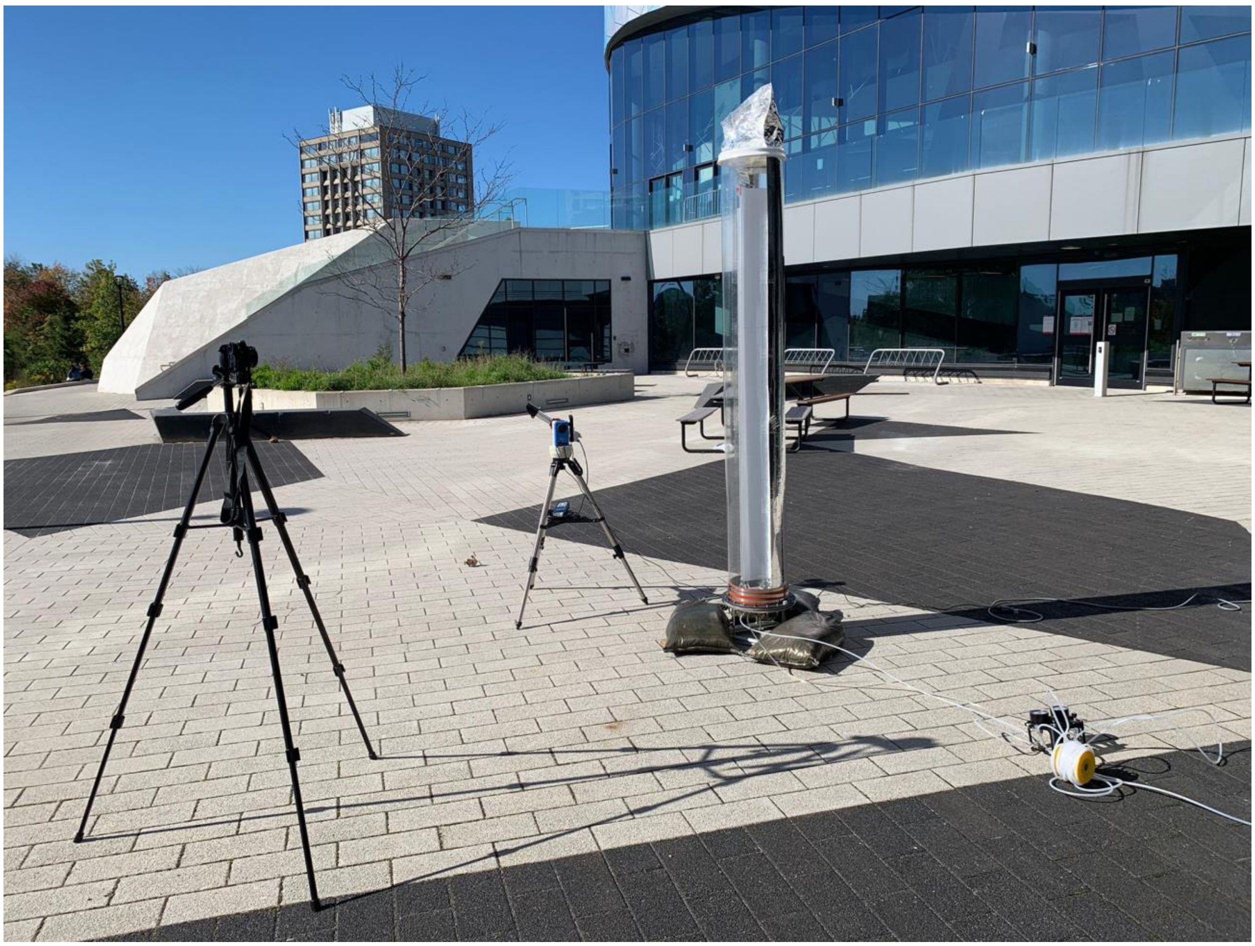

Figure 6.8. Flux mapping test set-up at ground level south of the Bergeron Centre of Engineering Excellence.

A standard operating procedure was performed each time before the Lambertian target was imaged. First, the target was directly illuminated by the sun and the surface was imaged. This image later served as a reference for which pixel intensity is converted to irradiance. Then, the concentrator was focused with respect to the sun. The base was rotated such that the target was just shadowed to ensure that the inlet aperture was perpendicular to the horizontal component of the sun vector. A full shadow indicated that the collector was rotated too far. The surface of the Lambertian target was then imaged. **Figure 6.9** shows the Lambertian target after it has been illuminated by concentrated sunlight.

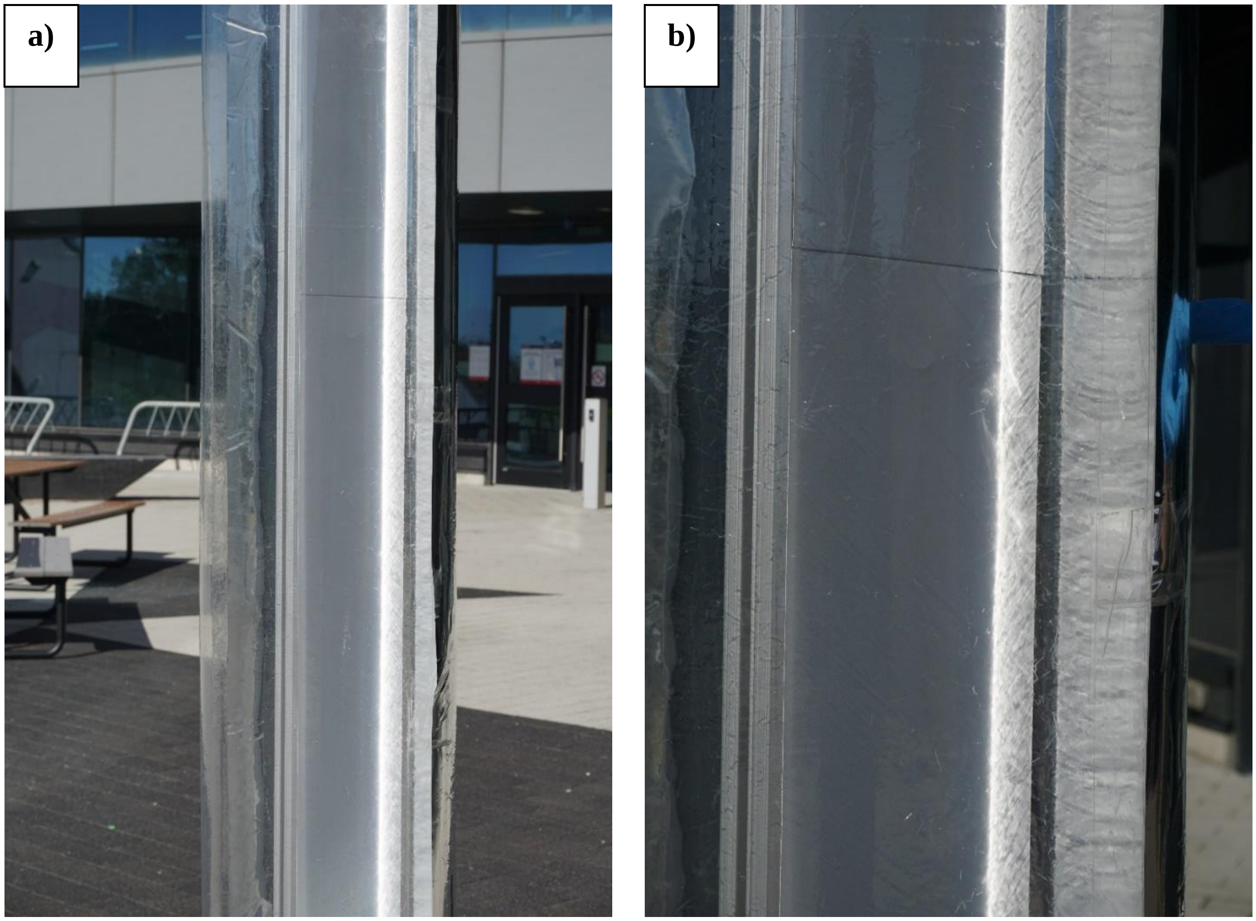

Figure 6.9. a) Lambertian target illuminated by concentrated sunlight and **b)** a close-up of the mid-region of the target. Photos were taken at 12:12:36 p.m. and 1:44:58 p.m., respectively.

A caustic can be seen towards the leading edge of the illuminated region indicating the envelope of light for a circular mirror. The effect of wrinkling can be seen in both the caustic and the region directly following it. In **Figure 6.9 b)**, some spillage is noticeable towards the midspan of the target through the presence of a flare-up off the caustic. Further, the region following the caustic is not uniformly illuminated, but rather features areas of both bright and dark spots. This can be attributed to wrinkles changing the local normal vector at the point of intersection on the mirror. However, these wrinkles may not be contributing too severely to optical losses. So long as the reflected rays are confined to a reasonably sized region, a suitably sized receiver will still capture the reflected radiation. Therefore, imaging the target during this experiment further proves that operating pressures of at least 1 psi are capable of significantly reducing the effect of wrinkles.

To create a flux map, both the reference image (image of the target directly illuminated by sunlight), the image of the focused target (image of the target when the collector is tracking the sun), and several optical quantities are processed in Matlab. First, both images are converted into grayscale such that each pixel is represented by a gray value from 0 to 1. Since we know the exact value of irradiance from the pyrheliometer, we can calculate a scaling factor which correlates gray value to pixel intensity using the following equation

$$\text{scaling factor} = \frac{\text{irradiance}}{\text{mean(gray value)}} \tag{6.1}$$

To do so, we calibrate our scaling factor using the reference image since we know the exact value of irradiance over the inlet aperture is given as DNI$\tau\rho\cos\theta$. Therefore, the scaling factor is calculated using

$$\text{scaling factor} = \frac{\text{DNI}\,\tau\rho\cos\theta}{\text{mean(gray value)}} \tag{6.2}$$

where DNI is the pyheliometer reading equal to 960 W/m^2, τ is the transmittance of the polyester equal to 0.874, ρ is the reflectance of the metallized polyester roughly equal to 0.9, and cosθ is the elevation angle at the time the images were taken equal to 60°. Essentially, multiplying the gray value at any pixel by the scaling factor returns the irradiance at that point after it has been attenuated by the transparent top sheet, mirror, and elevation angle. That is, if a pixel reads a gray value equal to 1, the scaling factor returns an irradiance equal to 377.57 W/m^2. The scaling factor is then multiplied by the gray value of each pixel in the image of the focused target to produce the flux map shown in **Figure 6.10**.

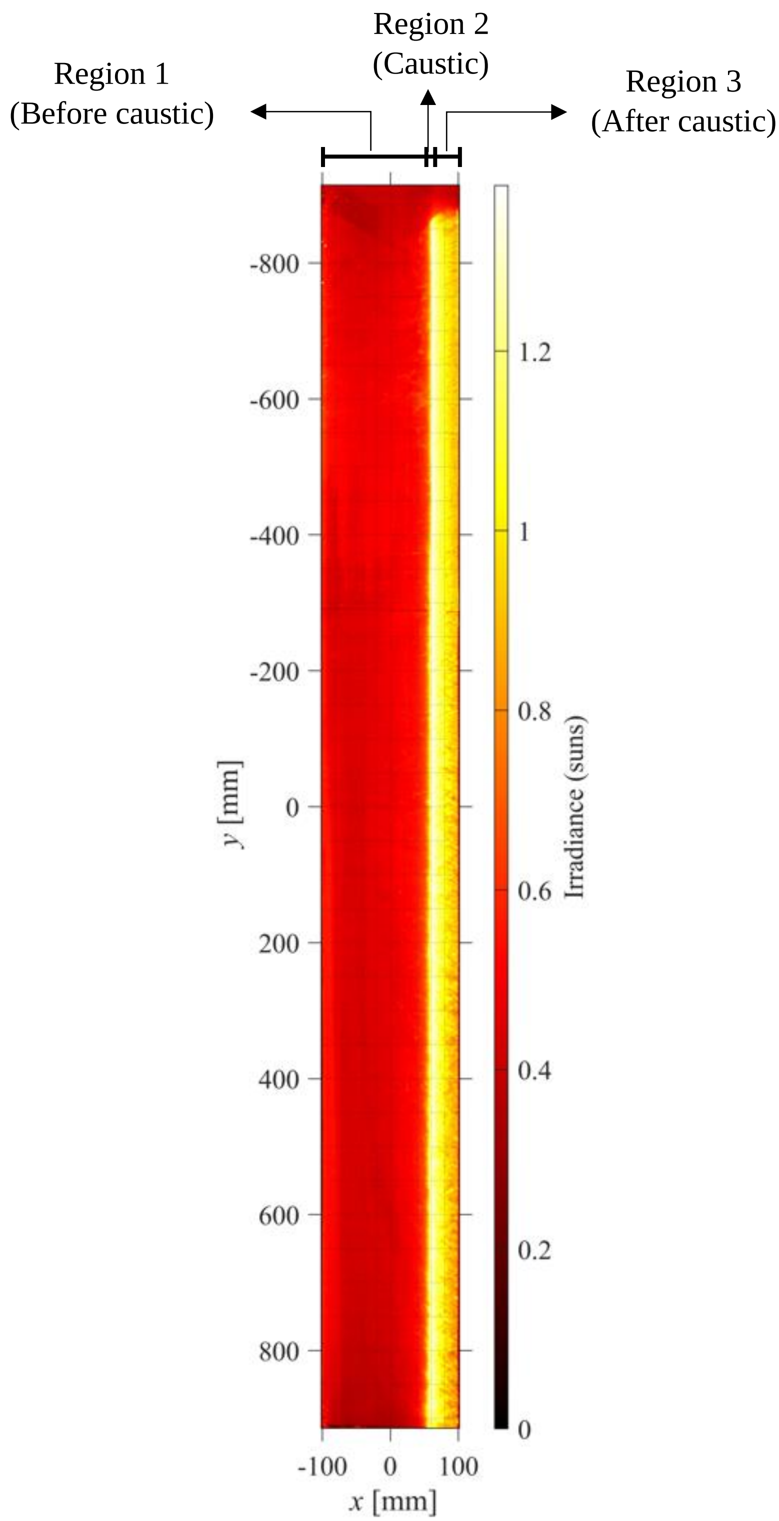

Figure 6.10. Flux map of the Lambertian target normalized by the pyrheliometer irradiance reading of 960 W/m^2 resulting in Q_{targ} = 265.5 W. The result is the concentration ratio, or suns. The artifact at the top of the illuminated region results from a shadow cast on the target due to the pail lid. The image was taken at 2:31:02 p.m.

Figure 6.10 is split into 3 regions: the region before the caustic, the caustic itself, and the region proceeding the caustic. The region before the caustic represents diffusely collected radiation and is of little importance for the final design. The caustic itself experiences the greatest recorded values of concentration equal to approximately 1.25. The flux map at the caustic further justifies the insignificant effects of wrinkling in this region. The region following the caustic experiences values of concentration in the range of 1 to 1.2. The effect of wrinkling in this region is the most prominent. As explained previously, a perfect mirror surface would result in uniform concentration for a constant value of the *x*-coordinate. Instead, certain hot spots can be seen indicating that wrinkling does cause some deviation in the reflected ray. Once again, however, so long as these rays are confined to this region, the effect of wrinkling is insignificant. **Figure 6.11** displays both the experimental and simulated flux distributions normalized to the reading of the pyrheliometer across the surface of the target. The simulated flux distributions were developed in VeGaS by assuming various surface errors (in mrad) to validate the experimental results.

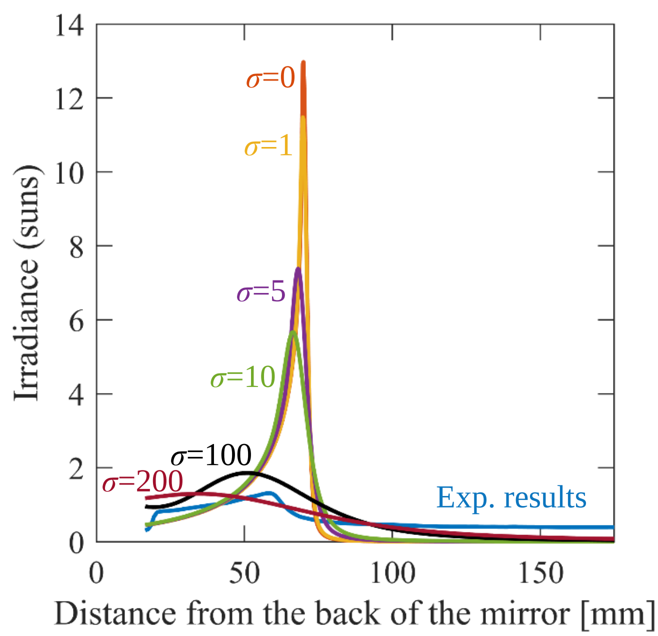

Figure 6.11. Experimental and simulated distribution of the concentration ratio across the target plane. The simulation uses 10^9 rays and all error values are given in milliradians.

According to Bader et al. typical values of mirror surface error are around 2.5 mrad [9]. Then, according to **Figure 6.11**, the simulated results bound the experimental results at very large (and perhaps unrealistic) values of the surface error of around 100-200 mrad. Potential reasons for the discrepancy between the simulated and experimental results include, but are not limited to:

misplacement of the Lambertian target within the collector, alignment error within the fabrication process of the outer-envelope, tracking error, and/or the outer-envelope not inflating perfectly vertical resulting in some curvature within the mirror. Nevertheless, the final average value of concentration can be extracted from **Figure 6.11** by averaging over those values greater than 1. The final value of concentration is equal to 2.3 (doubled to consider a two-sided receiver).

6.2.1. Flux mapping validation

While flux mapping provides useful information with respect to optical analysis and receiver design, the technique is not without error. Therefore, it becomes important to quantify this error to justify the results presented here. To do so, we utilize a numerical integration technique to find the total heat incident on the Lambertian target in the flux map and compare it to the heat entering through the inlet aperture. The latter (Q_{in}) is found by attenuating the pyrheliometer irradiance reading by the transmittance of the top sheet, reflectance of the mirror, and the cosine of the elevation angle and multiplying the result by one-half the inlet aperture since the experiment is one sided. Simply put, Q_{in} is found using

$$Q_{\mathrm{in}} = q_{\mathrm{pyr}} \tau \rho \cos\theta \left(\tfrac{1}{2} L_{AP} W_{AP} \right) \tag{6.3}$$

The flux map on the other hand is essentially a measure of the heat flux per pixel. Since the physical dimensions of the target are known, the size of a pixel can be converted to physical space using the following equation

$$\text{pixel size} = \frac{L_{AP} W_{AP}}{\#\,\text{of pixels}} \tag{6.4}$$

We can then multiply the irradiance value at each pixel by the pixel size and sum the result to find the overall power incident on the target. Doing so yields a Q_{in} and a Q_{exp} of 99.77 W and 105.41 W, respectively, thus resulting in a difference of 5.4% and verifying the experiment.

6.3. Outdoor thermal tests

To culminate the proof of concept of the all-inflated vertically oriented solar collector, a thermal prototype was deployed on the roof of the Bergeron Centre of Engineering Excellence (latitude 43.77°N, longitude 79.51°W, elevation 92.7 m) on April 22, 2022 as shown in **Figure 6.12**. The experiment used the same Kipp and Zonen CHP1 pyrheliometer to measure the DNI over the course of the experiment. The solar collector tracked the sun manually over the course of 5 hours. The experiment was split into two phases. During the first phase the flow rate inside the receiver was set to 1 scfm and later increased to 1.3 scfm during the second phase. The measured values of the thermal experiment are shown in **Figure 6.13**. Superimposed on **Figure 6.13** are the inlet and outlet temperatures generated by the simulation in *Section 5*.4. The right y-axis is representative of the portion of the DNI that contributes to heating the receiver, where cosϑ represents the cosine losses due to elevation angle. The sharp vertical lines in the data representing the projected irradiance are a result of clouds passing in front of the sun. In the second phase of the experiment, the conditions of the sky were particularly hazy with clouds passing in front of the sun more frequently than in the first phase of the experiment. A summary of the operating conditions are given in **Table 6.1**. Recording began as soon as the temperatures reached steady state. Furthermore, **Figure 6.14** shows the experimental and simulated power output and efficiency calculated using the definitions provided in *Section 5.3* reiterated here for convenience[13]

$$Q_{\text{out}} = \dot{m}c_p\left(T_{\text{out}} - T_{\text{in}}\right) \tag{6.5}$$

$$\eta = \frac{Q_{\text{out}}}{Q_{\text{in}}} = \frac{\dot{m}c_p\left(T_{\text{out}} - T_{\text{in}}\right)}{\text{DNI}\cos\theta A_{\text{in}}} \tag{6.6}$$

In the efficiency calculations for the experimental results, Q_{out} is time averaged over a period of 20 minutes to compensate for the sudden drops in projected irradiance. If this is foregone, efficiency values of over 100% can be observed as an artifact of the calculation. Essentially, Q_{in} decreases due to clouds while Q_{out} is held almost constant as the HTF does not have a sufficient amount of time to cool down.

---

[13] In Eq. (6.5) and Eq. (6.6) the nomenclature is slightly different from that of *Section 5.3*. Q_{gain} has been replaced by Q_{out}, but for all intents and purposes the two are equal.

Figure 6.12. Thermal experiment set-up on the roof of the Bergeron Centre of Engineering Excellence (latitude 43.77°N, longitude 79.51°W, elevation 92.7 m) on April 22, 2022.

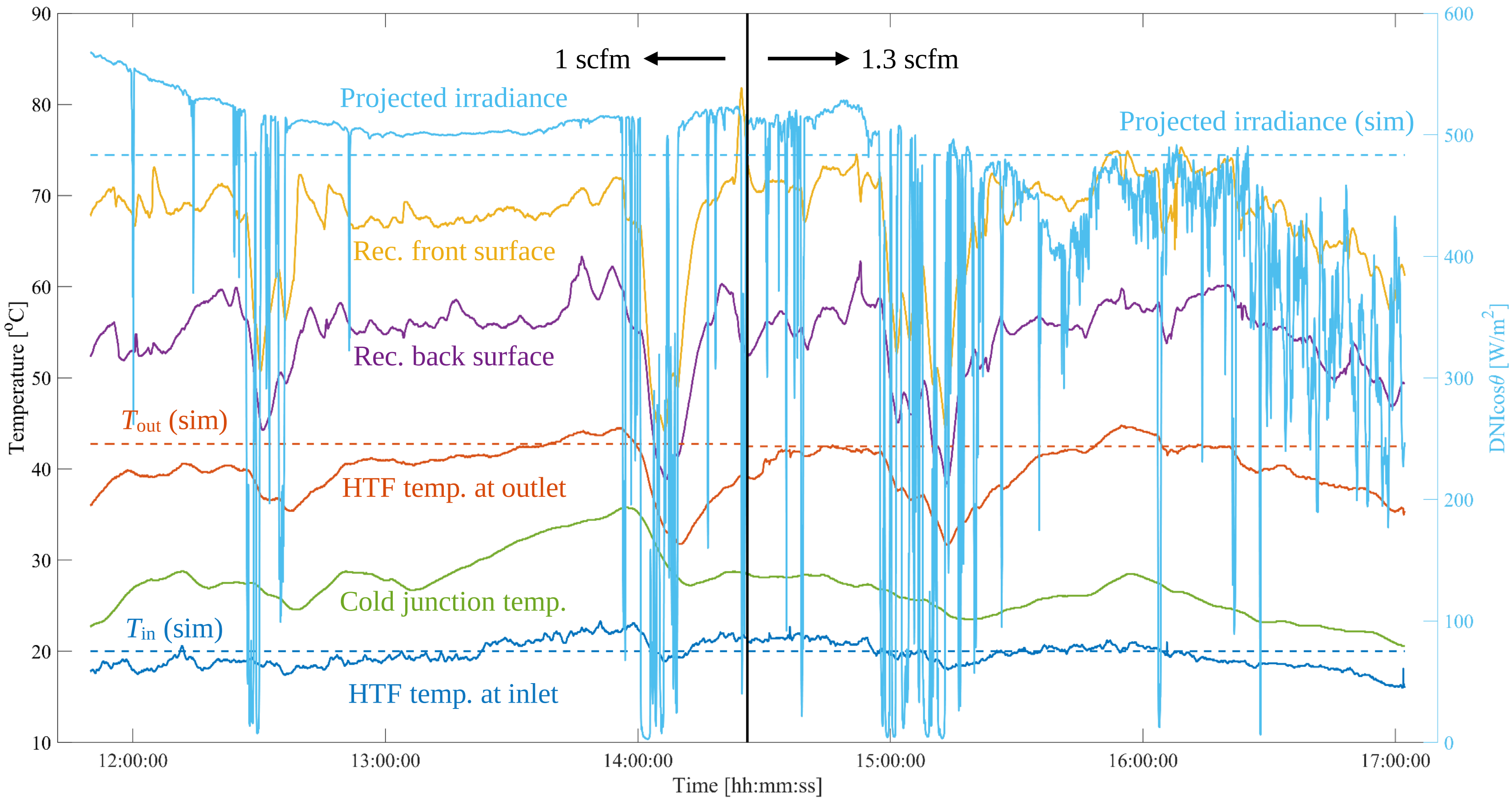

Figure 6.13. Results of the final thermal experiment. The vertical line separates the two phases of the experiment where the flow rate was changed. The dashed lines represent the simulated values for the irradiance and inlet and outlet temperatures which are approximately 483.5 W/m^2, 20°C, and 42.5°C, respectively. The projected irradiance is the irradiance entering the inlet aperture, while the irradiance on the receiver will be larger by $\eta_{opt}C_g$ (without considering losses in the top-sheet, mirror, or receiver).

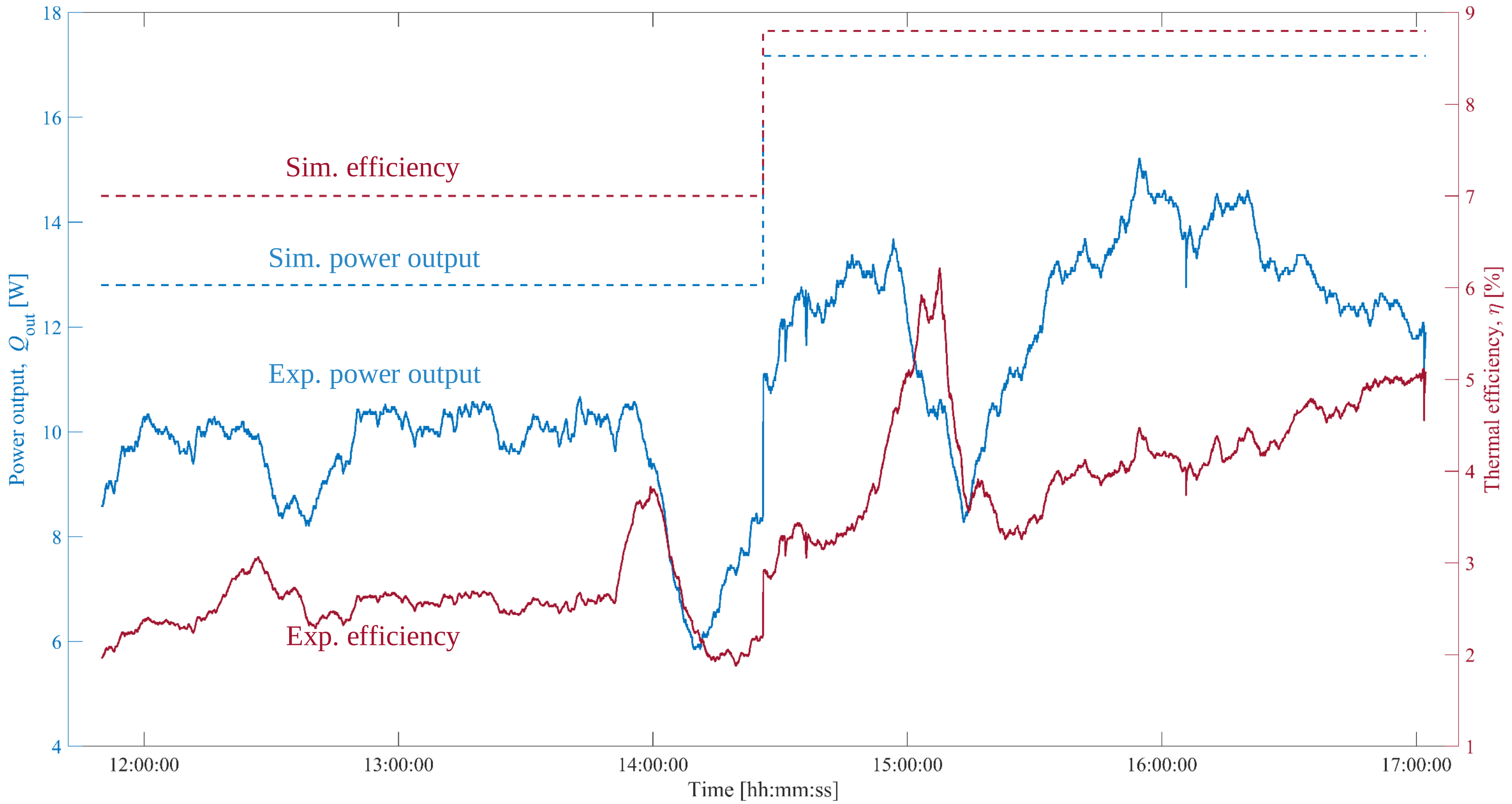

Figure 6.14. Power output and efficiency calculated from the results of the final thermal experiment. The dashed lines represent the simulated values.

Table 6.1. Summary of the operating conditions over the two phases of the final thermal experiment.

	Phase 1 – *1 scfm*	**Phase 2 – *1.3 scfm***
Inlet temperature (°C)	19.8	19.6
Outlet temperature (°C)	39.7	40.0
Front surface temperature (°C)	66.8	67.6
Back surface temperature (°C)	54.9	54.3
Average power output (W)	9.4	12.6
Simulated power output (W)	12.8	17.2
Average efficiency (%)	2.6	4.2
Simulated efficiency (%)	7.0	8.8
Average elevation angle (°)	57.4	45.2

The results from the thermal experiment in **Figure 6.13** and **Figure 6.14** agree reasonably well with the thermal simulation. However, caution must be employed when comparing the results as the simulation uses steady state conditions whereas the experiment is transient in nature. Without modelling the thermal capacitance of the receiver tube, the changing values of projected irradiance cannot be captured and will therefore produce a discrepancy between simulated values and those determined experimentally. We can, however, obtain an idea of the steady state conditions by examining the period of time from 13:00:00 to 14:00:00 where the projected irradiance is relatively constant. Within this period of time, the experimentally obtained output temperature shown in **Figure 6.13** is approximately 40°C, whereas for the same conditions the simulation predicts a slightly greater value of approximately 43°C. Similarly, the experimentally obtained power output during this period is approximately equal to 10 W, with the simulated value equaling 12.8 W. The efficiency displays the largest difference between the experimentally obtained and simulated value. However, it must be remembered that the efficiency changes depending on the time period over which the moving average is taken. Other discrepancies in the experimentally obtained and simulated values include, but are not limited to: shape error in the bag, wrinkles in the mirror, misalignment during tracking, or thermal losses in the inflation sub-assembly. Interestingly, however, the thermal capacitance of the receiver can be empirically determined from **Figure 6.13**. For example, consider the time period from 12:20:00 to 12:40:00

where the sun was blocked by incoming clouds thus reducing the projected irradiance significantly. While the surface temperature of the receiver responded quite quickly and decreased over 15°C, the heat transfer fluid only dropped 5°C. This same trend can be observed from 13:55:00 to 14:10:00 and from 15:00:00 to 15:20:00. This indicates that the receiver has a large heat capacitance and is capable of heating the heat transfer fluid even during periods of lower projected irradiance. This can be both a benefit and a detriment to the system. While a heated receiver will continue to heat the heat transfer fluid during periods of lower projected irradiance, a cold receiver will need to be directly illuminated for some time to be brought up in temperature. Finally, the surface thermocouples in both phases of the experiment depict the same trend – the back of the receiver is approximately 10°C colder than the front of the receiver. This is to be expected as the back of the receiver absorbs very little radiation compared to the front of the receiver closer to the caustic, as shown by **Figure 6.15**.

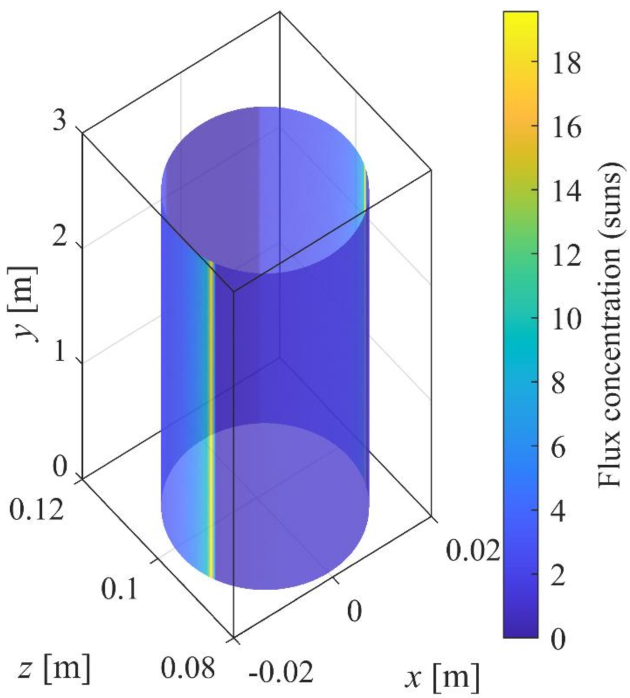

Figure 6.15. Flux distribution over the surface of the receiver. Greater values of the *y*-coordinate indicate the side closest to the mirror.

Chapter 7

Future design considerations

The all-inflated vertically oriented solar trough concentrator has been realized as a low-cost, simple alternative to its horizontal counterpart. However, there is much left to be optimized with respect to its thermal performance. This chapter is dedicated to discussing future design considerations to increase the maximum output temperature and solidify the vertical solar collector as a real alternative to low-cost, renewable energy.

7.1. Mitigating thermal losses

The main factor preventing the vertical collector presented here from being realized as a robust alternative in its current state is its extremely low efficiency. While achieving a ΔT of around 20°C is a step in the right direction, a thermal efficiency of 7% is limiting the output to much lower values than are achievable. Therefore, in order to increase the operating efficiency, both the convection and radiative losses must be supressed to increase Q_{gain}.

In the current state, 54% of the incident heat is being lost by convection. As aforementioned, since the air on the inside of the bag is stationary, the convective losses must be due to natural convection. In order to supress natural convection, an inflated heat shield may be added around the receiver which restricts convection currents from forming. In fact, if the space between the receiver and the heat shield is made sufficiently small such that the Rayleigh number is below that of the critical value, fluid motion can be prevented altogether. This forces heat transfer to occur by conduction rather than convection. Therefore, the air in the space between the heat shield and the receiver acts as a low-*k* cushion to prevent losses. The heat shield may be made of any tubular material with high transmittance values such that it does not prevent thermal radiation from reaching the receiver, such as FEP or ETFE, assuming that neither of these materials yield under pressure.

In the current work, one thermal experiment was attempted with a heat shield made of FEP installed around the receiver. The heat shield was manufactured as a sheet and formed into a tube by taping the seams together. The nominal diameter of the heat shield was 1.8". The heat shield was supplied air through a bleed hole made within the pipe nipple that supports the receiver. That is, the heat shield was inflated with air after it had been heated. During the experiment, however, the tape along the heat shield failed numerous times. The seam would frequently open and create a path for the heated air to flow into the chamber of the main bag. The outcome of this experiment provides two main takeaways for the future design considerations of a vertical collector. Firstly, the method of binding the heat shield must be capable of withstanding the internal pressure of the receiver. Ideally, the heat shield would come manufactured as a tube to prevent failure of the seal altogether. Secondly, the heat shield should be inflated through a separate line. This will allow us to individually control the pressure of the receiver and heat shield and to isolate the two flow paths.

Supressing radiation is a much more difficult feat to achieve. Radiative losses are inherent to the material being used for the receiver, and at higher temperatures, radiative losses become increasingly more prominent. As aforementioned in *Section 3.4*, solar selective coatings are not easily applied to thin film polymers by spraying or brushing like they are on rigid receivers. Therefore, there are two approaches to supressing radiation. Firstly, a further investigation into the absorption to emission ratio of thin film polymer membranes can be conducted in search of a polymer that inherently displays solar selectivity. Secondly, alternative methods of applying solar selective coatings can be explored such as polymer electroplating. Nevertheless, the thermal Simulink simulation was tweaked to explore the effects of supressing losses. In the following simulation, it was assumed that the critical Rayleigh's number was not achieved, and thus losses are convective and not conductive. This is because the critical Rayleigh's number may result in a characteristic thickness that is impractical to produce. Instead, the convective heat transfer coefficient was set to 2 W/m^2K. The absorptance of the receiver was maintained at 0.9, however the emittance was reduced to 0.2. **Figure 7.1 – 7.4** present the simulation results with reduced losses.

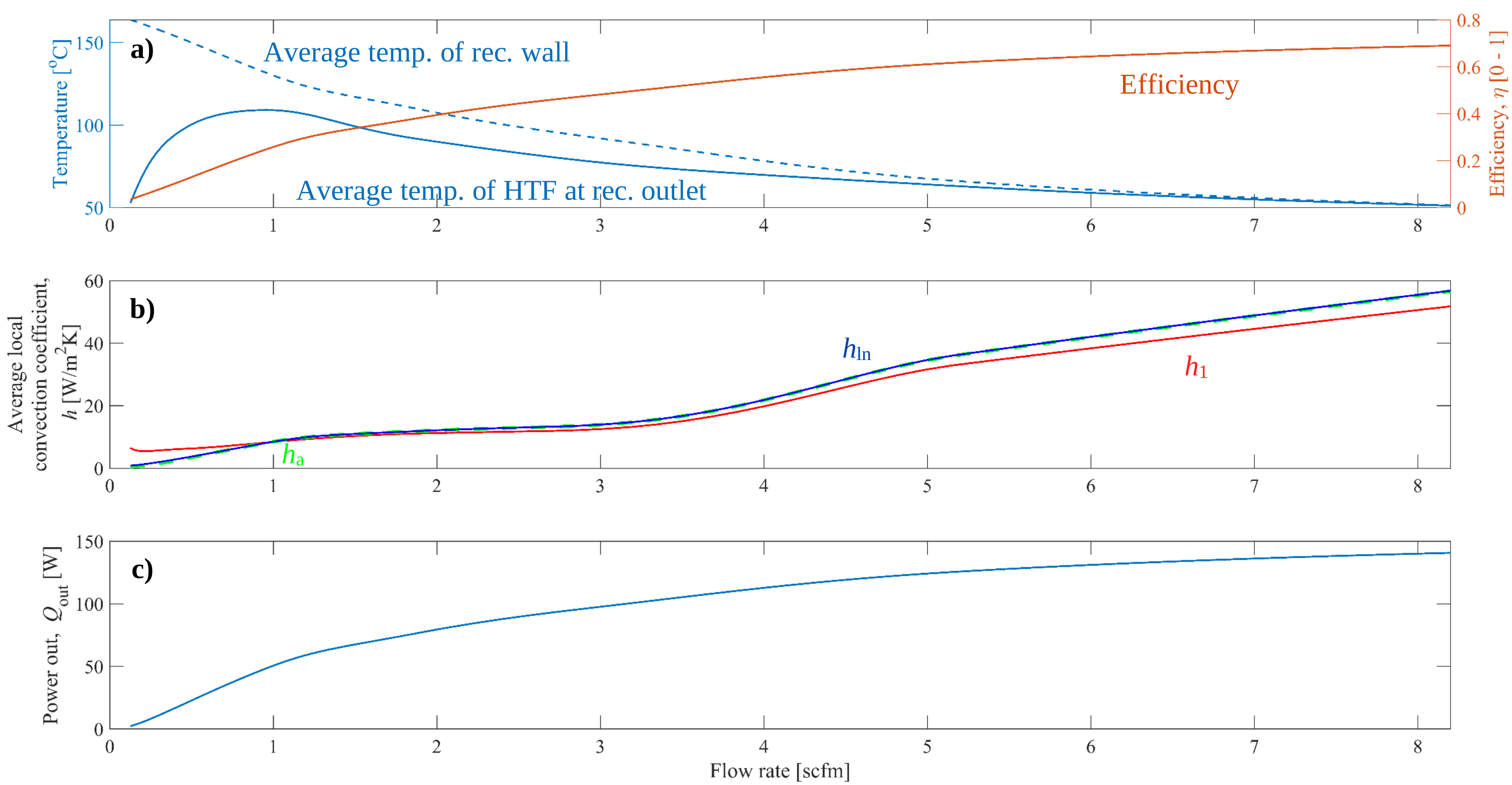

Figure 7.1. Results of thermal simulation with reduced losses showing the effect of changing flow rate on: **a)** outlet fluid temperature, wall temperature, and efficiency; **b)** average local heat transfer coefficients h_1, h_a, and h_{ln} (h_a is represented visually by the dashed green line); and **c)** the power output in W.

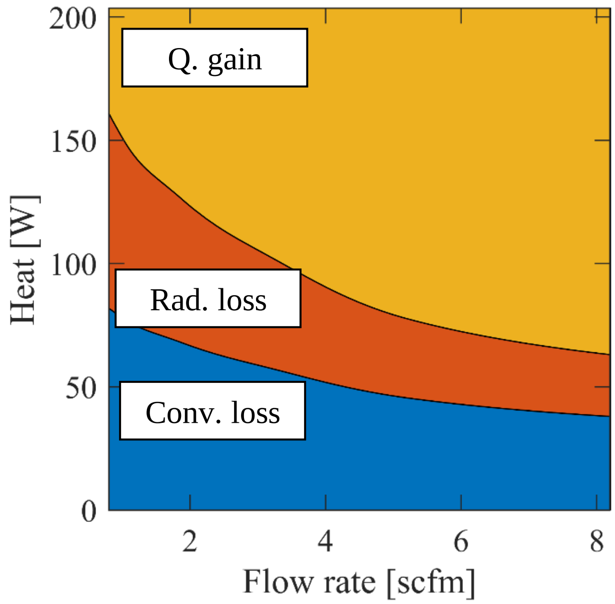

Figure 7.2. Dependence of Q_{gain} and Q_{loss} on flow rate with reduced convective and radiative losses.

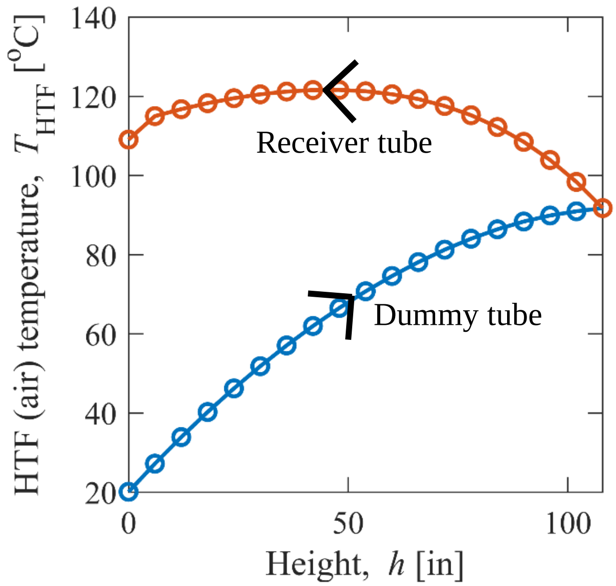

Figure 7.3. Evolution of air temperature throughout the concentric receiver at 1 scfm with reduced losses. The arrows represent the flow direction.

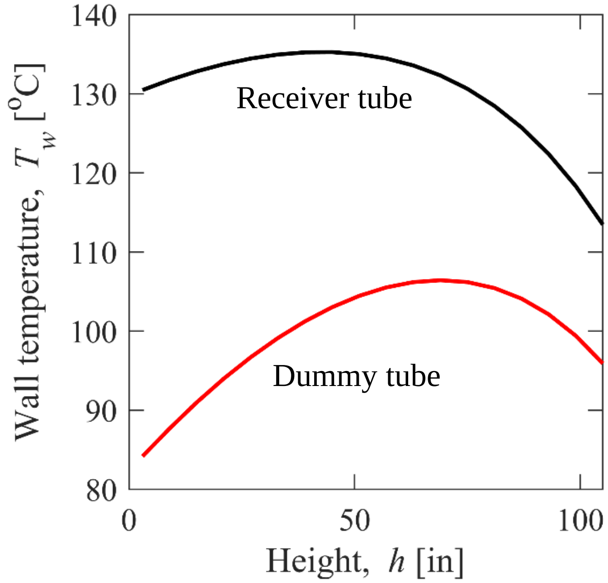

Figure 7.4. Evolution of the wall temperature across the concentric receiver with reduced losses.

The main result of the preceding simulation is **Figure 7.2** which displays the losses and gains of the system. By reducing the convection coefficient to 2 W/m^2K, the convective losses at 1 scfm reduce to approximately 77 W, or 37.8% of the total heat input. This corresponds to a 29% decrease in convective losses from the previous case. Subsequently, by reducing the value of emittance to 0.2, the radiative losses at 1 scfm reduces to approximately 73 W, or 35.9% of the total heat input. This corresponds to a 5.1% decrease in radiative losses from the previous case. Careful consideration must be given when comparing the radiative losses of the two systems, however, since emission is proportional to the fourth power of the absolute temperature. Therefore, it is not surprising that the reduction in radiative losses is not as significant as the reduction in convective losses, as the receiver is operating at a higher overall temperature. In fact, the implication behind any reduction in radiative losses is quite substantial. Then, from **Figure 7.1** it can be seen that for an equivalent flow rate of 1 scfm, the average outlet temperature of the heat transfer fluid is 109°C the efficiency increases to 25.8%, and the power output increases to 50.5 W. Interestingly, the peak outlet temperature shifts to marginally smaller values of flow rate when the efficiency is increased.

7.2. Reducing leakage

One recurring problem that took place across all thermal prototypes was leakage within the bag. Whilst a standard operating procedure for constructing the bag was created, the method was not immune to error. Taping the seams of the bag, for example, was especially susceptible to human error resulting in leak pathways if not performed perfectly. While part of the process involves eliminating the leak pathways within the seam, they are not always visible and only become apparent after inflation. During experimentation, these leaks were fixed simply with an overlapping piece of tape. Once the leak has propagated across the main seam, however, it becomes nearly impossible to prevent a leak from occurring elsewhere. Therefore, a single impulse weld along each seam is proposed to reduce the chances of a leak forming. More importantly, however, careful consideration needs to be given to sealing the top of the bag. The half-round method used in the current works performed well, but the method should be refined to eliminate leaks altogether. In the current method, the half rounds are lined with butyl rubber cut from the same tube as the receiver, except for the region where the receiver itself is being clamped. This is to match the thickness of the receiver to create a uniform clamping pressure. This method, however, will always leave a leak path at the point where the rubber strip meets the receiver tube. Instead, it may be possible to weld these materials together once assembled to create a barrier against leaks. Additionally, in future iterations the half-rounds should be machined from aluminum stock rather than acrylic. This will provide an even and much greater clamping force.

7.3. Final considerations

The final considerations that should be made for future iterations begins with fully implementing a furling and tracking system. While several methods of furling were tested and evaluated based on their pros and cons, further investigation is required before realizing a completely and autonomously deployable system. If utilizing the tape spring method, it should be physically constrained to the spine of the bag such that any lateral motion and buckling is prevented. If utilizing the pulley and winch method, appropriate motors and control systems should be implemented to autonomously deploy the system. Additionally, the electromechanical system required for tracking has been developed in theory, however, it was foregone to prioritize a complete thermal analysis. In future iterations of the vertical collector, the electromechanical system should be developed to properly track the sun and, as a result, eliminate any human errors introduced in the thermal analysis from manual tracking. Finally, while the current design is meant to standalone, when the thermal losses are mitigated, a potential avenue for utilizing multiple solar collectors in an array should be investigated.

References

[1] bp, "Stastical Review of World Energy," *bp*, 2021.

[2] International Energy Agency, "World Energy Outlook 2021," Paris, 2021.

[3] International Energy Agency, "Global Energy Review - Assessing the effects of economic recoveries on global energy demand and CO2 emissions in 2021," 2021.

[4] T. A. Cooper, A. Steinfeld, and M. Collares Pereira, "High-concentration solar trough collectors and their application to concentrating photovoltaics," ETH-Zürich, 2014. doi: 10.3929/ethz-a-010216611.

[5] P. D. Tagle-Salazar, K. D. P. Nigam, and C. I. Rivera-Solorio, "Parabolic trough solar collectors: A general overview of technology, industrial applications, energy market, modeling, and standards," *Green Process. Synth.*, vol. 9, no. 1, pp. 595–649, 2020, doi: doi:10.1515/gps-2020-0059.

[6] Y. L. He *et al.*, "Perspective of concentrating solar power," *Energy*, vol. 198, p. 117373, May 2020, doi: 10.1016/J.ENERGY.2020.117373.

[7] R. Bader, P. Haueter, A. Pedretti, and A. Steinfeld, "Optical Design of a Novel Two-Stage Solar Trough Concentrator Based on Pneumatic Polymeric Structures," *J. Sol. Energy Eng.*, vol. 131, no. 3, Jun. 2009, doi: 10.1115/1.3142824.

[8] R. Pitz-Paal *et al.*, "Development Steps for Parabolic Trough Solar Power Technologies With Maximum Impact on Cost Reduction," *J. Sol. Energy Eng.*, vol. 129, pp. 371–377, Nov. 2007, doi: 10.1115/1.2769697.

[9] R. Bader, A. Pedretti, and A. Steinfeld, "A 9-m-Aperture Solar Parabolic Trough Concentrator Based on a Multilayer Polymer Mirror Membrane Mounted on a Concrete Structure," *J. Sol. Energy Eng.*, vol. 133, no. 3, Jul. 2011, doi: 10.1115/1.4004353.

[10] P. Good, G. Ambrosetti, A. Pedretti, and A. Steinfeld, “A 1.2 MWth solar parabolic trough system based on air as heat transfer fluid at 500 °C — Engineering design, modelling, construction, and testing,” *Sol. Energy*, vol. 139, pp. 398–411, Dec. 2016, doi: 10.1016/J.SOLENER.2016.10.002.

[11] H. Tabor and H. Zeimer, “Low-cost focussing collector for solar power units,” *Sol. Energy*, vol. 6, no. 2, pp. 55–59, Apr. 1962, doi: 10.1016/0038-092X(62)90004-X.

[12] F. M. I. De Los Santos-García, Y. Nahmad-Molinari, J. Nieto-Navarro, C. Alanís-Ruiz, and F. Patiño-Jiménez, “Construction and Testing of Lightweight and Low-Cost Pneumatically Inflated Solar Concentrators,” *Int. J. Photoenergy*, vol. 2016, p. 2758546, 2016, doi: 10.1155/2016/2758546.

[13] T. Cooper, G. Ambrosetti, A. Pedretti, and A. Steinfeld, “Surpassing the 2D Limit: A 600x High-concentration PV Collector Based on a Parabolic trough with Tracking Secondary Optics,” *Energy Procedia*, vol. 57, pp. 285–290, 2014, doi: https://doi.org/10.1016/j.egypro.2014.10.033.

[14] T. Cooper, M. Schmitz, P. Good, G. Ambrosetti, A. Pedretti, and A. Steinfeld, “Nonparabolic solar concentrators matching the parabola,” *Opt. Lett.*, vol. 39, no. 15, pp. 4301–4304, 2014, doi: 10.1364/OL.39.004301.

[15] P. Kurup, S. Glynn, and S. Akar, “Manufacturing Cost Analysis of Advanced Parabolic Trough Collector: Preprint,” Golden, CO, 2021.

[16] P. Kurup, S. Akar, S. Glynn, C. Augustine, and P. Davenport, “Cost Update: Commercial and Advanced Heliostat Collectors,” 2022.

[17] L. Li, B. Wang, R. Bader, T. Cooper, and W. Lipiński, “Concentrating collector systems for solar thermal and thermochemical applications,” *Adv. Chem. Eng. Sol. Thermochem.*, vol. 58, 2021.

[18] J. Chaves, *Introduction to Nonimaging Optics*, Second. Taylor & Francis Group, LLC, 2016.

[19] M. Timpano and T. A. Cooper, “Concentration ratio for a circular trough with flat receiver,” *arXiv:2206.08244 [physics.optics]*, 2022.

[20] H. Tabor, “Stationary mirror systems for solar collectors,” *Sol. Energy*, vol. 2, no. 3, pp. 27–33, 1958, doi: https://doi.org/10.1016/0038-092X(58)90051-3.

[21] A. Rabl, “Comparison of solar concentrators,” *Sol. Energy*, vol. 18, no. 2, pp. 93–111, Jan. 1976, doi: 10.1016/0038-092X(76)90043-8.

[22] D. A. Harper, R. H. Hildebrand, R. Stiening, and R. Winston, “Heat trap: an optimized far infrared field optics system,” *Appl. Opt.*, vol. 15, no. 1, pp. 53–60, 1976, doi: 10.1364/AO.15.000053.

[23] R. Winston, J. C. Minano, P. G. Benitez, N. Shatz, and J. C. Bortz, *Nonimaging Optics*. Burlington, M.A.: Academic Press, 2005.

[24] D. Buie, A. G. Monger, and C. J. Dey, “Sunshape distributions for terrestrial solar simulations,” *Sol. Energy*, vol. 74, no. 2, pp. 113–122, Feb. 2003, doi: 10.1016/S0038-092X(03)00125-7.

[25] P. Bendt and A. Rabl, “Optical analysis of point focus parabolic radiation concentrators,” *Appl. Opt.*, vol. 20, no. 4, pp. 674–683, 1981, doi: 10.1364/AO.20.000674.

[26] Z. H. Zhu and B. M. Quine, “Experimental Investigation of Inflatable Cylindrical Cantilevered Beams,” *Solids Struct.*, 2008.

[27] J. R. Leonard, G. Brooks, and H. G. Mccomb, “Structural Considerations of Inflatable Reentry Vehicles,” *NASA*, no. TN D-457, Sep. 1960.

[28] R. L. Comer and S. Levy, “Deflections of an Inflated Circular-Cylindrical Cantilever Beam,” *AIAA J.*, vol. 1, no. 7, pp. 1652–1655, Jul. 1963, doi: 10.2514/3.1873.

[29] J. A. Main, S. W. Peterson, and A. M. Strauss, “Load-Deflection Behavior of Space-Based Inflatable Fabric Beams,” *J. Aerosp. Eng.*, vol. 7, no. 2, pp. 225–238, Apr. 1994, doi: 10.1061/(ASCE)0893-1321(1994)7:2(225).

[30] H. Stein and J. Hedgepeth, "Analysis of Partly Wrinkled Members," *NASA*, no. TN D-813, 1961.

[31] J. A. Main, S. W. Peterson, and A. S. Strauss, "Beam-Type Bending of Space-Based Inflated Membrane Structures," *J. Aerosp. Eng.*, vol. 8, no. 2, pp. 120–125, Apr. 1995, doi: 10.1061/(ASCE)0893-1321(1995)8:2(120).

[32] R. Hibbeler, *Mechanics of Materials*, Ninth. Upper Saddle River: Pearson Prentice Hall, 2014.

[33] Y. A. Cengel and D. J. M. Cimbala, *Fluid Mechanics - Fundamentals and Applications*, Fourth. New York: McGraw-Hill Education, 2018.

[34] Y. A. Cengel and A. J. Ghajar, *Heat and Mass Transfer*, Fifth. McGraw-Hill Education, 2015.

[35] J. M. Buchlin, "Natural and forced convective heat transfer on slender cylinders," *Rev. Générale Therm.*, vol. 37, no. 8, pp. 653–660, Sep. 1998, doi: 10.1016/S0035-3159(98)80043-3.

[36] R. Byron Bird, W. E. Stewart, and E. N. Lightfoot, *Transport Phenomena*, Revised Second. John Wiley & Sons, 2007.

List of publications

M. Timpano, T. Cooper, "Concentration ratio for a circular trough with flat receiver," submitted June 2022 to *Solar Energy*, under review.

M. Timpano, T. Cooper, "Nonimaging behavior of circular trough concentrators with tubular receivers," submitted July 2022 to *Solar Energy Engineering*, under review.

Appendix A

Bag construction process (visual)

The following section is intended to accompany the procedure for developing the outer envelope (bag) laid out in *Section 3.2.2*. Each step is accompanied by an image to facilitate visual understanding.

Step 1

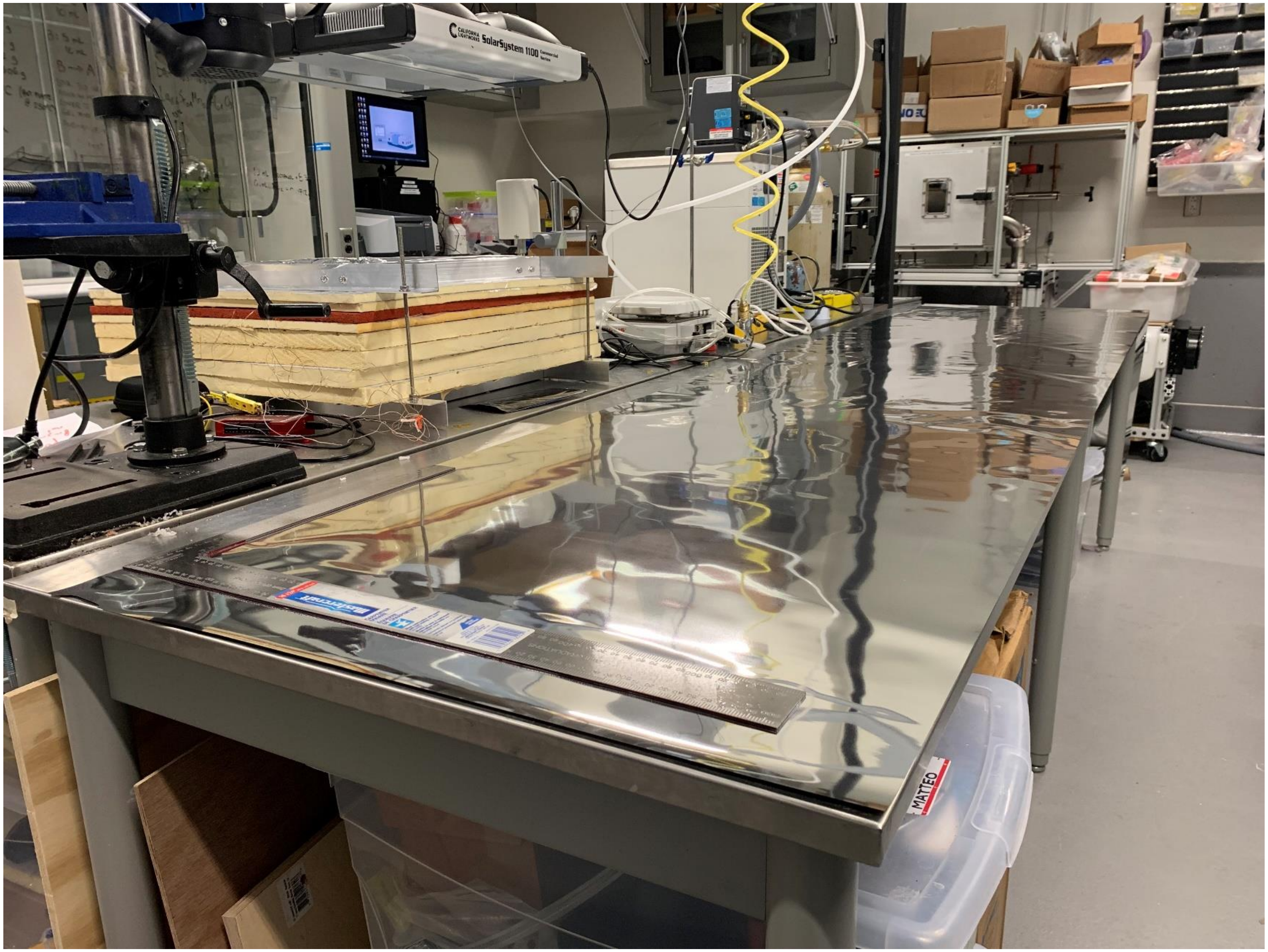

Step 2

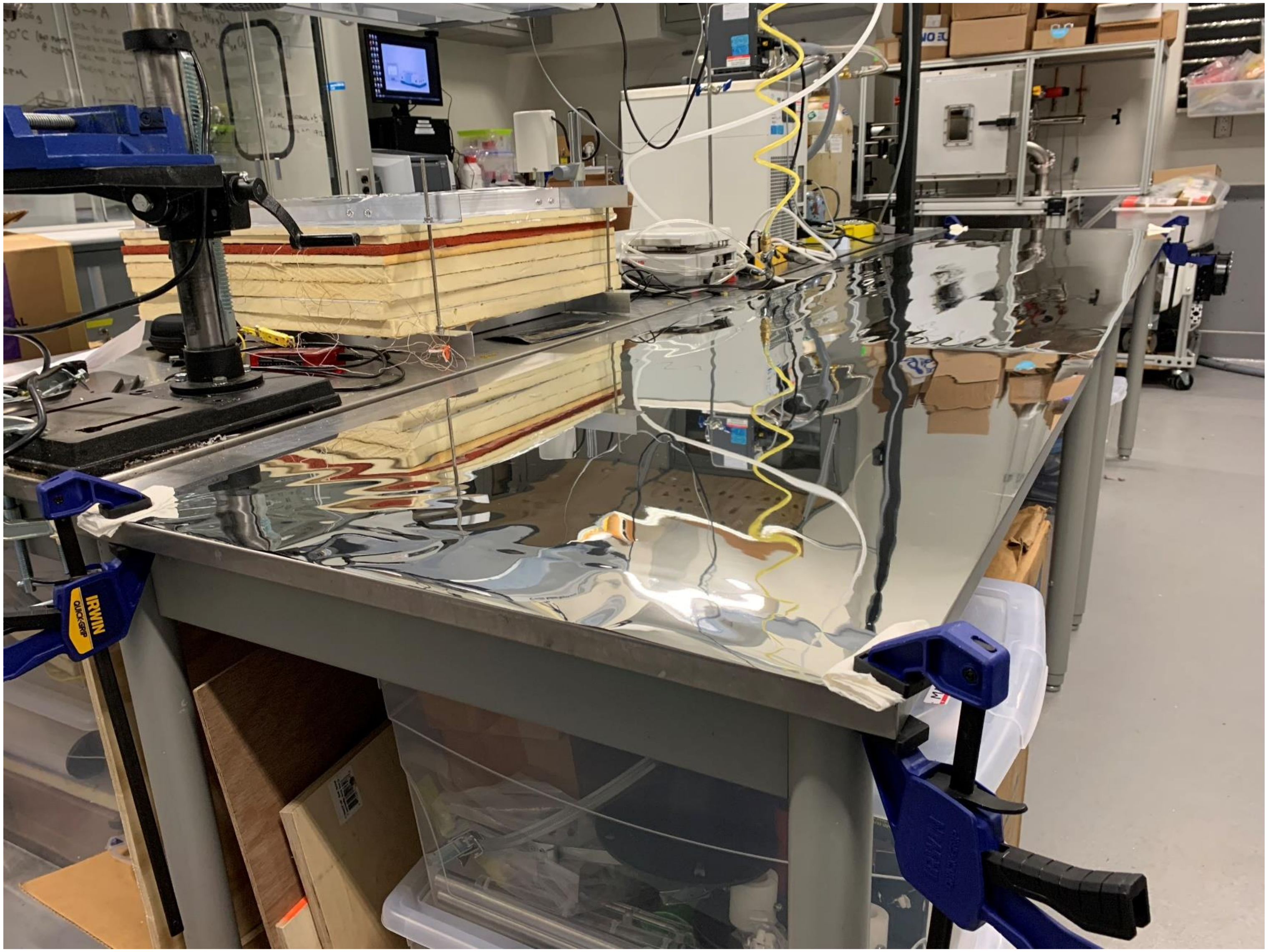

Step 3

Step 4

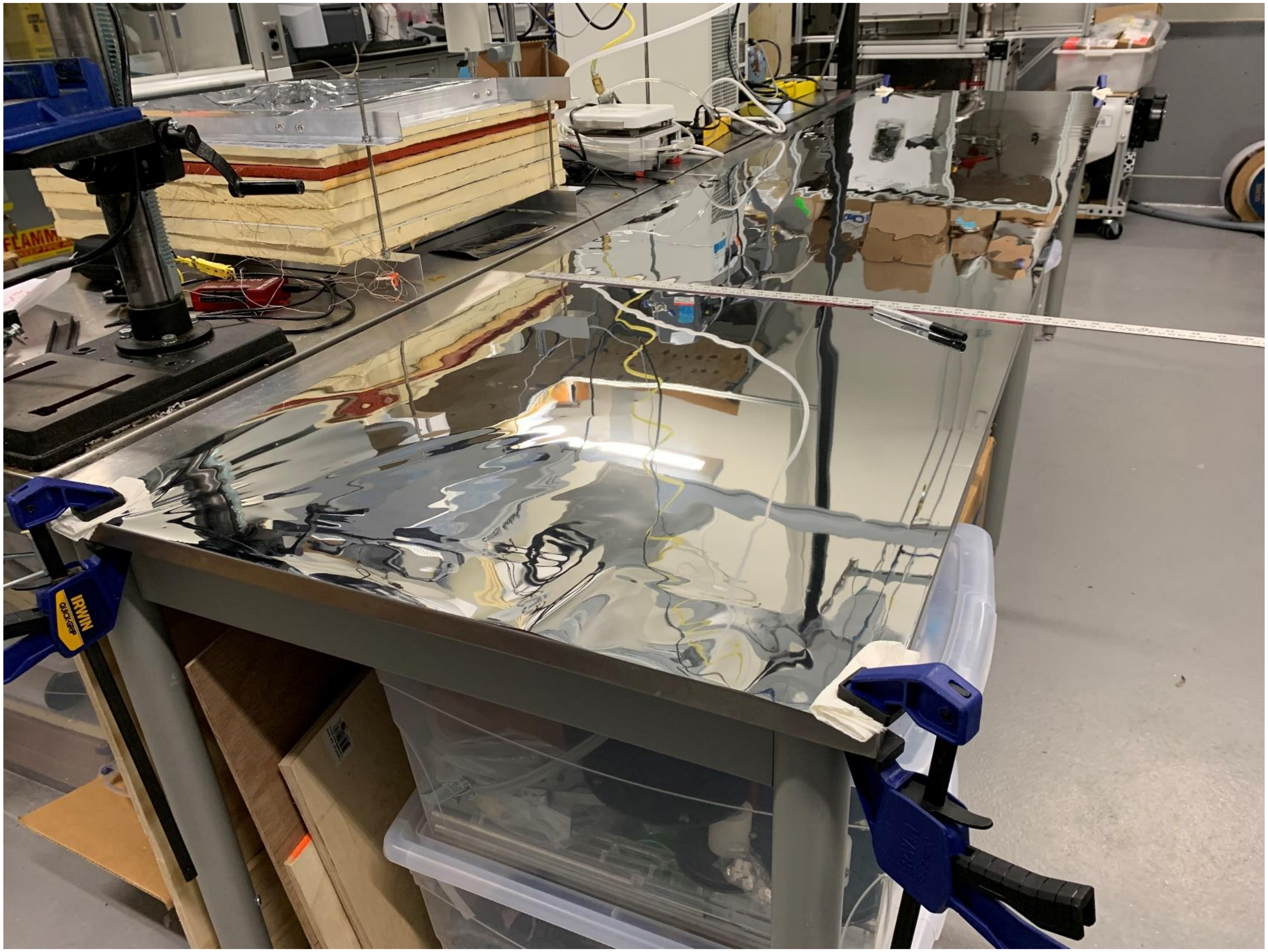

Step 5

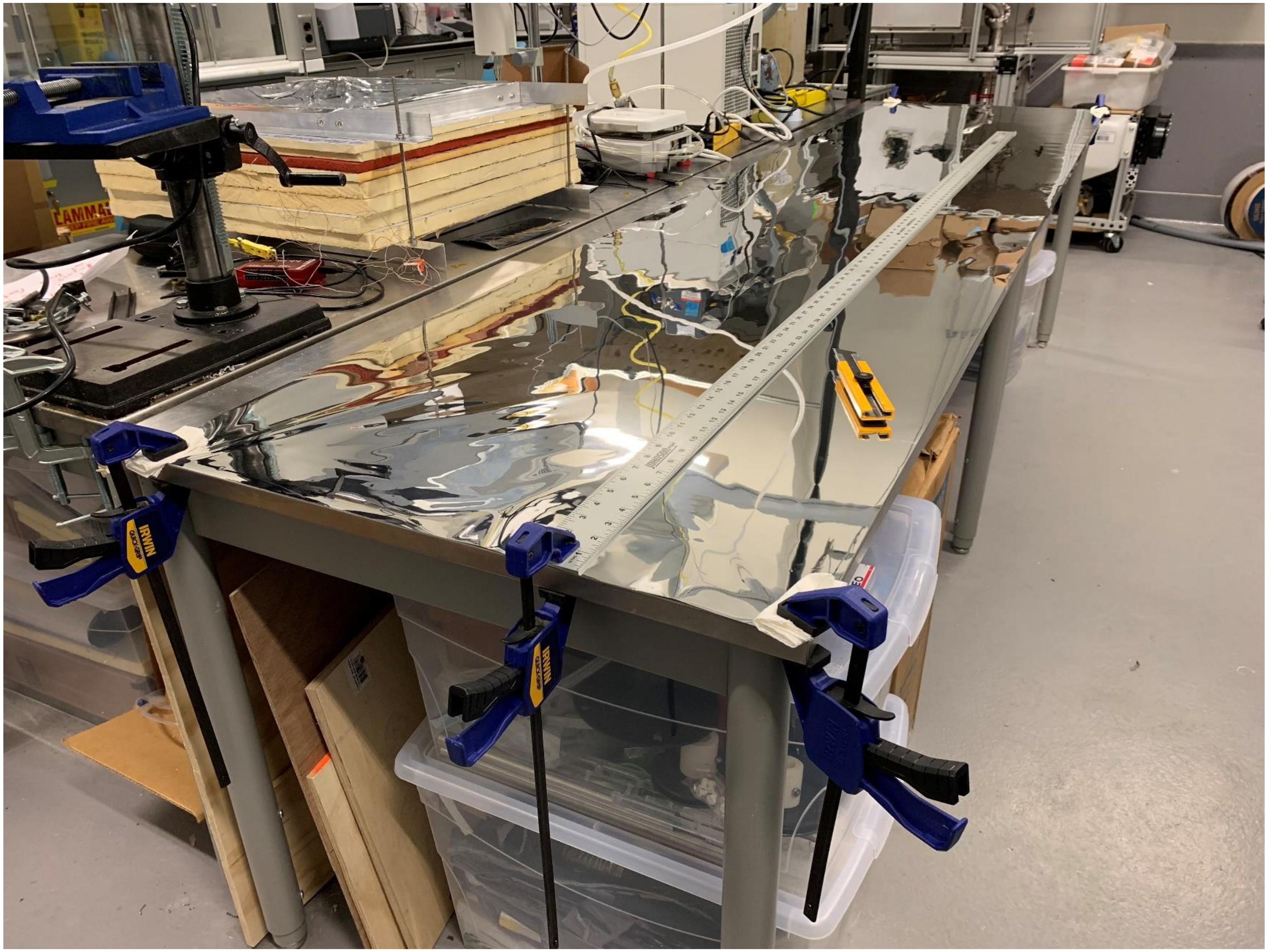

Step 6-7

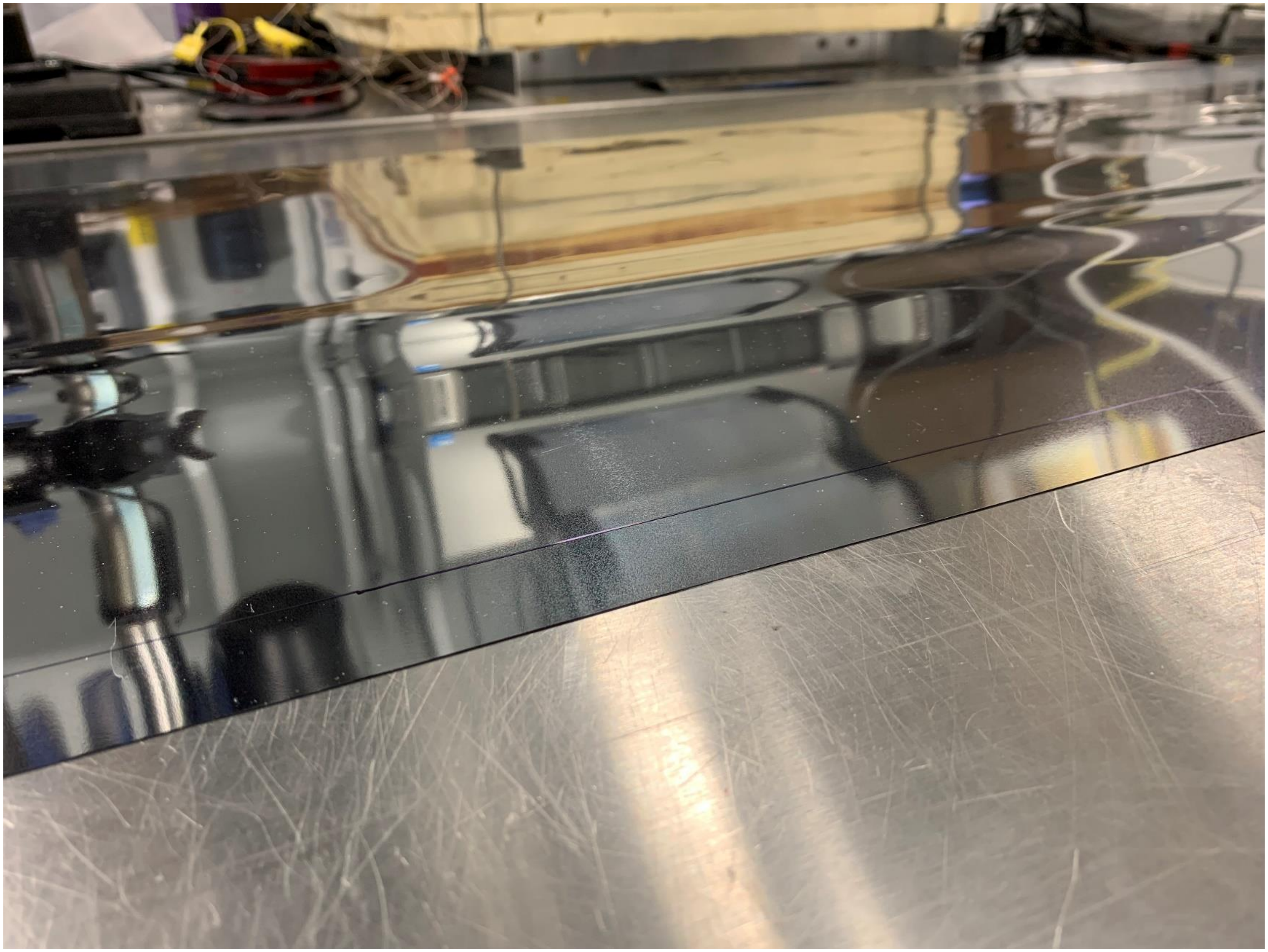

Step 8

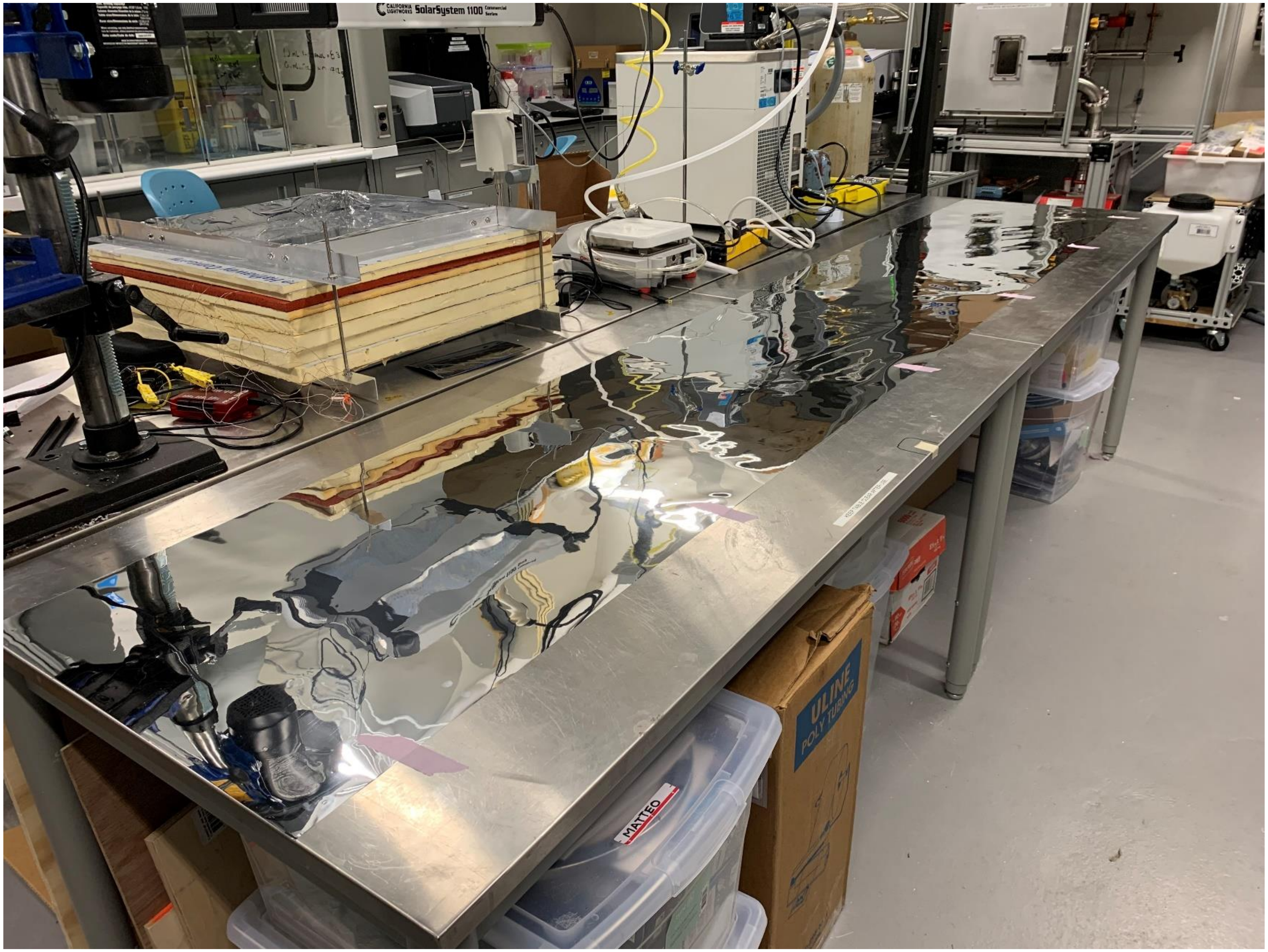

Step 9-10

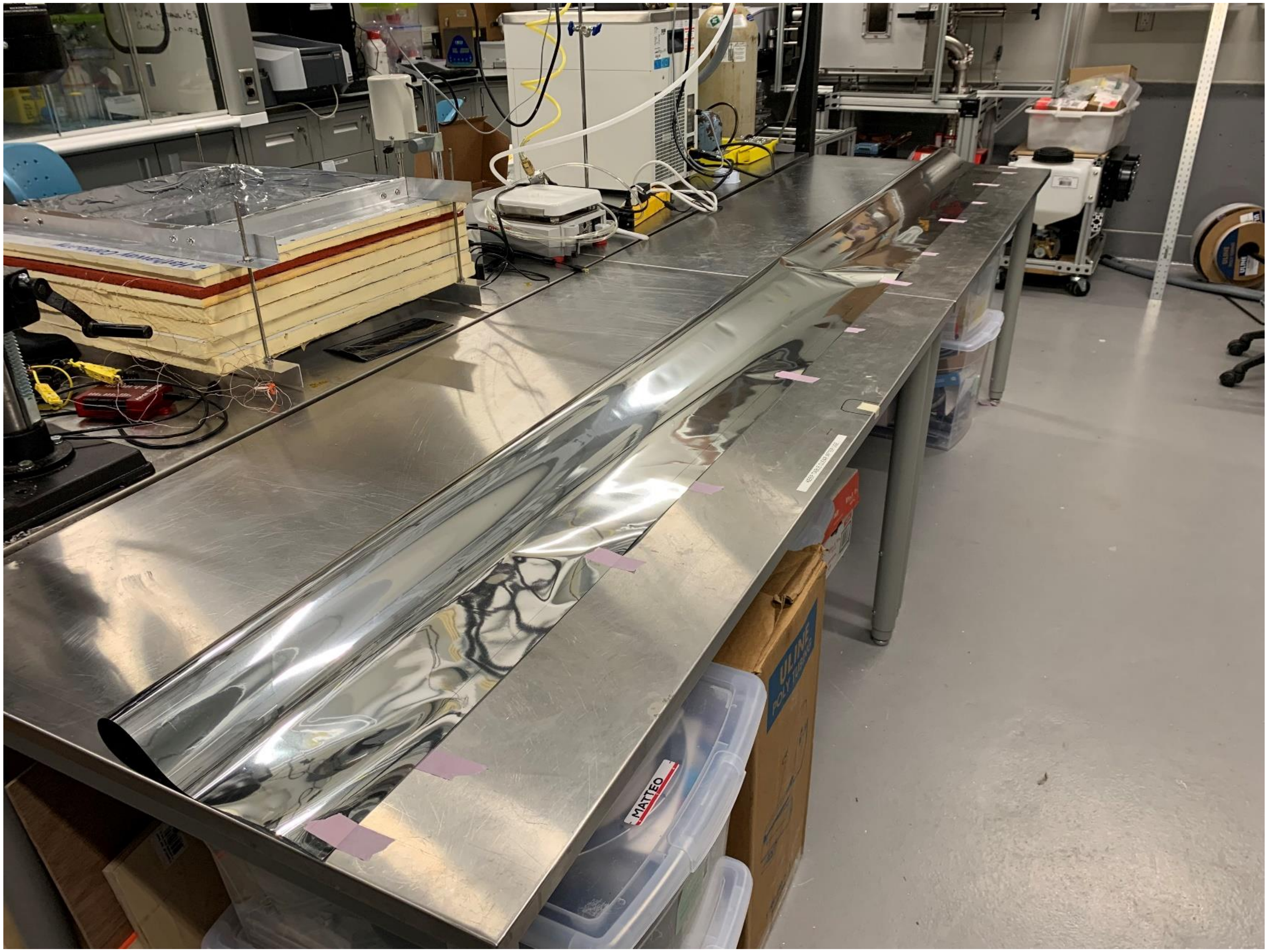

Step 11

Step 13

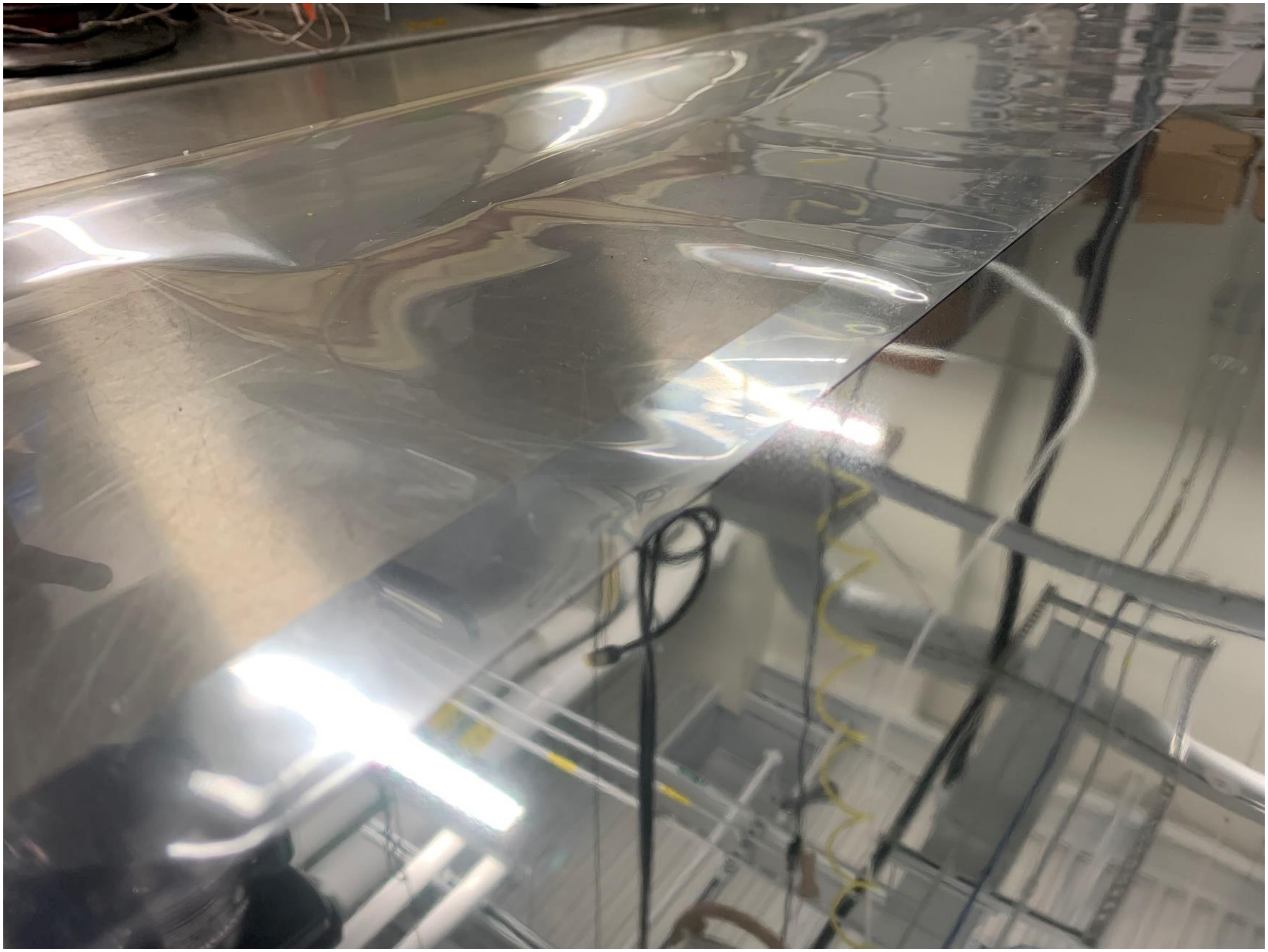

Step 15-16

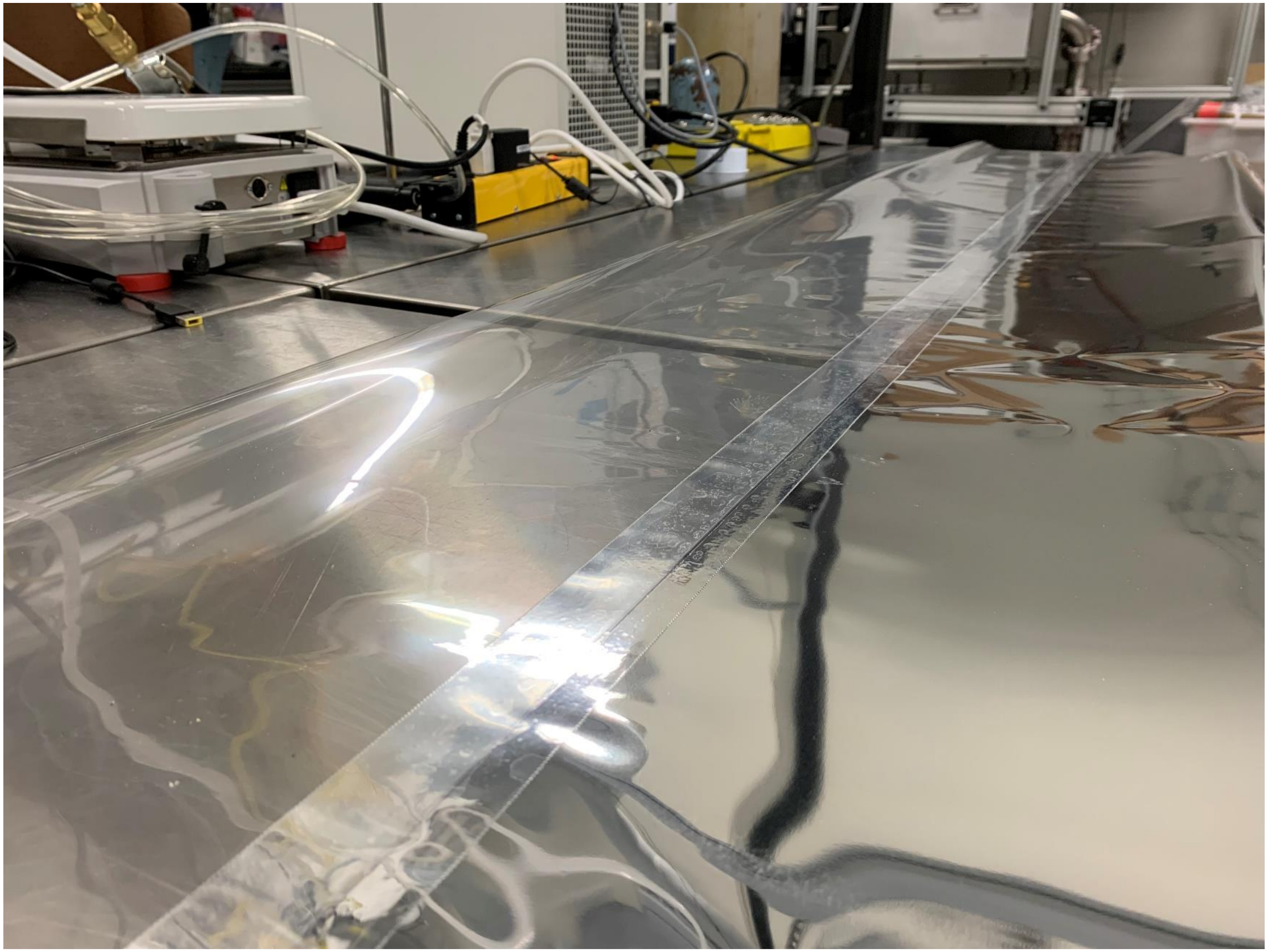

Appendix B

Total absorptance and emittance calculations over a finite wavelength

Typically, the integral for total absorptance and emittance is performed over a wavelength range of 0 to ∞ nm. However, due to the finite measuring spectrum of common devices (UV-vis and FTIR for the present case), this integral must be performed over a subset of the entire wavelength range. It then becomes important to understand what the finite integral implies with respect to the unknown emittance and absorptance values outside of the measured spectrum. That is, performing the integral over a finite wavelength range implicitly assumes a value for spectral emittance and absorptance in the unmeasured region. This section aims to determine the value of the unknown spectral emittance and spectral absorptance.

Consider the equation for calculating the total emittance using the spectral hemispherical emittance

$$\varepsilon = \frac{\int_0^\infty \varepsilon_\lambda E_{b\lambda} d\lambda}{\int_0^\infty E_{b\lambda} d\lambda} \tag{B.1}$$

The integral in the numerator can be split up into three separate ranges

$$\varepsilon = \frac{\int_0^{\lambda_1} x E_{b\lambda} d\lambda + \int_{\lambda_1}^{\lambda_2} \varepsilon_\lambda E_{b\lambda} d\lambda + \int_{\lambda_2}^\infty x E_{b\lambda} d\lambda}{\int_0^\infty E_{b\lambda} d\lambda} \tag{B.2}$$

Since the value of the spectral hemispherical emittance in the wavelength range from 0 to λ_1 and from λ_2 to ∞ is not known, we can replace them with a constant value equal to x. Taking x out of the integral yields

$$\varepsilon = x\frac{\int_0^{\lambda_1} E_{b\lambda}d\lambda}{\int_0^{\infty} E_{b\lambda}d\lambda} + \frac{\int_{\lambda_1}^{\lambda_2} \varepsilon_\lambda E_{b\lambda}d\lambda}{\int_0^{\infty} E_{b\lambda}d\lambda} + x\frac{\int_{\lambda_2}^{\infty} xE_{b\lambda}d\lambda}{\int_0^{\infty} E_{b\lambda}d\lambda} \tag{B.3}$$

We recognize the first and third term as the fractional functions from 0 to λ_1 and λ_2 to ∞

$$\varepsilon = xf_{0-\lambda_1} + \frac{\int_{\lambda_1}^{\lambda_2} \varepsilon_\lambda E_{b\lambda}d\lambda}{\int_0^{\infty} E_{b\lambda}d\lambda} + xf_{\lambda_2-\infty} \tag{B.4}$$

Now consider the total emittance defined over a subset of the entire wavelength range

$$\varepsilon = \frac{\int_{\lambda_1}^{\lambda_2} \varepsilon_\lambda E_{b\lambda}d\lambda}{\int_{\lambda_1}^{\lambda_2} E_{b\lambda}d\lambda} \tag{B.5}$$

We want to know the value of x that will make the total emittance calculated over the entire wavelength range equal to the total emittance calculated over the subset of the wavelength range. Therefore, equating Eq. (B.4) and (B.4)

$$\frac{\int_{\lambda_1}^{\lambda_2} \varepsilon_\lambda E_{b\lambda}d\lambda}{\int_{\lambda_1}^{\lambda_2} E_{b\lambda}d\lambda} = xf_{0-\lambda_1} + \frac{\int_{\lambda_1}^{\lambda_2} \varepsilon_\lambda E_{b\lambda}d\lambda}{\int_0^{\infty} E_{b\lambda}d\lambda} + xf_{\lambda_2-\infty} \tag{B.6}$$

Rearranging for x

$$x\left(f_{0-\lambda_1} + f_{\lambda_2-\infty} \right) = \frac{\int_{\lambda_1}^{\lambda_2} \varepsilon_\lambda E_{b\lambda}d\lambda}{\int_{\lambda_1}^{\lambda_2} E_{b\lambda}d\lambda} - \frac{\int_{\lambda_1}^{\lambda_2} \varepsilon_\lambda E_{b\lambda}d\lambda}{\int_0^{\infty} E_{b\lambda}d\lambda} \tag{B.7}$$

Rewriting the term in the brackets on the left side and factoring out the numerator on the right side

$$x\left(1 - f_{\lambda_1-\lambda_2}\right) = \int_{\lambda_1}^{\lambda_2} E_{b\lambda}d\lambda \left(\frac{1}{\int_{\lambda_1}^{\lambda_2} E_{b\lambda}d\lambda} - \frac{1}{\int_0^{\infty} E_{b\lambda}d\lambda} \right) \tag{B.8}$$

The integral of $E_{b\lambda}$ from 0 to ∞ is simply equal to E_b

$$x\left(1-f_{\lambda_1-\lambda_2}\right)=\int_{\lambda_1}^{\lambda_2}E_{b\lambda}d\lambda\left(\frac{1}{\int_{\lambda_1}^{\lambda_2}E_{b\lambda}d\lambda}-\frac{1}{E_b}\right) \tag{B.9}$$

Factoring out $1/E_b$ on the right side

$$x\left(1-f_{\lambda_1-\lambda_2}\right)=\frac{\int_{\lambda_1}^{\lambda_2}\varepsilon_\lambda E_{b\lambda}d\lambda}{E_b}\left(\frac{E_b}{\int_{\lambda_1}^{\lambda_2}E_{b\lambda}d\lambda}-1\right) \tag{B.10}$$

We recognize the first term in the brackets on the right-hand side as 1 over the fractional function from λ_1 to λ_2

$$x\left(1-f_{\lambda_1-\lambda_2}\right)=\frac{\int_{\lambda_1}^{\lambda_2}\varepsilon_\lambda E_{b\lambda}d\lambda}{E_b}\left(\frac{1}{f_{\lambda_1-\lambda_2}}-1\right) \tag{B.11}$$

Cleaning up the terms on the right-hand side

$$x\left(1-f_{\lambda_1-\lambda_2}\right)=\frac{\int_{\lambda_1}^{\lambda_2}\varepsilon_\lambda E_{b\lambda}d\lambda}{E_b}\left(\frac{1-f_{\lambda_1-\lambda_2}}{f_{\lambda_1-\lambda_2}}\right) \tag{B.12}$$

Dividing out $1-f_{\lambda 1-\lambda 2}$ on both sides

$$x=\frac{\int_{\lambda_1}^{\lambda_2}\varepsilon_\lambda E_{b\lambda}d\lambda}{E_b}\left(\frac{1}{f_{\lambda_1-\lambda_2}}\right) \tag{B.13}$$

Finally, we recognize that $E_b(f_{\lambda 1-\lambda 2})$ is simply the integral of $E_{b\lambda}$ from λ_1 to λ_2

$$x=\frac{\int_{\lambda_1}^{\lambda_2}\varepsilon_\lambda E_{b\lambda}d\lambda}{\int_{\lambda_1}^{\lambda_2}E_{b\lambda}d\lambda} \tag{B.14}$$

The final result shows that performing the calculation for the total emittance over a subset of the entire wavelength range (approximate total emittance) is equivalent to calculating the total emittance over the entire wavelength range assuming that any unmeasured values are equal to the approximate total emittance. The same result can be obtained using absorptance instead of emittance.

Appendix C

Qa-MCRT test cases for validation

Several test cases were simulated using both VeGaS and the Qa-MCRT ray tracing package to determine the validity of the latter. The test cases are described in the following table.

Table C.1. Parameters of the test cases used to validate the Qa-MCRT

Test No.	Rim angle, φ_{rim} [°]	Rec. diameter, D_{rec} [mm]	Rec. placement, C_z [m]	Intercept factor, γ, using Qa-MCRT	Intercept factor,γ, using VeGaS
1	9.0756	2.5550	−0.0792	0.9825	0.9625
2	19.1597	2.7138	−0.0772	0.8396	0.8192
3	29.2437	3.1664	−0.0784	0.5088	0.5257
4	39.3277	4.0761	−0.0809	0.3484	0.3388
5	49.4188	5.6211	−0.0839	0.2808	0.2889
6	59.4958	8.0009	−0.0871	0.2727	0.2749
7	69.5798	11.4449	−0.0899	0.3945	0.3954
8	79.6639	16.2241	−0.0919	0.5797	0.5803
9	89.7479	22.6661	−0.0926	1.000	0.9982
10	99.8319	31.1777	−0.0914	0.9755	0.9726
11	109.9160	42.2766	−0.0877	0.92873	0.9244
12	120.0000	56.6394	−0.0810	0.8759	0.8725